,

ITERATIVE INTERFERENCE CANCELLATION, AND CHANNEL ESTIMATION FOR UNDERWATER ACOUSTIC AND UNSOURCED RANDOM ACCESS COMMUNICATIONS

by

Murwan Bashir

Submitted in partial fulfillment of the requirements
for the degree of Doctor of Philosophy

at

Dalhousie University
Halifax, Nova Scotia
July 2021

to my parents

Table of Contents

List of Tables

List of Figures

Abstract

The work in this thesis is dedicated to design and analysis of iterative interference cancellation systems with applications in underwater acoustic communication and random access communications over terrestrial wireless channels.

In the first part of the work a technique is proposed for signal transmission and reception over underwater acoustic communications channels targeting high spectral efficiency. The transmit data is split into multiple superimposed streams, where each stream is encoded via an error-correction code, interleaved, permuted, and modulated via Orthogonal Frequency Division Multiplexing (OFDM).

Since the channel exhibits a doubly selective nature due to multi-path and fading, a significant channel variation occurs within each OFDM symbol. The task of the receiver is to iteratively refine the channel estimate, cancel the inter-carrier interference (ICI) introduced by the Doppler spread, and inter-data stream interference, and perform error-correction decoding. The receiver is shown that it can operate successfully over a range of significant Doppler spreads. Because of lack of standard underwater channel models, I propose an underwater channel model which is suited for my proposed Kalman Forward-Backward channel estimation algorithm specifically to support the iterative receiver with channel knowledge. Simulation results of the integrated iterative cancellation process with channel estimation are presented.

The second part of the thesis deals with unsourced random access (URA) over Gaussian and fading channels. In a URA setting, a very large number of potential users is considered, while only a smaller subset of the users is active at any given time. The users transmit messages in a grant-free fashion, utilizing a common codebook. A new URA iterative cancellation receiver is proposed and studied, that operates in both Gaussian and fading channels. The transmitted message format is concatenation of preamble and data payload packets respectively. Payload of each user incorporates repetition and permutation, and the task of the receiver is to cancel users' interference when retrieving a user signal. The preamble of each packet carries information about the users signature and permutation sequences. The

main focus is on the approximate message passing (AMP)-based preamble detection algorithms, where user's preambles is employed for channel estimation. As in the underwater case, the URA interference cancellation multi-user detector (MUD) algorithm depends on channel estimate obtained from the preamble part. A set of new preamble detection algorithms which can perform user activity and collision detection, as well as channel estimation for large numbers of active users is presented. The results are compared with the sate-of-the art methods and demonstrate advantages over the existing algorithms for both stand-alone preamble detection and the entire URA system performance.

Acknowledgements

Thanks to everyone.

Chapter 1

Summary

1.1 Introduction

This thesis is dedicated to study, design and analysis of receiver communications architectures which are based on iterative interference cancellation processing with applications in underwater acoustic and wireless and unsourced random access (URA). These environments are distinct in nature and have different parameters settings. We consider acoustic orthogonal frequency division multiplexing (OFDM) modulation-based transmission underwater, where the communication channels exhibit doubly-selective behavior. The power fluctuates across frequency tones as a result of multi-path (frequency selectivity), *and* the signal of a single frequency tone spreads to neighbouring frequency tones and causes inter-carrier interference (ICI). The spread is caused by the channel variation during the OFDM symbol (time selectivity) and results in loss of orthogonality among the OFDM tones. In such setting, the task of the interference cancellation algorithm is to simultaneously estimate transmitted symbols at frequency tones and cancel the interference caused by the *neighbouring* tones. The main challenge comes from the necessity to obtain channel knowledge within each OFDM symbol individually and simultaneously perform interference cancellation and channel estimation.

In a URA scenario at anytime slot, a random subset of devices from a large pool of devices are activated to transmit short data packets, without bandwidth, time, and code resource pre-allocation. Because of the huge size of original user pool, users cannot be assigned pre-allocated identifiers, unlike the case of grant-based access where user's unique identifier is employed to allocate resources on a case of regular random channel access. Additionally, the transmitters are low power devices with low computational capabilities. Because of these constraints, transmitted users' signals actively interfere with each other. At the receiver side, after acquiring channel knowledge, the interference cancellation algorithm is tasked with retrieving user data while cancelling inter-user interference. The challenge is to design the multi-user detection interference cancellation algorithm that supports high number of active users with low error rate per user. This requirement demands high-quality estimation

process, which resembles activity-detection problem, to correctly detect active users and their channels.

Both of the described systems require channel knowledge to perform detection and interference cancellation processes. In order to design estimation algorithms that reliably work in real settings, we utilize emulated channels that closely resemble actual communication channels. For URA setting, the employed channels are standard, such as Gaussian and Rayleigh single path channels, which allows for results comparison. For OFDM underwater channels, however, no universal model exists for communication system evaluation. Hence, we develop a model to serve this purpose.

In this summary we first describe the underwater channel model developed in [1] for single-input multiple-output (SIMO) channel, highlight its main features, and provide a model for multiple-input multiple-output (MIMO) channel, detailed in Chapter 2 and 3 respectively. In Chapter 4, we describe the proposed interference cancellation algorithm for OFDM in doubly-selective underwater acoustic channels and propose to integrate estimation into the interference cancellation. In Chapter 5, we describe the URA setup approach, and the proposed signalling format that enables the capabilities of MUD algorithm, channel estimation approach, and provide a detailed analysis of the system's performance. Each of the following sections provide more details on the problems, the publications, and the contributions made.

1.2 Underwater Channels Models

Channel modeling is an important step in the process of studying and designing a communication system. Typically standardized models, that may be simple or complex, exist and can be readily adopted for system design and testing, as in wireless communications and optical communications, for example. For underwater channels, however, because of a large amount of degrees of freedom in the channel and modeling parameters, there is no unified model for study and design of such systems.

Several SISO channel models have been proposed in the literature. Some of them follow the approach of physical environment modeling such as [2][3], where ray-tracing is employed to determine multi-path propagation profile. Another cohort of models follow a statistical approach as in [4], where time behavior of channel paths is modeled as autoregressive processes. The existing approaches don't offer a test environment that can facilitate design

of singling format, channel estimation, and detection algorithms we consider. More importantly, channel models in MIMO presented as in [1], [5], [6] lag on both physical modeling of MIMO underwater aspects and ignore the key aspect which is the time-space correlation of the channel.

We propose a communication channel model based on the sum-of-sinusoids approach [7], and a notion of correlation footprints together to model correlation for SIMO. We also propose a MIMO correlation modeling approach based on a Lloyd reflection technique and treating surface-time variation. The model developed in Chapter 2 takes into account specific communication-based processes like receive and transmit filtering. The model is base-band and is capable of augmenting Doppler shifts, caused by carrier miss-match between transmitter and receiver, and approximates time-space correlation in case of SIMO setting. The final outcome of the model is a sequence of channel impulse responses for the duration of the OFDM symbol that can be readily used in system testing .

The modeling setup includes setting the environmental parameters such as the nature of sea bottom, depth and the sound-speed profile (sound-speed as function of depth). Additionally, the depth of the transmitter and receiver is supplied to the Bellhop simulator [3] which generates an analog channel characterized by a power-delay profile that shows the time of arrival of each signal propagation path, its power and the number of surface-bottom bounces per path. To add the time variability to the analog paths, the SOS approach is employed. Each analog path is SOS with frequencies sampled randomly to follow decaying exponential Doppler spectrum function. The Doppler spread can potentially be replaced with an observed one. The time-variable paths are then sampled using transmit-receive raised cosine filter to produce channel impulses. By use of the correlation footprint approach, the correlation factor is calculated for any two hydrophones in the receiver array, as a function of overlap area between the footprints which the signals leave on sea surface. Based on the correlation factor, some of the sinusoids are re-employed in path time variability generation to emulate the correlation.

In Chapter 3 we present another model to treat MIMO in underwater channels and explain the nature of time-space correlation function to allow for better physical understanding. The accurate, physically representative spatial-temporal correlation function is crucial for underwater MIMO channel capacity estimation. The current underwater MIMO models assume independence of time and space, and rely on fitted experimental data to justify the

choice of spatial correlation functions. In Chapter 3, derivation of the correlation is initiated by formulating time-space pressure wave between a source and destination using Lloyd mirror model.

The model considers direct and indirect signal propagation paths. The indirect path is modeled as another direct path which is emanating from a mirror source. Hydrophones are assumed to be close to the surface, and far from the bottom such that there is no bottom reflections. By introducing the statistical variables of gravity wave, wave heights and surface velocity through change of frame of reference, the model presents stochastic pressure waves utilized for correlation. The pressure wave, in addition of its dependence of sea environment, depends on the angular spectrum of the source through its frequency response. For a two array receiver, the correlation function approximates to sum of direct path correlation and the indirect. Two sources are tested, the delta function as monochromatic source with a single frequency signal, and the raised-cosine pulse as ploy-chromatic source with a bandwidth of frequencies. For a vertical and horizontal array setting, the correlation between arriving pressure waves is high because of the dominance of the direct path. The indirect path correlation vanishes dramatically with angular separation between the receiver elements, and becomes much smaller compared to direct path. The work on modelling been summarized in the table below.

Publication	Status and Contributions
Truhachev, D., Schlegel, C., Bashir, M. and Bousquet, J.F., "Modeling of underwater acoustic channels for communication system testing," *In OCEANS 2018 MTS/IEEE*, Charleston, USA, pp. 1-8, 2018, October.	Published, contributed to the model design, and designed model evaluation parameters.
Bashir, M., Ponomarenko, S.,Truhachev, D. Acoustic Pressure Correlations in Deep Ocean with Applications to Multiple-Input Multiple-Output Underwater Communications. *to be re-submitted to Journal of Acoustical Society of America.*	Addressing reviewers comments to be resubmitted, contributed to model design and performance testing.

1.3 Iterative Interference Cancellation For Acoustic Underwater OFDM System

Bandwidth available for underwater communication systems is a critical resource and its optimal utilization is necessary to achieve high spectral efficiency required for short to medium

transmission ranges and high throuput applications such as video transmission. The early attempt of video transmission, presented in of [8], used differential phase shift keying (DPSK) and a slow rate of transmission is observed. The orthogonal frequency division modulation (OFDM) is advocated for underwater acoustics communication in many research contributions [9][10][11], and we adopt it here under SISO and SIMO setting. OFDM allows for treating the channel conveniently in frequency domain at both transmitter and receiver. Higher order constellations are also desirable to enhance spectral efficiency.

Given the doubly spread nature of the underwater channel, the approach of higher order constellation OFDM system quickly becomes challenging because of the long delays that causes severe inter-symbol interference (ISI), in addition to the ICI. The approach we present here uses a transmission format where multiple streams with unequal powers that are independently modulated and superimposed to achieve higher constellation that is tolerant to ISI and achieve targeted high spectral efficiency. The theory of multi-users detection offers various techniques for interference cancellation, and allow for channel estimation integration to the process. Moreover, MUD theory is rich with analysis tools to borrow for system parameter optimization. The key question which I worked on and provided a solution is "how to estimate accurately the doubly selective channel within each OFDM symbol".

In chapter 4 the employed OFDM signalling is utilized in an multi-user-like interference cancellation system. In electromagnetic (EM) wireless channels, the multi-path channel is static during the OFDM symbol duration, and results in un-equal power frequency tones or so called frequency selectivity, and no frequency tone is interacting with its neighbouring ones. As mentioned earlier, in underwater OFDM the channel is dynamic during the OFDM symbol, and each frequency tone signal spreads into neighbouring frequency tones, and the higher the channel's Doppler spread the wider is the neighbourhood of the interference. The frequency domain channel matrix captures both effects, with frequency selectivity present as diagonal elements of the channel matrix in frequncy domain of un-equal power, and time selectivity as decaying off-diagonal elements with decay depends on Doppler spread.

When a receiver processes a single stream of data, with perfect channel knowledge, one iteration operation is comprised of symbols detection, interference estimation and subtraction. Symbols detection utilizes diagonal elements of frequency domain channel matrix, and the resulting symbols estimates are used with the off-diagonal elements to estimate the interference and cancel it. The next iteration starts with less interference and the process

continues until it reaches the interference free state. Using SISO channel model presented in Chapter 2, the system is evaluated, with perfect channel knowledge, for wide range of Doppler spreads, and system settings (bandwidth and number of OFDM frequency tones) and to demonstrate convergence to interference-free state.

In the sequel, the channel estimation process replaces the perfect channel knowledge assumption, and the operation of the iterative receiver follows the sequence of channel estimation, symbols detection and interference cancellation. The cancellation process requires high accuracy channel estimate and tracking for the duration of the OFDM symbol, especially for small bandwidths of underwater channel and high number of tones to increase transmission rates. Well known adaptive filters provide decent estimates only for lower Doppler spreads, disregard channel models to improve estimation quality, and omit certain structures of received signal that are useful for estimation. My proposed first-order Kalman forward-backward filter (KFBF) is able to provide channel estimates that allow the cancellation to start successfully and converges. The soft-data aided KFBF that utilizes soft-data as pilots is presented and studied as pre-cursor to uniting channel estimation, interference cancellation and data detection processes. The integrated systems are tested for range of Doppler spreads, and proved successful convergence.

My contributions include proposing FBKF and its soft-data aided version which enables usage of data detected in channel estimation process. The algorithm's Mean Square Error (MSE) performance is studied using first and second order autoregressive processes as channel models for a wide range of Doppler spreads. I then integrated the channel estimation with interference cancellation system, and studied the effect of the estimate quality on the convergence process using experimental state evolution. The resultant Bit Error Rates (BER) are compared with the case of perfect channel knowledge case. Additionally, the channel estimation algorithm is utilized to quantify the effect of beam forming in terms for MSE reduction. The following table lists relevant publications.

Publication	Status
Bashir, M., Truhachev, D. and Schlegel, C., 2018, May. Kalman forward-backward channel tracking and combining for OFDM in underwater acoustic channels. In 2018 OCEANS-MTS/IEEE Kobe Techno-Oceans (OTO) (pp. 1-10). IEEE.	Published
Eskandari, N., Bashir, M., Truhachev, D., Schlegel, C. and Bousquet, J.F., 2018, May. Improving the Quality of Underwater Acoustic Channel via Beamforming. In 2018 OCEANS-MTS/IEEE Kobe Techno-Oceans (OTO) (pp. 1-7). IEEE.	Published
Bashir, M., Truhachev, D., Schlegel, C. Iterative Equalization and Estimation, Superposition Modulation.	To be submitted

1.4 Iterative Interference Cancellation For Unsourced Random Access (URA)

We consider a class of random-access systems, proposed in [12], where the potential pool of users is very large with a much smaller random and varying set of active users that infrequently transmit short messages to the receiver point. As mentioned earlier, because of the short message constraint and the large size of users' pool, the utilization of unique users identifiers is hindered, and the receiver is tasked with retrieving users' data without explicit knowledge of users IDs. Consequently, the users access the channel without resource allocation requests. Such setting presents itself in applications like sensor networks, internet of things, and generally in scenarios where sensor data is more important than IDs.

The URA concept is approached using various methods based on compressed sensing (CS) [13, 14, 15, 16, 17], irregular slotted and T-fold ALOHA [18, 19, 20, 21], and preamble-data payload format [22, 23, 24, 19]. The systems derived in the mentioned approaches are compared in performance, in terms of the number of supported active users, and far from random coding bound in [12] especially for high numbers of active users. It is important to note that per user probability of block error is the measure of success instead of the "every users success" requirement of the classic multiple access.

We utilize preamble/payload format, where the preamble carries a part of the user's message, encoded using a Gaussian signature dictionary, and communicates signature/permutation pair which will be used in the payload. The payload part employs error-correction code, and uses signature/permutation pair to scramble and spread data. At the receiver side, approximate message passing (AMP) algorithms, for Gaussian and Rayligh access channels, are employed to recover the signature/permutation pair from the preamble and initiate the

multi-user detection algorithm for the payloads. MUD algorithm refines channel estimates and performs SNR-based selective decoding with removal of successfully detected users packets.

Since the access is grant free, two or more users can collide in case they randomly select the same signature sequence. For the case of equal power Gaussian channel, the preamble channel estimator results in an activity detection algorithm. The preamble activity detection problem setting resembles a compressed sensing linear system and approximate message passing (AMP) is typically utilized to solve for the sparse activity detection vector. The CS-AMP algorithm is collision ignorant, and starts to miss-detect users and introduces false ones as number of active users increase (and probability of collision increases accordingly). Both false alarms and missed detections deteriorate the performance of the MUD algorithm. Therefore, I present pair-collision aware algorithms to mitigate this problem. For the case of URA operating in Rayleigh channel, the channel is sparse complex Gaussian vector, and the joint activity detection and channel value estimation is required. By extending the activity-detection only to exploit the Rayleigh distribution, the joint estimation task is proved possible, and can support the missed detection/false alarms rates required for MUD performance, to achieve much higher number of active users than existing algorithms.

My contribution is the development and study of the collision-aware AMP algorithm, as well joint channel estimation and activity detection AMP and integration with MUD algorithms. The following table list relevant publications.

Publication	Status
Truhachev, D., Bashir, M., Karami, A. and Nassaji, E., "Low-Complexity Coding and Spreading for Unsourced Random Access," *IEEE Communications Letters*, March 2021.	Published
Nassaji, E, Bashir, M.,Truhachev, D., "Unsourced Random Access over Fading Channels via Data Repetition, Permutation, and Scrambling," *submitted to IEEE Transactions of Communications.*, 2021	Submitted

Chapter 2

Underwater Channel Model

2.1 Abstract

A model for single-input multiple output (SIMO) underwater acoustic channel is proposed. The model targets testing of underwater acoustic communication systems and incorporates multi-path, Doppler spread and shift, as well as correlation between the signals at multiple receive hydrophones, transmit/received filtering and sampling. A study of receive hydrophone correlation based on surface correlation footprints is included. An example of a modeled and measured channel corresponding to the same communication scenario is presented together with the bit-error rate (BER) results for a data receiver algorithm which includes channel estimation and iterative equalization performed on the measured and modeled channels for comparison.

2.2 Introduction

Propagation of sound in underwater ocean environments is a complex physical phenomenon. A multitude of approaches to underwater acoustic propagation modeling have been proposed over the years. The focus and the areas of application of models vary: oceanography, sonar systems, underwater navigation, positioning and sensing, environmental observation etc. We target modeling of the underwater acoustic channel for the sole purpose of communications system design and testing. The underwater acoustic communication channel is a doubly-spread channel that exhibits frequency selectivity (multi-path effect) and time selectivity (fading). Because of the necessity to utilize multiple receivers and, in some cases, transmitters, spatial behavior of the channel is of significant importance for channel modeling.

One of the key aspects in establishing high-rate coherent acoustic communications underwater is accurate channel estimation and tracking. Realistic testing of channel estimation algorithms involves modeling channel multi-path profiles, Doppler effects (shift and spread),

and their impact on the transmitted data in time and frequency. The effect of the transmit and receive filtering also needs to be included. Testing of Doppler-shift compensation, synchronization, and channel equalization algorithms all require accurate modeling of these effects.

Understanding the potential of multiple-input multiple-output (MIMO) communications underwater requires modeling of the spatial correlation between the channel impulse responses in time and frequency. The channel correlation and its temporal behavior impact the channel rank, resulting capacity and MIMO communication algorithms such as beamforming [25] and equalization. Modeling of signals arriving from different directions with their associated time delays and frequency shifts is required together with an understanding of the physical effects behind spatial correlation of the propagating signals.

While no standardized underwater communications channel model exists, a number of approaches have been developed. Among these are channel ray-tracing [26] and parabolic equation propagation models [27], as well as statistical models [28]. The model proposed in [28] is a point-to-point model that models the channel dynamics based on modeling a physical processes underlying underwater sound propagation such as extension and contraction of the sound propagation paths and formation of micro-path clusters causing Doppler spread.

In an attempt to model MIMO channels two major approaches are usually taken: the first is to extend a point-to-point channel model including the transmit and receive array geometry without explicitly modeling the correlation effect (see for example [29]) or looking at general matrix-based MIMO channel models with transmitter and receiver correlation applied externally [30].

Instead of modeling the physical reality of ocean propagation environments and communications channels resulting from transmitter/receiver deployments within these, our focus is on creation of artificial test channels that would provide communications algorithms with the same set of challenges as the real acoustic underwater channel would. Our approach is to propose a structurally simple model core that depends on a few experimentally observed or precomputed parameters. When assessing the modeling performance we would like to ensure that our test algorithms (channel tracking [31], equalization [32] etc.) demonstrate similar performance on both the model and a corresponding channel measured in sea trials.

The proposed model starts with a power-delay profile (as the model in [28]) which is either

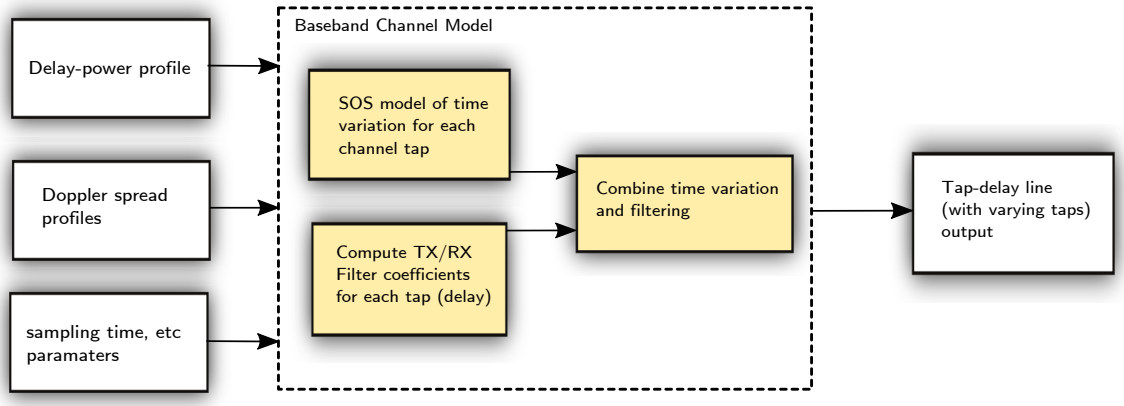

Figure 2.1: Channel model setup.

measured in a sea trial, produced by a ray-tracing simulator, or created artificially for testing purposes. The time evolution of each channel tap is determined by a selected scattering function, such as a exponentially decaying Doppler spread function [33], and generated using a sum-of-sinusoids (SOS) technique [34]. Transmit and receive filtering and sampling is then applied to create a time-varying tap-delay model of the channel in baseband. In a related work, statistical underwater acoustic channel modeling based on artificial generation of channel tap variation has been considered in [35] where random Gaussian process is used to generate each path dynamics and is shaped to have specific Doppler spectra obtained during sea measurements. In [36] a stochastic replay approach is taken where a measured channel is considered to be a single instance of a random process characterized by a number of parameters and other realizations of that random process are generated for the purpose of channel modeling. Here we take an approach to use SOS that gives us possibility of controlling the fading dynamics and initiation of correlated fading processes for different receive hydrophones. Also the above-mentioned models consider point-to-point channel while we take a step to model the spatial behavior of the channel as well.

The proposed single-input multiple-output (SIMO) model uses the angle of arrival information of the propagation paths as well as the array geometry to generate the tap-delay profile and fading processes at each receive hydrophone. The correlated fading processes at various hydrophones are generated by reusing groups of frequencies and phases seeding the SOS model generating time-fading of the channel taps. In order to realistically set the correlation parameters we utilize the ray-tracing propagation geometry and use Huygens'

principle to derive the approximate surface areas contributing to the Doppler spectra of the respective channel taps observed at neighboring hydrophones. The overlap of these "correlation footprints" is used to set the approximate tap correlations.

2.3 Model Setup

The flow of the modeling process is presented in Fig. 2.1. The input parameters include channel power-delay profile given by L_p paths with delays $\tau_1, \tau_2, \cdots, \tau_{L_\mathrm{p}}$ and average powers $P_1, P_2, \cdots, P_{L_\mathrm{p}}$. For each channel path we consider a Doppler spread function $S_l(\nu)$, which, in the simplest case, can be defined by a single parameter α_l representing root-mean square (RMS) Doppler spread for path $l = 1, 2, \cdots, L_\mathrm{p}$. The Doppler spread function determines time-selectivity (fading) of the channel and we follow a common assumption that fading processes are independent for all L_p paths. The carrier frequency is given by f_c.

The L_p paths result from the acoustic wave propagation from the transmitter to receiver without the effect of transmit/receive filtering and sampling and represent an "infinite bandwidth" channel model. To create a tap-delay baseband channel model suitable for testing acoustic communication systems we introduce the transmit/receive filter impulse response $g(t)$ and sampling time T_s.

To model SIMO systems we consider a vertical line array (VLA) at the receiver with distance d meters between each pair of neighboring hydrophones. We also consider the angle of arrival θ_l, $l = 1, 2, \cdots, L_\mathrm{p}$ for each channel path. The incident angle for each path is the same for all hydrophones. We assume that a path is a result of a flat acoustic wavefront arriving at the VLA. This implies that the fading processes generated by one wavefront on different hydrophones are correlated. We define correlation parameters $\rho_l \in [0, 1]$, $l = 1, 2, \cdots, L_\mathrm{p}$ which determine the correlation between two fading processes on the neighboring hydrophones in the receive VLA for each channel path.

2.3.1 SIMO Modeling Setup

The first hydrophone of the receive VLA is considered as the reference hydrophone. The acoustic wavefront from channel path l, $l = 1, 2, \cdots, L_\mathrm{p}$ arriving from an incident angle θ_l reaches hydrophone i, $i = 1, 2, \cdots, N$ with delay $\Delta_l^{(i)} = d(i-1)\sin(\theta_l)/c$ measured with respect to the reference hydrophone.

An infinite-bandwidth L_{p}-path channel in baseband observed at hydrophone i, $i = 1, 2, \cdots, N$ can be written [37] as

$$h^{(i)}(t;\tau) = \sum_{l=1}^{L_{\mathrm{p}}} \sqrt{P_l} h_l^{(i)}(t) \delta(\tau - \tau_l^{(i)}(t)) e^{j2\pi f_{\mathrm{c}} \Delta_l^{(i)}} \tag{2.1}$$

where $h_l^{(i)}(t)$ is the fading process for channel path l at hydrophone i, the delay equals

$$\tau_l^{(i)}(t) = \tau_l + \Delta_l^{(i)} \ ,$$

and the exponential factor $e^{j2\pi f_{\mathrm{c}} \Delta_l^{(i)}}$ results from the down-conversion to baseband.

2.3.2 Sum-of-Sinusoids Model

The fading process $h_l^{(i)}(t)$ is generated using a sum-of-sinusoids (SOS) technique [34]

$$h_l^{(i)}(t) = \frac{1}{\sqrt{M}} \sum_{m=1}^{M} e^{j(\phi_{l,m}^{(i)} + 2\pi f_{l,m}^{(i)} t)} \tag{2.2}$$

as a sum of M unit-power complex exponentials with frequencies $f_{l,m}^{(i)}$, $m = 1, 2, \cdots, M$. The initial phases $\phi_{l,m}^{(i)}$, $m = 1, 2, \cdots, M$ are selected independently from the uniform distribution on the interval $[0, 2\pi]$. The M frequencies $f_{l,m}^{(i)}$ are selected to generate time variation of path l according to scattering function $S_l(\nu)$. It is common to utilize an exponentially decaying Doppler spread function [33]

$$S_l(\nu) = \frac{1}{2\alpha} e^{-|\nu|/\alpha} \ . \tag{2.3}$$

where α_l is root-mean square (RMS) Doppler spread (Hz). In order to guarantee

$$S_l(\nu) = \left| \lim_{M \to \infty} \mathcal{F} \left(\mathbb{E}_t h_l^{(i)}(t) h_l^{(i)}(t + \Delta t)^* \right) \right| \tag{2.4}$$

(where $\mathcal{F}$ denotes Fourier transform) we select frequencies $f_{l,m}^{(i)}$ independently out of a distribution determined by the probability density function (pdf) $S_l(\nu)$. The respective cumulative distribution function (cdf) is given by

$$F(f) = \int_{-\infty}^{f} \frac{1}{2\alpha} e^{-|\nu|/\alpha} \mathrm{d}\nu = \frac{\mathrm{sgn}(f)}{2} \left(1 - e^{-|f|/\alpha}\right) \ . \tag{2.5}$$

Inverse transform sampling allows us to use uniformly distributed $u \in [0, 1]$ and set $F(f_{l,m}^{(i)}) = u$ in order to generate

$$f_{l,m} = -\alpha \log \left(\mathrm{mod} \ (2u, 1) \right) \mathrm{sgn}(1 - 2u) \tag{2.6}$$

such that pdf of $f_{l,m}^{(i)}$ equals $S_l(\nu)$.

2.3.3 Setting up hydrophone correlation

It is common to observe correlation between signals received by the VLA. While in practice correlation is time dependent we include an average correlation parameter ρ_l, $l = 1, 2, \cdots, L_{\mathrm{p}}$ into the model. A more-detailed study of the correlation is given in Section 4.8.

In order to guarantee the average correlation between fading processes for two neighboring hydrophones

$$\mathbb{E}_t h_l^{(i)}(t) h_l^{(i+1)}(t)^* = \rho_l \tag{2.7}$$

we select the sinusoid frequencies $f_{l,m}^{(i)}$ such that ρM frequencies are shared between the frequency set $f_{l,m}^{(i)}$, $m = 1, 2, \cdots, M$ for hydrophone i and the frequency set $f_{l,m}^{(i+1)}$, $m = 1, 2, \cdots, M$ for hydrophone $i + 1$.

During the frequency-generation process we can start from the reference hydrophone and select M frequencies for each path. Then for the second hydrophone we draw ρM frequencies uniformly from the previously selected set and add $(1 - \rho)M$ new frequencies. For the third hydrophone we draw ρM frequencies uniformly from the second hydrophone set and add $(1 - \rho)M$ new frequencies and so on. Note that this process restricts the range of possible correlation patters between hydrophones. Another approach would be to generate random set of frequencies for each hydrophone and then multiply with the correlation factor to obtain the required correlation.

In order to select phases $\phi_{l,m}^{(i)}$ we follow the same sharing process as with the frequencies but we also take into account the phase differences $2\pi f_{\mathrm{c}} \Delta_l^{(i)}$ caused by the acoustic wave propagation between the hydrophones in the VLA and add respective terms for the phases of hydrophone i, $i = 1, 2, \cdots, N$. Here we assume that the speed of the sound in the water c is constant within the VLA.

2.3.4 Filtering and Sampling

Consider transmit filter $q(t)$ and the same receive filter with combined transit/receive filter given by the convolution $g(\tau) = q(\tau) \star q^*(-\tau)$. The channel for hydrophone i including transmit/receive filtering is then represented by the convolution

$$f^{(i)}(t; \tau) = h^{(i)}(t; \tau) \star g(\tau). \tag{2.8}$$

Finally we consider sampling with sampling time T_{s}. The sampled received signal values

$y_k^{(i)} = y^{(i)}(kT_\mathrm{s})$, $k = 0, 1, 2 \cdots$ at hydrophone i are given by

$$y_k^{(i)} = \sum_{l=1}^{L} x_{k-l} f_{k,l}^{(i)} + n_k \tag{2.9}$$

where $n_k = n(kT_\mathrm{s})$, $k = 0, 1, 2 \cdots$ is the sampled noise, $x_{k-l} = x((k-l)T_\mathrm{s})$ is the sampled transmit signal, and $f_{k,l}^{(i)}$ is the sampled channel (tap-delay line) where k is the time sample index and l is the delay sample index, L is the number of discrete (sampled) channel taps. Note that we assume perfect synchronization between transmitter and receiver. However, this assumption might not hold in real setting because of transmitter and receiver movements resulting in time dilation.

The discrete filtered channel taps for the multi-path case are then generated as

$$f_{k,l}^{(i)} = \sum_{l'=1}^{L_\mathrm{p}} \sqrt{P_{l'}} h_{l'}^{(i)}(kT_\mathrm{s}) g(lT_\mathrm{s} - \tau_{l'}^{(i)}(kT)) e^{j2\pi f_\mathrm{c} \Delta_{l'}^{(i)}} \tag{2.10}$$

for $l = 1, 2, \cdots, L$, $i = 1, 2, \cdots, N$.

In a practical model implementation it is convenient to first generate the fading processes $h_{l'}^{(i)}(kT_\mathrm{s})$ and then obtain the convolution with the transmit/receive filter $g(lT_\mathrm{s} - \tau_{l'}^{(i)}(kT))$ as in (2.10).

2.3.5 Doppler Shift

If the receiver moves at constant speed v relative to the transmitter, channel path l will experience a Doppler shift dictated by the Mach number $a_l = v/c \cos(\theta_l)$ (not including the effect of bandwidth)

Then the channel model takes the form

$$h^{(i)}(t;\tau) = \sum_{l=1}^{L_\mathrm{p}} \sqrt{P_l} h_l^{(i)}(t(1+a_l)) \delta(\tau - \tau_l^{(i)}(t)) e^{j2\pi f_\mathrm{c} \Delta_l^{(i)}(1+a_l)} \tag{2.11}$$

where

$$\tau_l^{(i)}(t) = (\tau_l + \Delta_l^{(i)})(1 + a_l)$$

The rest of the modeling process is the same including the SOS channel tap model, tap correlation between the hydrophones, filtering and sampling. The next section deals with hydrophone correlation in more detail.

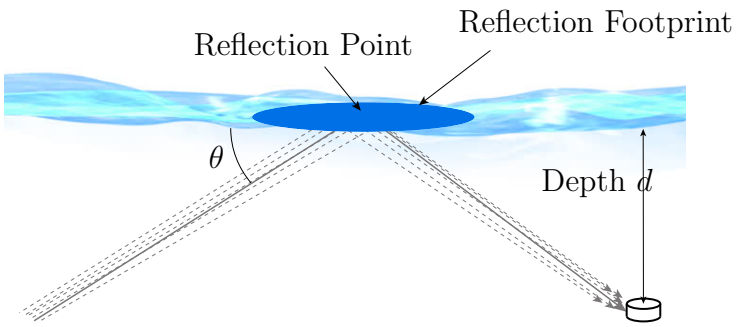

Figure 2.2: Illustration of signal reflection at the sea surface.

2.4 Correlation Between Receive Hydrophones: The Correlation Footprint Approach

The way reflections of acoustic energy at the sea surface is typically viewed is that akin to a mirror, as illustrated in Fig. 2.2 by the solid line. However, as argued in recent treatises on the subject [28], that single path is in reality a bundle of many close path that are generated by the typically rough sea surface. This is illustrated in the figure by the dashed paths.

The reflection footprint, highlighted in the figure, is the area of sea surface that "significantly" contributes to the signal a the receive hydrophone. While a truly planar incident wave would generate received signal power from the infinitely large sea surface, and there would be no clearly defined reflection footprint, we will show that we can nonetheless sharply define such a footprint. To do this, we first make the following observations: (i) clearly, the incident wave is not an infinite-size planar wave and can be considered planar only over a relatively small area, certainly an area whose diameter is smaller then d; (ii) in order to estimate statistical correlation, we are not so much interested in how much energy the footprint reflects, but how large is the footprint such that the energy from it arrives at the hydrophone mostly coherently. Outside this coherence area, there won't be a statistical correlation either. We'll see that our analysis will give a sharp definition for the criteria (i) and (ii). Lastly, (iii), the footprint can be no larger than the average length of the surface waves which create the time variations in the path bundles in the first place. Beyond that wave length, statistical signal correlation is also not expected to be significant.

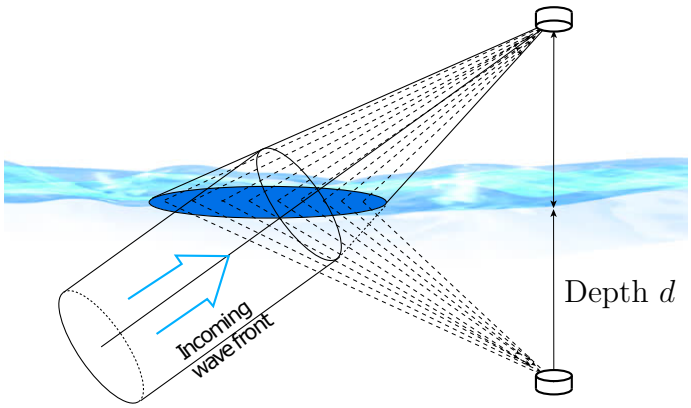

Figure 2.3: Illustration of signal reflection at the sea surface.

2.4.1 The Reflection Footprint

Here we compute the contribution of signal from a elliptical surface area onto a given point at depth d, the hydrophone location. The incident wave is assumed to be planar, as in Fig. 2.2. We apply Huygens' principle that each surface point emits a omni-directional wave. Fig. 2.3 illustrates the principle, where we have reflected the hydrophone using the reflection principle to facilitate the analysis.

We note that the rays generated by the elliptical surface that travel to the hydrophone at the apex of the cone in Fig. 2.3, are the same as those that would originate from the circular conical cut at right angles to the cylinder's axis. We denote the radius of this circle by $M_w/2$, where we call M_w the *mirror width*. The circular equivalent mirror, however, can be thought of as the surface of a cylindrical section of the planar incident wave field. We will now calculate the signal at the apex resulting from that circular surface instead, and translate the geometry back to the sea surface later. In essence both surfaces results form conical cut through the same cone, but the circular view is simpler to analyze.

Assume the uniform intensity across the circular area to be I. Then each annular region at radius x from the center, will contribute the same amount and phase of signal to the apex point, this amount is given by

$$I(x) \propto 2\pi x e^{j2\pi \frac{f}{c}\sqrt{x^2+d^2/\sin^2(\theta)}} \tag{2.12}$$

where f is the acoustic frequency, $c = 1500$ m/s is the speed of sound in water, d is the depth of the hydrophone and θ is the ray incident angle, as explained earlier. The quantity $I(x)$ is proportional to the intensity. The wave amplitude is proportional to x. The term $d^2/\sin^2(\theta)$ is the distance from the sea surface to the apex of the cone. The main effect in (2.12) is the phase shift that the signal experiences, which will cause the signal decorrelation. The minuscule amounts of amplitude attenuation differences between rays are ignored.

The complete signal at the hydrophone is now computed as

$$\begin{aligned} I_R(M_w) &= \int_0^{M_w/2} I(x)dx \\ &= 2\pi x \int_0^{M_w/2} e^{j2\pi\frac{f}{c}\sqrt{x^2+d^2/\sin^2(\theta)}}dx \end{aligned}$$

We can further express $I_R(M_w)$ as

$$\begin{aligned} I_R(M_w) = &\frac{c^2}{2\pi f^2}\left(1-\frac{2\pi j f}{c}d\right) \\ &\cdot\left(e^{j2\pi\frac{f}{c}d\sqrt{\frac{M_w^2}{4d^2}+\frac{1}{\sin^2(\theta)}}}\sqrt{\frac{M_w^2}{4d^2}+\frac{1}{\sin^2(\theta)}}-\frac{e^{j2\pi\frac{f}{c}\frac{d}{\sin(\theta)}}}{\sin(\theta)}\right) \end{aligned} \tag{2.13}$$

where we note that, while a closed form exists, it is not very readable.

For typical values, such as our experimental values of $f = 2048$ Hz, and d on the order of $40-50$ m, $2\pi fd/c \gg 1$, and we can simplify to

$$\begin{aligned} &I_R(M_w) = \\ &-j\frac{cd}{f}\left(e^{j2\pi\frac{f}{c}d\sqrt{\frac{M_w^2}{4d^2}+\frac{1}{\sin^2(\theta)}}}\sqrt{\frac{M_w^2}{4d^2}+\frac{1}{\sin^2(\theta)}}-\frac{e^{j2\pi\frac{f}{c}\frac{d}{\sin(\theta)}}}{\sin(\theta)}\right) \end{aligned}$$

Further noting that $M_w \ll 2d$, that is the mirror width will be significantly smaller then the hydrophone depth, otherwise we are in a near-field situation, where we can no longer assume ray-tracing to be accurate, we obtain our final approximation

$$I_R(M_w) \approx \frac{-jcd}{f\sin(\theta)}\left(e^{j2\pi\frac{f}{c}d\sqrt{\frac{M_w^2}{4d^2}+\frac{1}{\sin^2(\theta)}}}-e^{j2\pi\frac{f}{c}\frac{d}{\sin(\theta)}}\right). \tag{2.14}$$

Numerical comparisons between (2.15) and (2.13) show an excellent agreement.

We can use a normalized mirror width $m_w = M_w/(2d)$, and reduce the above equation to a single parameter equation

$$I_R(m_w) \approx \frac{-jcd}{f\sin(\theta)}\left(e^{j2\pi\frac{f}{c}d\sqrt{m_w^2+\frac{1}{\sin^2(\theta)}}}-e^{j2\pi\frac{f}{c}\frac{d}{\sin(\theta)}}\right). \tag{2.15}$$

Normalizing by d^2 we obtain the following proportionality for the received pressure power

$$\begin{aligned} P(m_w) &= \frac{|I_R(m_w)|^2}{d^2} \\ &\approx \frac{c^2}{f^2 \sin^2(\theta)} \left| e^{j2\pi \frac{f}{c} d\left(\sqrt{m_w^2 + \frac{1}{\sin^2(\theta)}} - \frac{1}{\sin(\theta)}\right)} - 1 \right|^2 \end{aligned} \tag{2.16}$$

We further manipulate $P(m_w)$ into

$$P(m_w) \approx \frac{c^2}{f^2 \sin^2(\theta)} \left| e^{j2\pi \frac{f}{c} d m_w^2 \Big/ \left(\sqrt{m_w^2 + \frac{1}{\sin^2(\theta)}} + \frac{1}{\sin(\theta)}\right)} - 1 \right|^2 \tag{2.17}$$

But since $m_w \ll 1$ and $\frac{1}{\sin(\theta)} > 1$, we can further approximate as follows

$$P(m_w) \approx \frac{c^2}{f^2 \sin^2(\theta)} \left| e^{j\pi \frac{f}{c} d m_w^2 \sin(\theta)} - 1 \right|^2 \tag{2.18}$$

and we realize that it is advantageous to renormalize the function by letting $\nu = \sqrt{\frac{fd}{c}}\, m_w \sqrt{\sin(\theta)}$ to obtain the normalized pressure power function

$$P(\nu) = \left| e^{j\pi\nu^2} - 1 \right|^2 \tag{2.19}$$

which does no longer contain the nuisance environmental variable d, f, c, and θ.

Fig. 2.4 shows (2.19) for $\nu < 1.5$, and we see that the function has a clear maximum at $\nu = 1$, and then rapidly decreases as near-field effects cause destructive interference. (For larger values of ν, the function $P(\nu)$ will start to oscillate.) We conclude that the coherence footprint is caused by the circular cylinder cut of radius M_w computed from $\nu = \sqrt{\frac{f}{dc}} \frac{M_w}{2} \sqrt{\sin(\theta)} = 1$, that is, a circluar area with a radius of $\sqrt{d}\sqrt{\frac{c}{f}}\sqrt{\frac{1}{\sin(\theta)}} = \sqrt{d\lambda / \sin(\theta)}$.

2.4.2 Correlation Regions

Let us return now to our original question of determining the correlation region of a path bundle, i.e., the surface area that contributes to the majority of the energy received at the hydrophone.

This area coincides with the area over which the received phases of different rays add coherently, as discussed in the previous section.

There are in general two effects that limit the correlation region: (i) As discussed above, the area of significant reflection is limited, and (ii) the correlation is also limited by the

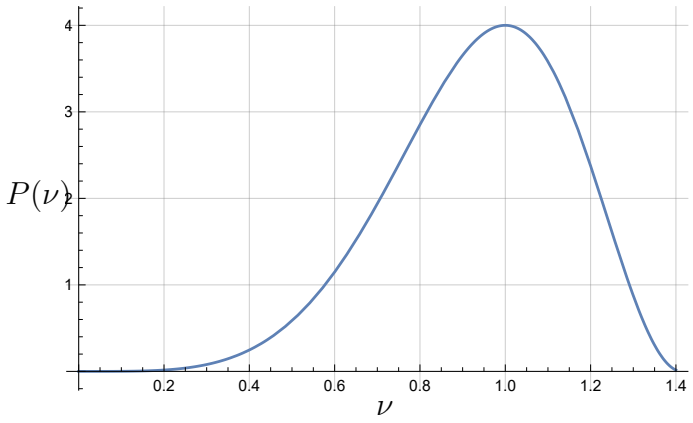

Figure 2.4: Plot of the normalized received pressure power as a function of ν.

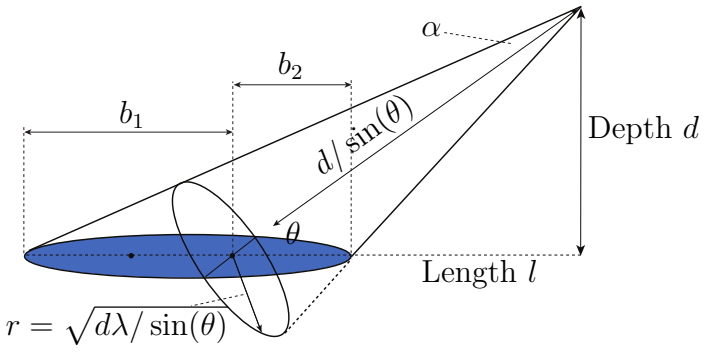

Figure 2.5: Illustration of the conical cut model to determine correlation regions.

geometric extent of the gravity waves that cause the time variations in the path bundles. The smaller region among the two will determine the correlation region.

We first return to the limit (i) by reconsidering the geometry discussed above, which is illustrated again in Fig. 2.5 for clarity. As can be seen, the sea surface cuts an ellipse out of the ray cone with major axis aligned with the path bundle direction. The way we chose to orient the cutting planes, the semi-latus rectum of the ellipse $l = M_w/2$, the radius of the circular reflection mirror discussed above.

To compute the extent of the elliptical footprint, we introduce the axis parts b_1 and b_2,

as well as the apex angle α. First we compute

$$\alpha = \tan^{-1}\left(\frac{r}{d}\sin(\theta)\right) = \tan^{-1}\left(\sqrt{\frac{\lambda\sin(\theta)}{d}}\right) \tag{2.20}$$

or in terms of the distance l of the reflection point from the receiver, we obtain

$$\alpha = \tan^{-1}\left(\sqrt{\frac{\lambda\cos(\theta)}{l}}\right) \to \tan^{-1}\left(\sqrt{\frac{\lambda}{l}}\right) . \tag{2.21}$$

Using the sine-law we further compute

$$b_1 = \frac{d\sin(\alpha)}{\sin(\theta)\sin(\theta+\alpha)}; \quad b_2 = \frac{d\sin(\alpha)}{\sin(\theta)\sin(\theta-\alpha)}; \tag{2.22}$$

and the diameter of the reflection footprint is given by

$$d_e = b_1 + b_2 = \frac{d\sin(\alpha)}{\sin(\theta)}\left(\frac{1}{\sin(\theta+\alpha)} + \frac{1}{\sin(\theta-\alpha)}\right) \tag{2.23}$$

Example: We assume a deployment depths of d =40 m, a reflection point distance l =150 m, and a frequency of f = 2048 Hz. These numbers will give us a radius of $M_w/2 = 5.25$ m, and a footprint extent of d_e =42 m.

Regarding point (ii), since the average gravity wave length varies from about 8 m to over 200 m, the correlation regions appear to be lower bounded by the refection footprint for most combinations of depths and reflection angles in shallow water, where, typically $\sqrt{d\lambda} <$ gravity wave periods.

2.4.3 Applications

The reflection footprints can now be used to estimate the amount of signal correlation in various situations. In Fig. 2.6 we consider the use of two hydrophones which may form part of vertical array and are separated by a distance of Δd. The overlap of their respective reflection footprints is where signals reach both hydrophones and the ratio between overlap and individual reflection footprint shall serve as estimate of the correlation between the two signals arriving at the two hydrophones.

Using basic geometry we find that the centers of the two elliptical footprints are offset from each other by the offset of the central reflection points using standard ray-tracing, leading to $\Delta r = \Delta d/\tan(\theta)$. For the example from above with l = 150 m and d = 40 m, then the footprints have axis of 40 m as discussed above.

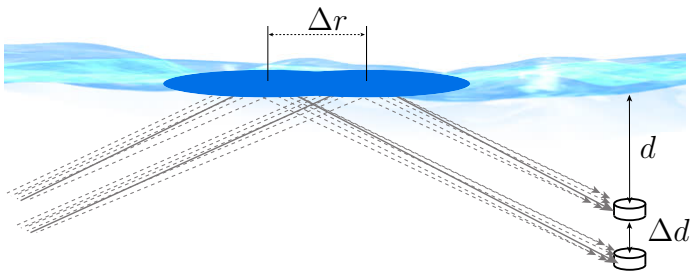

Figure 2.6: Correlation illustration of vertically separated hydrophones.

As a simplifying assumption, think for a moment of the reflection footprints as square areas, and near-by footprints lie on the diagonals of these squares. Then, the area shared by two footprints shrinks with the square of the separation between the two centers. In the example above with a hydrophone separation of $\Delta d = 0.33$ m, $\Delta r = 1.25$ m. With a reflection footprint diameter of $40m$, the expected correlation factor ρ would be given by

$$\rho = \left(\frac{d_e - \Delta r}{d_e}\right)^2 = \left(\frac{38.75}{40}\right)^2 = 0.94 \tag{2.24}$$

Using the same geometries, and the example of the VLA, correlation between the first and last hydrophone would be $\left(\frac{35}{40}\right)^2 = 0.76$.

Generically then, in order to achieve decorrelation between the signal of two hydrophone receivers, we need $\Delta r > d_e$, which leads to $\Delta d > d\, d_e/l$. In our example this would lead to a hydrophone separation of 11 m or larger. Since $d_e \propto \sqrt{d}$, the required separation for decorreation has an order relationship with depths as $\mathcal{O}(d^{3/2})$ where the exact proportionality factors depend on the geometry of the transmission environment as discussed here. However, we can conclude that deep-sea systems will practically never see a significant decorrelation of a given path over the hydrophone array, and only rather shallow deployments could achieve such a signal decorrelation.

2.5 Model Example and Experimental Results

In this section we consider an example channel measured in a sea trial experiment performed off the cost of Nova Scotia, Canada, during the summer of 2017. The distance between

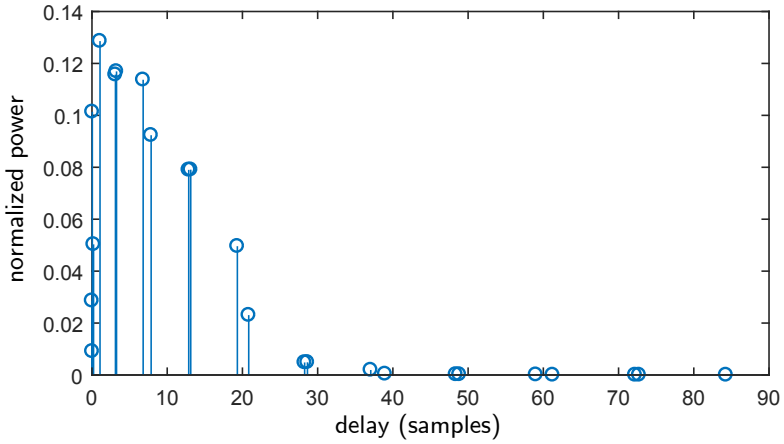

Figure 2.7: Normalized power-delay profile used to generate a model of St. Margaret's bay channel.

the transmitter and receiver was equal to 1 km, and the ocean depth was approximately 80 m. Both transmitter and receiver were at approximately 40 m depth. Hard bottom (gravel and sand composition) is expected in the measurement area according to Canadian oceanographic survey maps. The underwater acoustic transmission was performed using the carrier frequency $f_c = 2048$ Hz, bandwidth was set to $B = 320$ Hz and root-raised cosine filters with roll-off 0.25 have been used. The receive VLA consisted of five hydrophones separated by $d = 0.36$ m (half a wavelength).

Sampled power-delay profiles of the measured is given in Fig. 2.8 (top) where the horizontal axis represents the sampled (discrete) channel taps. Sampling time equals $T_s = 1/B = 0.0031$s. A clear multi-path propagation is exhibited by the channel. The first cluster of channel taps includes the direct, single bottom and single surface reflection paths. A dynamic sampled power-delay profile of the measured channel is given in Fig. 2.9. The overall RMS Doppler spread is equal to 0.44 Hz.

The modeled channel was obtained via Bellhop modeling of the channel power delay profile according to the communication channel geometry given by the measurement setup. The resulting (unsampled) normalized power-delay profile is given in Fig. 2.7 and a sampled discrete power-delay profile of the modeled channel is given in Fig. 2.8 (bottom). Both measured and modeled power-delay profiles consist of five clusters of significant channel taps. We notice that for the measured channel all channel taps, even these outside the clusters are non-zero. On the other hand for the modeled channel all non-zero taps are located within the clusters resulted from the channel paths (Fig. 2.7) and subsequent filtering.

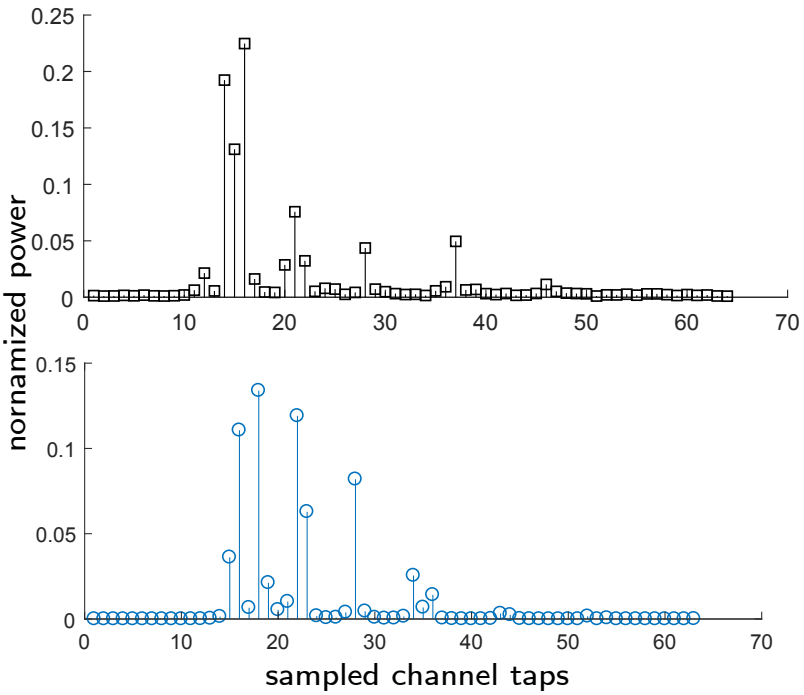

Figure 2.8: Sampled power-delay profile of measured (top) and modeled (bottom) St. Margaret's bay channel.

In order to set the Doppler spread for the channel we take one of the two approaches where the first approach is to set the Doppler spread for each channel path to the same value α RMS Doppler and use the distribution (2.3) to create the time fading according to the SOS process. The second approach would be to set α_l for path $l = 1, 2, \cdots, L_{\mathrm{p}}$ proportional to the number of surface bounces (see also [28]) since the Doppler spread tend to broaden with the number of surface bounces.

The average correlation between two neighboring hydrophones obtained for the measured channel was around $\rho = 0.8$. Hence we use the same value to set the correlation for the modeled channel. We use the same correlation values for all paths for the example modeled channel. This is also consistent with the values predicted by Section 4.8.

Finally we use the two channels, measured and modeled to test the OFDM communication system presented in [31]. The transmitter performs data modulation where the (uncoded) binary data is repeated, permuted and mapped to QPSK symbols in frequency domain. The data stream is superimposed bit by bit with the repeated pilot sequence designed in [38] and transmitted over the channel. Total channel power (sum of all taps squared) is normalized

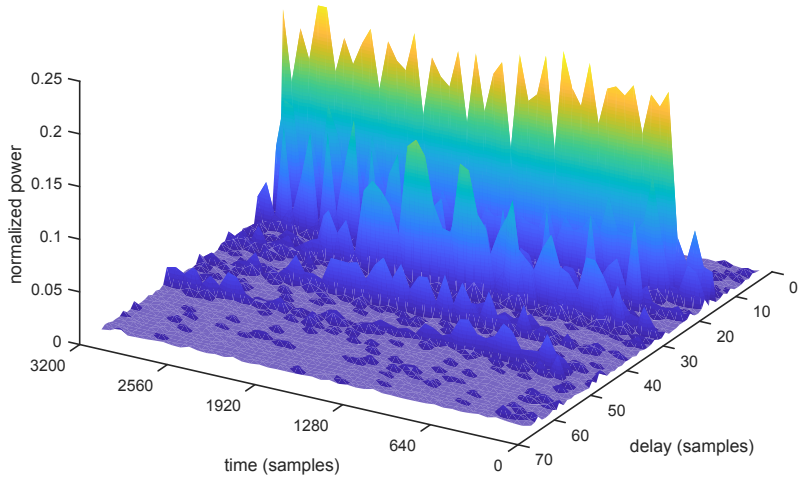

Figure 2.9: Time-variation of the measured normalized power-delay profile of St. Margaret's bay channel.

to one and Gaussian additive noise is considered to simulate the system at different signal-to-noise ratios (SNR)s. The OFDM size is 1024, repetition factor equals 4 and a pilot with time-domain period of 64 is considered where the pilot power is 10% of the signal power. The details are given in [31].

The receiver performs iterative channel estimation, equalization and data decoding [31]. At every iteration Kalman-based channel estimator in time domain is estimating the channel based on the pilot signal and partially decoded data. Soft data estimation and interference cancellation removing inter-carrier interference is performed after the channel estimation and using the obtained channel knowledge. Iterative decoding with 6 iterations has been performed for the two channels.

Fig. 2.10 demonstrates the uncoded bit-error rate of OFDM transmission utilizing the modeled and measured channels employing transmit and receive signaling described above. The modeled channel was set to have 0.44 Hz Doppler per path. The simulated BERs for both perfect channel knowledge assumption and channel estimation based iterative receivers are close for modeled and measured channels.

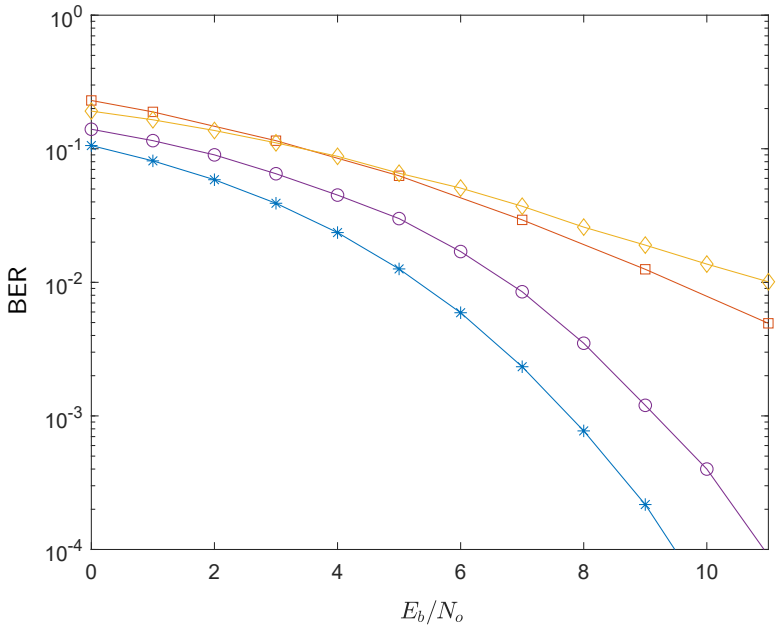

Figure 2.10: Bit-error rate for the iterative receiver obtained on measured (circles curve) and modeled (stars curve) St. Margaret's bay channel assuming perfect channel knowledge and performing 6 equalization iterations. Simulated BER for full iterative receiver which includes channel estimation are given by diamonds curve for the measured channel and squares curve for the modeled channel.

2.6 Conclusion

A dynamic underwater acoustic SIMO communications based on SOS principle is presented. The model reproduces the essential features of the underwater acoustic channel such as time and frequency selectivity, and incorporates transmit/receiver filtering. Special attention is given to modeling spatial channel correlation between the received hydrophones. A setup for modeling hydrophone correlation based on SOS is presented and the correlation values themselves are predicted using a study of correlation footprints presented in this chapter. Finally an example of a channel scenario is provided with both modeled and measured channel and the results of channel estimation and equalization demonstrate similar behavior on both measures and modeled channels.

hyperref amsmath graphicx bmcolor amsfonts float natbib soul algpseudocode appendix

Chapter 3

Acoustic Pressure Correlations in Deep Ocean with Applications to Multiple-Input Multiple-Output Underwater Communications

3.1 Abstract

We derive a general expression for the two-point space-time pressure field correlations generated by a polychromatic acoustic point source located not too far from the surface of a deep water basin. We show that in the monochromatic case, our results yield an explicit analytical expression for the two-point correlation function of acoustic Green's functions that characterize correlations among the individual transmitter-receiver links in a multiple-input multiple-output (MIMO) underwater communication system. In order to characterize the quality of the MIMO channel we quantify the degradation of the pressure correlations of the acoustic waves scattered by a free ocean surface due to the gravity wave velocity component and random ocean surface height fluctuations. The weak correlations of the surface-scattered waves are, however, offset by the presence of the direct propagation links between the transmitters and receivers. The direct link results in a significant overall correlation among the entries of the underwater MIMO channel matrix degrading its rank and limiting channel capacity.

3.2 Introduction

Understanding and modelling all aspects of the underwater sound propagation is a long-standing objective of the acoustic research that guides the fundamental oceanographic science and impacts a multitude of ocean technology applications. Recent advances in remote acoustic sensing and underwater acoustic communications research have led to the development of several sound propagation models, ranging from basic ones, aimed at computing the acoustic energy loss on wave propagation in the water, to comprehensive modelling of a multitude of underwater sound propagation aspects. The latter include multi-path sound propagation and acoustic wave scattering from the ocean seabed and free surface gravity

waves.

The widely utilized ray-tracing models such as Bellhop [3] are coached within the geometric acoustics framework that allows to determine a multi-path ray propagation profile. The latter can then be applied to model the impulse response of an acoustic communication channel, for instance. Further, the time variation of the impulse response modelling has been approached in a number of papers via modelling the acoustic wave scattering from the sea surface that was assumed to vary randomly in time. The authors of [4], for instance, attempted to model the actual acoustic wave scattering from the random sea surface by introducing, in a rather heuristic way, a random ensemble of micro-paths with prescribed time delays between the neighboring rays. A similar approach was followed in [5, 39, 6] for the case of modelling multiple-input multiple-output (MIMO) underwater acoustic signal propagation. An alternative approach was advocated in [40, 41] where instead of obtaining the scattered rays via micro-path ray tracing, an empirical scattering function, obtained from direct measurements, was incorporated into the model. The authors of [42] took a step further in the same direction by presenting a technique of stochastic replay whereby a time variation of the acoustic communication channel is generated from previously recorded channel measurements. The approach of superposition of a ray-tracing model and an empirical scattering function has been also considered for MIMO channels in [1] where an artificial parameter regulating correlations between individual transmit-receive propagation links have been introduced. In [43] a statistical model of random sea-surface variations was advanced and coupled with ray tracing to describe underwater sound propagation. A more fundamental, wave equation based approach to underwater acoustic signal propagation was also developed [44] within the parabolic equation approximation for relatively narrow-angle acoustic sources. Finally, the capacity of MIMO channel has been assessed based on coarse MIMO channel model approximations via correlated Rayleigh or Ricean matrices [30, 45] inspired by terrestrial wireless MIMO channel modelling.

However, while systematically treating the temporal fluctuations of the communication channel with variable degrees of success, the vast majority of existing underwater acoustic communication models incorporate the channel spatial fluctuations in a completely heuristic manner. To address the spatial and temporal fluctuations of the acoustic medium on equal footing, one has to go beyond ray tracing and explore the Green function of an acoustic field instead of the temporal impulse response function of an acoustic channel. To this

end, a normal mode expansion of the underwater Green function [46] serves as a convenient first step. Unfortunately, a purely numerical implementation of the method [47] is not conducive to gaining much physics insight. An alternative approach that combines a semi-analytic Kirchhoff theory to account for wave scattering from large surface wave swells and geometric optics approximation to obtain a rough estimate for the scattering cross-section was advocated in [48]. However, the acoustic pressure correlations were evaluated in a rather ad-hoc fashion, and in the end, a purely phenomenological exponential correlation function was argued to fit the measured data for pressure correlations at pairs of spatial points in the horizontal plane of the ocean. In addition the approach of [48] is limited to monochromatic sources and static ocean as no temporal pressure fluctuations are considered.

While point-to–point communication systems can use existing channel models discussed above, MIMO communication requires accurate space/time modelling. MIMO communications can open up a unique opportunity to take advantage of a multitude of spatially independent point-to-point communication channels between the transmitter/source and receiver [49]. In favorable channel conditions, the utilization of multiple transmitters and receivers leads to increased communication channel capacity which may scale linearly with the number of transmit/receive element pairs. The key question regarding a success of MIMO communication is the degree to which its promise can be exploited, or, in other words, the degree to which multiple point-to-point MIMO channels are uncorrelated in space. Answering this fundamental question necessitates the first-principles physics modelling of spatial correlations among individual transmitter-receiver links in multiple acoustic MIMO channels. The first-principles approach must rely on studying Green's function correlations at pairs of space-time points to establish the degree of MIMO channel correlations.

In this chapter, we determine space-time pressure correlations of the acoustic fields that are generated by monochromatic and polychromatic point sources located in the deep water not too far from the surface. In the monochromatic case, the result yields an analytical expression for the (normalized) correlation function of Green's functions at a pair of space-time points that characterizes the communication channel correlations. We discuss the influence of the random surface height fluctuations, as well as the Doppler effects associated with sound scattering from free surface gravity waves, on the spatial correlations of acoustic fields at pairs of observation points in the water. We then investigate the effects of source central frequency and bandwidth as well as receiver angular separation on the pressure correlation.

Finally, we study the interplay between the direct and indirect correlation components and conclude that the dominance of the direct signal propagation path undermines the efforts to create a high-rank high-capacity MIMO link.

3.3 Problem formulation and random Lloyd mirror model

We seek to determine two-point, space-time pressure correlations in the water, produced by an underwater acoustic source located not too far from the surface of a deep water reservoir such as a deep ocean or an ocean bay. In general, we expect the pressure correlations to be influenced by a multitude of uncontrollable factors related to the ocean free surface conditions, such as the gravity wave velocity and surface height distributions, as well as the ocean turbulence and its floor state (density, roughness and presence of sediments). The rich physics of underwater sound propagation and scattering necessitates a judicious choice of a *statistical* model to account for major factors affecting the pressure correlations. To this end, we shall make the follwoing simplifying assumptions.

1. The source is assumed to insonify the upper half space, $z \geq 0$ and to be located sufficiently far from the seabed.

2. The water is assumed to be very deep such that its depth far exceeds any characteristic spatial scale in the problem.

3. The source is assumed to be located not too far from the surface so that we can neglect sound speed stratification with the depth.

4. The water is assumed to be clear with no random sound scatterers.

5. The ocean surface is assumed sufficiently smooth such that its typical radius of the curvature far exceeds a characteristic wavelength of the source spectrum.

The first two assumptions imply that we can neglect scattering of sound from the seabed. Assumptions three and four are self-explanatory: we assume an isovelocity sound speed profile and neglect any effects due to volume scattering, either from random particles/copepods or ocean turbulence. The final assumption allows us to view the surface as locally flat with a random surface height with respect to the zero-crossing line $z = 0$. Our model can capture two major factors affecting the pressure correlations: the Doppler-induced correlation

fading due to random distribution of the surface wave velocities and the correlation decay due to random surface height fluctuations. We thus break the problem into two parts. First, we work in the gravity wave packet reference frame where the surface wave velocity is zero. Choosing our z axis in the vertical direction, the angular spectrum representation of a generic pressure wave in this frame reads

$$p(\mathbf{r}', t) = \int_0^\infty \frac{d\omega}{2\pi}\, e^{-i\omega t} \int \frac{d^2k_\perp}{2\pi}\, \mathcal{A}(\mathbf{k}_\perp, \omega) e^{i(\mathbf{k}_\perp \cdot \mathbf{r}'_\perp \pm k_z z')}, \tag{3.1}$$

where

$$k_z = \sqrt{\omega^2/c_s^2 - k_\perp^2}, \tag{3.2}$$

and all primed variables refer to the wave packet reference frame; $\mathcal{A}(\mathbf{k}_\perp, \omega)$ is the angular spectrum of our source, $\pm$ indicates the propagation direction of a constituent plane wave into the upper $(+)$ or lower $(-)$ half-space. Hereafter, we drop the plane wave components propagating downward and designate all vector components in the z-direction (depth) with the subscript " $\parallel$ " while all vector components in the plane perpendicular to the z-direction come with the subscript "$\perp$". Second, we transform to the laboratory frame and perform averages over statistical distributions of wave velocities and heights to determine the second-order pressure correlations at a pair of space-time points.

As the source is in deep water, we can treat sound scattering within the framework of a random Lloyd mirror model. This conceptually simple model implies that there are only two paths that matter: the direct path from the source to a receiver and the one involving a single reflection of sound from the random ocean surface. The second contribution can be thought of as coming from an image source above the surface so that the overall pressure at any point under water can be expressed as

$$p(\mathbf{r}', t) = \int_0^\infty \frac{d\omega}{2\pi}\, e^{-i\omega t} \int \frac{d^2k_\perp}{2\pi}\, \mathcal{A}(\mathbf{k}_\perp, \omega) e^{i\mathbf{k}_\perp \cdot \mathbf{r}'_\perp} [e^{ik_z(z'-z_0)} - e^{-ik_z(z'-z_*)}], \tag{3.3}$$

where z_0 and z_* define the vertical coordinates of the source and image, respectively; the source is assumed to be located on the z-axis. Next, imposing a pressure release condition on the surface,

$$p(\mathbf{r}', t)|_{z'=h} = 0, \tag{3.4}$$

we can easily determine the image location,

$$h - z_0 = -(h - z_*) \implies z_* = 2h - z_0. \tag{3.5}$$

Thus,

$$p(\mathbf{r}',t)=\int_0^\infty \frac{d\omega}{2\pi}\,e^{-i\omega t}\int \frac{d^2k_\perp}{2\pi}\,\mathcal{A}(\mathbf{k}_\perp,\omega)e^{i\mathbf{k}_\perp\cdot\mathbf{r}'_\perp}[e^{ik_z(z'-z_0)}-e^{-ik_z(z'+z_0-2h)}]. \tag{3.6}$$

3.4 Space-time acoustic pressure correlations

We may now transform from the gravity wave packet frame to the laboratory frame. To this end, we notice that the first term on the r.h.s, of Eq. (3.6) represents the contribution directly propagating from the source to the receiver without having ever interacted with the random surface. Hence, in the first term, $\mathbf{r}'_\perp=\mathbf{r}_\perp$ and $z'=z$. At the same time, the coordinates of the wave scattered by the moving surface in the laboratory frame read

$$\mathbf{r}_\perp=\mathbf{r}'_\perp+\mathbf{v}_\perp t, \qquad z=z'+v_\parallel t, \tag{3.7}$$

where the unprimed coordinates correspond to the laboratory frame; $\mathbf{v}_\perp$ and $\mathbf{v}_\parallel=v_\parallel\mathbf{e}_z$ are gravity wave velocities in the ocean surface plane and in the vertical direction, respectively. We have tacitly assumed that since the speed of any gravity wave is much smaller than the speed of sound, we can neglect the change in either vertical or horizontal velocity components of an ensemble of gravity waves over the course of their interaction with any acoustic plane wave making up the angular spectrum of the source. On substituting from Eq. (3.7) into (3.6) and rearranging terms we arrive at

$$p(\mathbf{r},t)=\int_0^\infty \frac{d\omega}{2\pi}\,e^{-i\omega t}\int \frac{d^2k_\perp}{2\pi}\,\mathcal{A}(\mathbf{k}_\perp,\omega)e^{i\mathbf{k}_\perp\cdot\mathbf{r}_\perp}[e^{ik_z(z-z_0)}-e^{i(k_zv_\parallel-\mathbf{k}_\perp\cdot\mathbf{v}_\perp)t}e^{-ik_z(z+z_0-2h)}]. \tag{3.8}$$

The first term on the r.h.s., of (3.8) is just the pressure generated by the source at the point $\mathbf{r}$ at a time t. Thus,

$$p(\mathbf{r},t)=p_0(\mathbf{r},t)-\int_0^\infty \frac{d\omega}{2\pi}\,e^{-i\omega t}\int \frac{d^2k_\perp}{2\pi}\,\mathcal{A}(\mathbf{k}_\perp,\omega)e^{i\mathbf{k}_\perp\cdot\mathbf{r}_\perp}e^{i(k_zv_\parallel-\mathbf{k}_\perp\cdot\mathbf{v}_\perp)t}e^{-ik_z(z+z_0-2h)}. \tag{3.9}$$

A straightforward analysis shows that the cross-terms involving directly propagated and scattered plane waves nearly vanish in the far zone, $k_jr_j\gg 1$, $(j=1,2)$ because the acoustic paths add up, resulting in highly oscillating contributions which should cancel out upon plane wave superpositions. We can then determine the effective correlation function

$$\Gamma(\mathbf{r}_1,t_1;\mathbf{r}_2,t_2)\equiv\overline{\langle[p^*(\mathbf{r}_1,t_1)-p_0^*(\mathbf{r}_1,t_1)][p(\mathbf{r}_2,t_2)-p_0(\mathbf{r}_2,t_2)]\rangle}, \tag{3.10}$$

where the bar indicates averaging over the ensemble of surface wave packet velocities and the angle brackets that over the surface wave heights which are assumed to be independent. The overall pressure correlation function will then be simply

$$\Gamma_{\rm tot}(\mathbf{r}_1,t_1;\mathbf{r}_2,t_2) \equiv \overline{\langle [p^*(\mathbf{r}_1,t_1)p(\mathbf{r}_2,t_2)\rangle} \simeq p_0^*(\mathbf{r}_1,t_1)p_0(\mathbf{r}_2,t_2) + \Gamma(\mathbf{r}_1,t_1;\mathbf{r}_2,t_2). \tag{3.11}$$

It follows that

$$\Gamma(\mathbf{r}_1,t_1;\mathbf{r}_2,t_2) = \int_0^\infty \frac{d\omega_1}{2\pi}\int_0^\infty \frac{d\omega_2}{2\pi}\int \frac{d^2k_{1\perp}}{2\pi}\int \frac{d^2k_{2\perp}}{2\pi}\, e^{i(\omega_1 t_1-\omega_2 t_2)} e^{i(\mathbf{k}_{2\perp}\cdot\mathbf{r}_{2\perp}-\mathbf{k}_{1\perp}\cdot\mathbf{r}_{1\perp})} e^{ik_{1\,z}(z_1+z_0)}$$
$$\times\, e^{-ik_{2\,z}(z_2+z_0)} \overline{e^{i(\mathbf{k}_{1\perp}t_1-\mathbf{k}_{2\perp}t_2)\cdot\mathbf{v}_\perp}} \langle e^{2ih(k_{2\,z}-k_{1\,z})}\rangle \overline{e^{i(k_{2\,z}t_2-k_{1\,z}t_1)v_\parallel}} \mathcal{A}^*(\mathbf{k}_{1\perp},\omega_1)\mathcal{A}(\mathbf{k}_{2\perp},\omega_2). \tag{3.12}$$

We are left to evaluate the characteristic functions of the gravity wave velocities and wave height distributions. Unless the ocean is in an extreme stormy condition, the wave height PDF is reliably Gaussian, as the surface height at a given point is determined by many independent contributions from the neighbourhood of the point. Averaging then over the Gaussian distribution of wave heights gives

$$\langle e^{2ih(k_{2\,z}-k_{1\,z})}\rangle = e^{-2\sigma_{\rm h}^2(k_{2\,z}-k_{1\,z})^2}, \tag{3.13}$$

where $\sigma_{\rm h}$ is an rms width of wave heights. Further, the vertical velocity distribution can be modelled by assuming that

$$v_\parallel = \overline{v}_\parallel \cos\theta, \tag{3.14}$$

where θ is a random phase of the wave train, uniformly distributed in the interval, $0 \le \theta \le 2\pi$. This generic distribution captures the key fact that the vertical velocity oscillates back an forth harmonically with the overall random phase of the wave with a characteristic average amplitude $\overline{v}_\parallel$. Averaging over the vertical velocity distribution yields a Doppler shift due to its spread as

$$\overline{e^{i(k_{2\,z}t_2-k_{1\,z}t_1)v_\parallel}} = J_0[(k_{2\,z}t_2 - k_{1\,z}t_1)\overline{v}_\parallel], \tag{3.15}$$

where $J_0(x)$ is a Bessel function of the first kind of order zero.

Let us next average over the group velocity of a gravity wave packet in the surface plane ($xy-$plane). The first requirement for the group velocity distribution PDF is rotational symmetry in the xy-plane, which follows from the random direction of a driving wind velocity. Thus the group velocity PDF should then depend only on the magnitude of the group velocity, $\mathcal{P}(\mathbf{v}_\perp) = \mathcal{P}(v_\perp)$. Each wave packet consists of a large number of gravity waves, propagating

with random phase velocities determined by the local wind gusts. Hence, it is reasonable to assume, by virtue of the central limit theorem, that the in-plane wave velocity PDF factorizes into a product of two uncorrelated Gaussian distributions for each Cartesian component of the velocity. By implication, the PDF of the in-plane velocity $v_\perp$ is a Rayleigh one,

$$\mathcal{P}(v_\perp, \phi) = (v_\perp/\sigma_\perp^2) e^{-v_\perp^2/2\sigma_\perp^2}. \tag{3.16}$$

Here $\sigma_\perp$ is a group velocity parameter related to the average group velocity through $\overline{v}_\perp = \sigma_\perp\sqrt{\pi/2}$. It follows from Eqs. (3.16) upon integrating either in Cartesian or in polar coordinates that

$$\overline{e^{i(\mathbf{k}_{1\perp}t_1 - \mathbf{k}_{2\perp}t_2)\cdot\mathbf{v}_\perp}} = e^{-(\mathbf{k}_{1\perp}t_1 - \mathbf{k}_{2\perp}t_2)^2\sigma_\perp^2/2}. \tag{3.17}$$

Finally, on combining Eqs. (3.13), (3.15) and (3.17), we arrive at the result,

$$\begin{aligned}\Gamma(\mathbf{r}_1, t_1; \mathbf{r}_2, t_2) = &\int_0^\infty \frac{d\omega_1}{2\pi}\int_0^\infty \frac{d\omega_2}{2\pi}\int \frac{d^2k_{1\perp}}{2\pi}\int \frac{d^2k_{2\perp}}{2\pi}\, e^{i(\omega_1 t_1 - \omega_2 t_2)} e^{i(\mathbf{k}_{2\perp}\cdot\mathbf{r}_{2\perp} - \mathbf{k}_{1\perp}\cdot\mathbf{r}_{1\perp})} e^{ik_{1z}(z_1+z_0)} \\ &\times e^{-ik_{2z}(z_2+z_0)} e^{-(\mathbf{k}_{1\perp}t_1 - \mathbf{k}_{2\perp}t_2)^2\sigma_\perp^2/2} J_0[(k_{2z}t_2 - k_{1z}t_1)\overline{v}_\parallel] e^{-2\sigma_h^2(k_{2z}-k_{1z})^2} \mathcal{A}^*(\mathbf{k}_{1\perp}, \omega_1)\mathcal{A}(\mathbf{k}_{2\perp}, \omega_2)\end{aligned} \tag{3.18}$$

In practice, it is convenient to introduce a normalized correlation function as

$$\gamma(\mathbf{r}_1, t_1; \mathbf{r}_2, t_2) = \frac{\Gamma_{\rm tot}(\mathbf{r}_1, t_1; \mathbf{r}_2, t_2)}{\sqrt{\Gamma_{\rm tot}(\mathbf{r}_1, t_1; \mathbf{r}_1, t_1)\Gamma_{\rm tot}(\mathbf{r}_2, t_2; \mathbf{r}_2, t_2)}}. \tag{3.19}$$

We point out that some of our Doppler-induced correlation factors resemble those derived heuristically in [4] that provides albeit an oversimplified, yet computationally attractive platform that has influenced a generation of signal processing papers in underwater acoustic communications. We note, however, that [4] model lacks solid physics basis. In particular, it entirely misses the fact that spatial and temporal correlations among plane wave components of the angular spectrum are strongly coupled by virtue of acoustic wave propagation as is evidenced by Eq. (3.18). Hence, one cannot simply ignore spatial dependence and introduce it later in a heuristic manner. In addition, [4] ignores Doppler broadening effects associated with a velocity spread of surface gravity waves in the horizontal plane of the ocean, which can be quite important as we estimate below and demonstrate in our numerical simulations.

3.5 Plane wave scattering and order-of-magnitude estimates

Let us briefly consider the physics of single plane-wave correlations. Consider a plane wave of frequency ω_* with the wave vector $\mathbf{k}_*$. If the angular spectrum consisted of just this plane

wave, implying that $\mathcal{A}(\mathbf{k}_\perp,\omega)=\delta(\mathbf{k}_\perp-\mathbf{k}_{*\perp})\delta(\omega-\omega_*)$, its self-correlation at two space-time points would be given by $\Gamma(\mathbf{r}_1,t_1;\mathbf{r}_2,t_2)\propto e^{-k_{*\perp}^2\sigma_\perp^2(t_1-t_2)^2/2}J_0[k_{*z}\overline{v}_\parallel(t_1-t_2)]$. It follows that the plane wave scattered in a given direction remains self-correlated over a typical correlation time $\tau_c\sim\min(k_{*z}^{-1}\overline{v}_\parallel^{-1},k_{*\perp}^{-1}\sigma_\perp^{-1})$ due to the Doppler broadening. Notice that characteristic self-correlation times are **different** for different plane waves within the angular spectrum of the source, implying a strong coupling of space-time correlations, the point missed in [4]. Let us now make some order-of-magnitude estimates. We first consider the appropriate range of sonar frequencies. Recent ultrasonic underwater communication experiments were performed in the frequency range $5\leq\nu_0\leq 20$ kHz [4], whereas acoustic sensing for oceanographic purposes is typically carried out in the range 24 kHz $\leq\nu_0\leq$ 1.2 MHz. [50]. Let us then assume a range 5 kHz $\leq\nu_0\leq$ 1 MHz to enable both possibilities. Notice that even at the lower end of the frequency spectrum, the sound wavelength $\lambda_0\sim 30$ cm is much shorter than a characteristic ocean surface radius of the curvature, typically of the order of a few meters even in a stormy weather. Further, a typical vertical wave velocity can be estimated from its amplitude a and gravity wave frequency $\omega_{\rm gw}$ as $\overline{v}_\parallel\sim\omega_{\rm gw}a$, where we can estimate $\omega_{\rm gw}\sim\sqrt{gk_{\rm gw}}\sim\sqrt{2\pi g/\lambda_{\rm gw}}$ in the deep water limit [51]. Table 3.1 presents the gravity wave $\sigma_\perp$,$\bar{v}_{||}$ and height $\sigma_{\rm h}$ parameters as a function of sea state. We employ Joint North Sea Wave Observation Project (JONSWAP) spectrum [52] to calculate the relationships between different sea state parameters (see Appendix B).

3.6 Far-field behavior and Green's function correlations

Since typical observations in acoustics happen in the far zone, $kr\gg 1$, Eq. (3.18) can be substantially simplified by performing a stationary-phase integration over the angular spectrum. To this end, we re-write Eq. (3.18) as

$$\Gamma(\mathbf{r}_1,t_1;\mathbf{r}_2,t_2)=\int_0^\infty\frac{d\omega_1}{2\pi}\int_0^\infty\frac{d\omega_2}{2\pi}\,e^{i(\omega_1t_1-\omega_2t_2)}\Phi(\mathbf{r}_1,t_1;\mathbf{r}_2,t_2;\omega_1,\omega_2),\tag{3.20}$$

where

$$\begin{aligned}\Phi(\mathbf{r}_1,t_1;\mathbf{r}_2,t_2;\omega_1,\omega_2)\;=\;&\int_{|\mathbf{f}_{1\perp}|\leq 1}\left(\frac{d^2f_{1\perp}}{2\pi}\right)\int_{|\mathbf{f}_{2\perp}|\leq 1}\left(\frac{d^2f_{2\perp}}{2\pi}\right)\,k_1^2k_2^2\,\mathcal{A}^*(k_1\mathbf{f}_{1\perp},\omega_1)\mathcal{A}(k_2\mathbf{f}_{2\perp},\omega_2)\\&\times C(\mathbf{f}_{1\perp},\mathbf{f}_{2\perp})\,e^{-[k_1[\mathbf{f}_{1\perp}\cdot\mathbf{r}_{1\perp}-f_{1\,\mathrm{z}}(z_1+z_0)]}\,e^{ik_2[\mathbf{f}_{2\perp}\cdot\mathbf{r}_{2\perp}-f_{2\,\mathrm{z}}(z_2+z_0)]}.\end{aligned}\tag{3.21}$$

Here the slowly-varying correlation function reads

$$C(\mathbf{f}_{1\perp},\mathbf{f}_{2\perp})=e^{-(k_1\mathbf{f}_{1\perp}t_1-k_2\mathbf{f}_{2\perp}t_2)^2\sigma_\perp^2/2}J_0[(k_2f_{2\,\mathrm{z}}t_2-k_1f_{1\,\mathrm{z}}t_1)\overline{v}_\parallel]e^{-2\sigma_{\rm h}^2(k_2f_{2\,\mathrm{z}}-k_1f_{1\,\mathrm{z}})^2},\tag{3.22}$$

where we introduced

$$\mathbf{k}_{j\perp} = k_j \mathbf{f}_{j\perp}, \qquad f_{j\,\mathrm{z}} = \sqrt{1 - f_{j\perp}^2}, \tag{3.23}$$

and $k_j = \omega_j / c_\mathrm{s}$, $j = 1, 2$. The integral (3.21) can be evaluated by the standard stationary-phase technique with the result being a straightforward generalization of [53, 45]

$$\Phi(\mathbf{r}_1, t_1; \mathbf{r}_2, t_2; \omega_1, \omega_2) = k_1 k_2 s_{1\,\mathrm{z}} s_{2\,\mathrm{z}}\, \mathcal{A}^*(\mathbf{s}_{1\perp}, \omega_1) \mathcal{A}(\mathbf{s}_{2\perp}, \omega_2)\, C(\mathbf{s}_{1\perp}, \mathbf{s}_{2\perp}) \frac{e^{i(k_2 r_2 - k_1 r_1)}}{r_1 r_2}, \tag{3.24}$$

where

$$C(\mathbf{s}_{1\perp}, \mathbf{s}_{2\perp}) = e^{-(k_1 t_1 \mathbf{s}_{1\perp} - k_2 t_2 \mathbf{s}_{2\perp})^2 \sigma_\perp^2 / 2} J_0[(k_2 t_2 s_{2\,\mathrm{z}} - k_1 t_1 s_{1\,\mathrm{z}}) \overline{v}_\parallel] e^{-2\sigma_\mathrm{h}^2 (k_2 s_{2\,\mathrm{z}} - k_1 s_{1\,\mathrm{z}})^2}. \tag{3.25}$$

Here we introduced a two-dimensional vector $\mathbf{s}_\perp$ and s_z viz.,

$$\mathbf{s}_{j\perp} = \sin\theta_j (\mathbf{e}_x \cos\phi_j + \mathbf{e}_y \sin\phi_j); \qquad s_z = \cos\theta_j. \tag{3.26}$$

In physics terms, our result implies that the plane waves propagating from the image source along the lines-of-sight connecting the image source and the two receivers, $s_{j\,\mathrm{z}} = (z_j + z_0)/r_{*j} \simeq \cos\theta_j$, $r_{*j} = \sqrt{x_j^2 + y_j^2 + (z + z_0)^2} \simeq r_j$ make dominate contributions to the correlation function in the far zone of the source. We also assumed that the receivers are located far enough from the source such that $z_0, z_j \ll r_j$, $(j = 1, 2)$.

We now specify to a polychromatic spherical wave as a conventional broadband acoustic source. The angular spectrum of such a source is well-known [46, 45]

$$\mathcal{A}(\mathbf{k}_{j\perp}, \omega) = \frac{i\tilde{F}(\omega)}{k_j s_{j\,\mathrm{z}}} = \frac{i\tilde{F}(\omega)}{k_j \sqrt{1 - s_{j\perp}^2}} = \frac{i\tilde{F}(\omega)}{k_j \cos\theta_j}, \tag{3.27}$$

where $\tilde{F}(\omega)$ is a spectral amplitude of the source. On substituting from Eq. (3.27) into (3.25) and making use of (3.21) through (3.24) and (3.26), we arrive at

$$\begin{aligned}\Gamma(\mathbf{r}_1, t_1; \mathbf{r}_2, t_2) = \frac{1}{r_1 r_2} \int_0^\infty \frac{d\omega_1}{2\pi}\, e^{i\omega_1 (t_1 - r_1/c_\mathrm{s})} \tilde{F}^*(\omega_1) \int_0^\infty \frac{d\omega_2}{2\pi} e^{-i\omega_2 (t_2 - r_2/c_\mathrm{s})} \tilde{F}(\omega_2) \\ \times e^{-(k_1 t_1 \mathbf{s}_{1\perp} - k_2 t_2 \mathbf{s}_{2\perp})^2 \sigma_\perp^2 / 2} J_0[(k_2 t_2 s_{2\,\mathrm{z}} - k_1 t_1 s_{1\,\mathrm{z}}) \overline{v}_\parallel] e^{-2\sigma_\mathrm{h}^2 (k_2 s_{2\,\mathrm{z}} - k_1 s_{1\,\mathrm{z}})^2}.\end{aligned} \tag{3.28}$$

Finally, on combining with the directly propagated contribution, we obtain

$$\Gamma_\mathrm{tot}(\mathbf{r}_1, t_1; \mathbf{r}_2, t_2) = \frac{F^*(t_1 - r_1/c_\mathrm{s}) F(t_2 - r_2/c_\mathrm{s})}{r_1 r_2} + \Gamma(\mathbf{r}_1, t_1; \mathbf{r}_2, t_2), \tag{3.29}$$

where we introduced a source temporal profile viz.,

$$F(t) = \int_0^\infty \frac{d\omega}{2\pi}\, \tilde{F}(\omega) e^{-i\omega t}. \tag{3.30}$$

Next, we specialize to a realistic case of grazing incidence which corresponds to most actual remote-sensing and underwater communication experiments near surface. The polar angles the observation points (receivers) make with the normal are then in the vicinity of $\pi/2$. As in oceanography the polar angles are often measured with respect to the horizon, we can introduce the complementary angle, $\psi = \pi/2 - \theta$. Thus, whenever $\theta \simeq \pi/2$, it follows that $\sin\theta_j \simeq 1$ and $\cos\theta_j \simeq \psi_j$, implying that

$$\mathbf{s}_{j\perp} \simeq \mathbf{e}_x \cos\phi_j + \mathbf{e}_y \sin\phi_j; \qquad s_{j\,\mathrm{z}} \simeq \psi_j. \tag{3.31}$$

It then follows at once that

$$\Gamma(\mathbf{r}_1, t_1; \mathbf{r}_2, t_2) = \frac{1}{r_1 r_2} \int_0^\infty \frac{d\omega_1}{2\pi}\, e^{i\omega_1(t_1 - r_1/c_\mathrm{s})} \tilde{F}^*(\omega_1) \int_0^\infty \frac{d\omega_2}{2\pi} e^{-i\omega_2(t_2 - r_2/c_\mathrm{s})} \tilde{F}(\omega_2)$$
$$\times e^{-\sigma_\perp^2 \chi(k_1,t_1,k_2,t_2,\Delta\phi)/2} J_0[(k_2 t_2 \psi_2 - k_1 t_1 \psi_1)\overline{v}_\parallel] e^{-2\sigma_\mathrm{h}^2 (k_2\psi_2 - k_1\psi_1)^2}; \tag{3.32}$$

where we introduced the notations

$$\chi(k_1, t_1, k_2, t_2, \phi_1 - \phi_2) = k_1^2 t_1^2 + k_2^2 t_2^2 - 2k_1 k_2 t_1 t_2 \cos\Delta\phi, \qquad \Delta\phi = \phi_1 - \phi_2. \tag{3.33}$$

To gain physical insight, we first examine a strictly monochromatic spherical wave with the spectrum in the form of a delta-function, $\tilde{F}(\omega) \propto \delta(\omega - \omega_0)$. In this case, the acoustic field is due to a monochromatic point source and hence is given by the Green function, $G(\mathbf{r}, t; z_0, 0)$. It follows that the total correlation function is equivalent to the second-order correlation function of Green's functions, $\Gamma_\mathrm{tot}(\mathbf{r}_1, t_1, \mathbf{r}_2, t_2) = \overline{\langle G(\mathbf{r}_1, t_1; z_0, 0)) G(\mathbf{r}_2, t_2; z_0, 0)\rangle}$. We can then readily obtain the normalized correlation function of Green's functions analytically by substituting the delta-function spectrum into Eq. (3.32) and carrying out trivial integrations. It then follows from Eqs. (3.19), (3.29), and (3.32) that

$$|\gamma_\mathrm{G}(\mathbf{r}_1, t_1, \mathbf{r}_2, t_2)| = \tfrac{1}{2}\left\{1 + e^{-k_0^2\sigma_\perp^2[t_1^2 + t_2^2 - 2t_1 t_2 \cos\Delta\phi]/2} J_0[k_0\overline{v}_\parallel(t_1\psi_1 - t_2\psi_2)] e^{-2k_0^2\sigma_\mathrm{h}^2(\Delta\psi)^2}\right\}, \tag{3.34}$$

where the subscript "G" stands for Green's function and we introduced $k_0 = \omega_0/c_\mathrm{s}$ and $\Delta\psi = \psi_1 - \psi_2$. Eq. (3.34) no longer depends on the source particulars and it is a function of the underwater acoustic communication channel.

In MIMO communication practice, we typically interrogate all the channels simultaneously. Thus, we are interested in equal-time acoustic correlations. Setting, $t_1 = t_2 = t$ in Eq. (3.34), we arrive at once at

$$|\gamma_\mathrm{G}(\mathbf{r}_1, \mathbf{r}_2, t)| = \tfrac{1}{2}\left[1 + e^{-2k_0^2\sigma_\perp^2 t^2 \sin^2(\Delta\phi/2)} J_0(k_0\overline{v}_\parallel t\Delta\psi) e^{-2k_0^2\sigma_\mathrm{h}^2(\Delta\psi)^2}\right]. \tag{3.35}$$

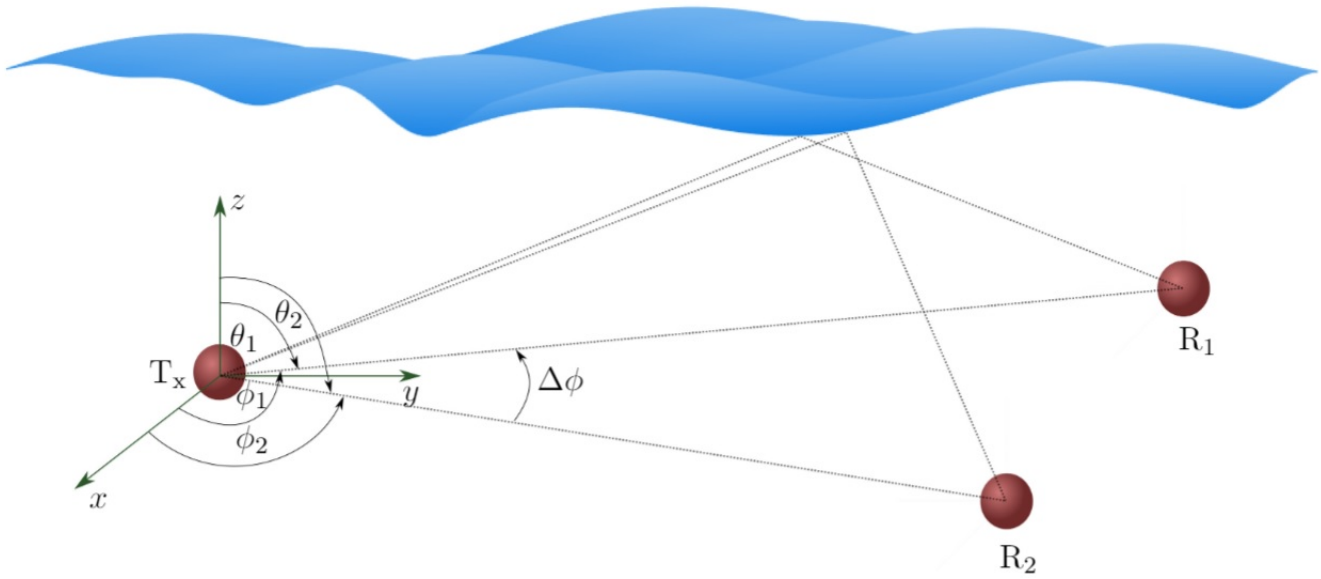

Figure 3.1: The horizontal array and the respective propagation model.

Let us focus on a pair of receivers located at approximately the same distance d from the source. We consider the correlations between the two receivers at the time the acoustic wave arrives at each receiver, $t = r/c_{\mathrm{s}}$. We can infer from Eq. (3.35) that the in-plane and vertical channel correlations are characterized by two (dimensionless) angular correlation scales of the order of

$$\begin{aligned} \sigma_\phi &\sim \frac{c_{\mathrm{s}}/\sigma_\perp}{k_0 r} \\ \sigma_\psi &\sim \min\left(\frac{c_{\mathrm{s}}/\overline{v}_\parallel}{k_0 r}, \frac{1}{k_0 \sigma_{\mathrm{h}}}\right). \end{aligned} \tag{3.36}$$

We can then infer from Eq. (3.36) that due to the space-time correlation coupling, we can control the azimuthal angular correlations by adjusting the communication channel length r.

The behavior of the polar angle correlation scale is more subtle as it is determined by a relative strength of wave height correlations, the communication channel length, and the magnitude of vertical gravity wave velocity fluctuations. In the following section, we present numerical examples illustrating various situations.

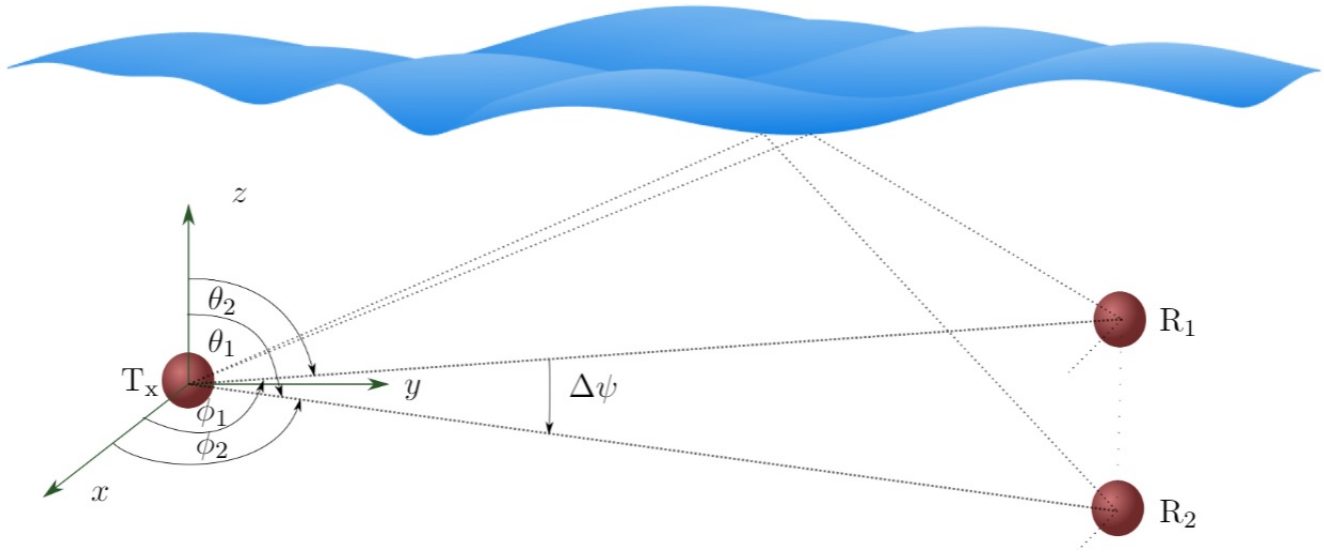

Figure 3.2: Propagation model for the vertical array.

3.7 Numerical results

In this section, we present a numerical evaluation of the spatio-temporal pressure wave correlation for two types of acoustic sources. We start (in Section 3.7.1) with considering a transmitter equipped with a monochromatic signal source which emits a pressure wave with frequency $\omega_0 = 2\pi\nu_0$ or equivalently is characterized by an impulse function $\delta(\omega - \omega_0)$. The second source we consider is a polychromatic source discussed in Section 3.7.2) and characterized by a raised cosine acoustic pulse spectral profile, shown in Fig. 3.7, frequently used in underwater communication transmitters.

The receiver is a two-hydrophone array positioned either vertically or horizontally with respect to the sea surface. We assume that the hydrophones are located at the same distance $r_1 = r_2 = r$ from the transmitter. They are positioned in a way that the direct pressure wave front, emitted by transmitter, arrives at both receivers at the same time $t_1 = t_2 = t$. The horizontal array placement is shown in Fig. 3.1 where both receivers lie in the xy-plane with angles $\theta_1 = \theta_2 = \pi/2$, or $\psi_1 = \psi_2 = 0$. The magnitude of the resulting normalized correlation function $|\gamma_{\mathrm{G}}|$ depends on the angular difference $\Delta\phi = \phi_2 - \phi_1$ and the arrival time t.

The vertical array shown in Fig. 3.2 consists of two hydrophones located in yz plane so that the angles $\phi_1 = \phi_2 = \pi/2$. Similar to the horizontal case, the normalized correlation $|\gamma_{\mathrm{G}}|$ depends on the angular difference $\Delta\theta = \theta_2 - \theta_1 = \Delta\psi$ and the time t. We choose

BEAUFORT NUMBER	**1**	**2**	**3**	**4**	**5**
Average Wind Speed U_{avg} (m/s)	0.90	2.45	4.40	6.70	9.35
Average Significant Height H_{s} (m)	0.182	0.364	1.091	1.820	3.640
Average Height H_{avg} (m)	0.1	0.2	0.6	1.0	2.0
Fetch Distance F (km)	153.9	83.05	231.7	277.6	570.2
Average Wave Period T_{avg} (sec)	3.226	3.667	6.276	7.669	10.894
Wave Height S.deviation σ_{h} (m)	0.062	0.125	0.375	0.626	1.253
Average Group Velocity $\bar{v}_{\perp}$ (m/s)	5.032	5.721	9.790	11.962	16.992
Group Velocity Parameter $\sigma_{\perp}$ (m/s)	4.015	4.564	7.811	9.544	13.558
Average Vertical Velocity $\bar{v}_{\|\|}$ (m/s)	0.097	0.171	0.300	0.409	0.576

Table 3.1: Physical environment parameters as a function of the Beaufort numbers.

$r = 1000$ m and, based on the assumptions outlined in Section 3.3, we consider a constant speed sound in the water (within the range of operation) equal to $c_{\text{s}} = 1500$ m/s.

The transmitter and receivers are assumed to operate in an ocean environment with the sea state parameters given in Table 3.1. We employ the Beaufort scale [54] to obtain the values of the average wind speed (measured at height of 10 m above sea surface) and the wave heights. The wind is assumed to be blowing with a constant speed U_{avg} over the fetch distance F, and the resulting waves have an average height of H_{avg}, and average wave period T_{avg}. Parameters $\sigma_{\text{h}}, \bar{v}_{\perp}, \sigma_{\perp}, \bar{v}_{||}$ are derived in Appendix B based on the JONSWAP spectrum.

Beaufort numbers shown in Table 3.1 characterize ocean environments that range from *calm* indicated by index 1, to *rough* indicated by 5. We are not considering higher Beaufort numbers since it is difficult to deploy transmitter and receivers in such ocean conditions. Note that both the wind speed and significant/average wave heights increase with Beaufort number. Throughout the Section 3.7 we assume that our transmitter and receivers are placed in an environment with Beaufort number equal to 3 (*slight*) which represents an intermediate sea state within the considered interval. The corresponding parameters $(\sigma_{\text{h}}, \bar{v}_{\perp}, \sigma_{\perp}, \bar{v}_{||})$ are used to find the correlation $|\gamma_{\text{G}}|$ for vertical and horizontal arrays with monochromatic and polychromatic sources. Sometimes, we will also consider behavior of the correlation function for the entire range of Beaufort numbers from 1 top 5.

Hereafter, it will prove convenient to introduce a retarded time expressed by $\tau = t - r/c_{\text{s}}$. The retarded time is always non-negative and $\tau = 0$ implies that the acoustic wave has just arrived at the receiver.

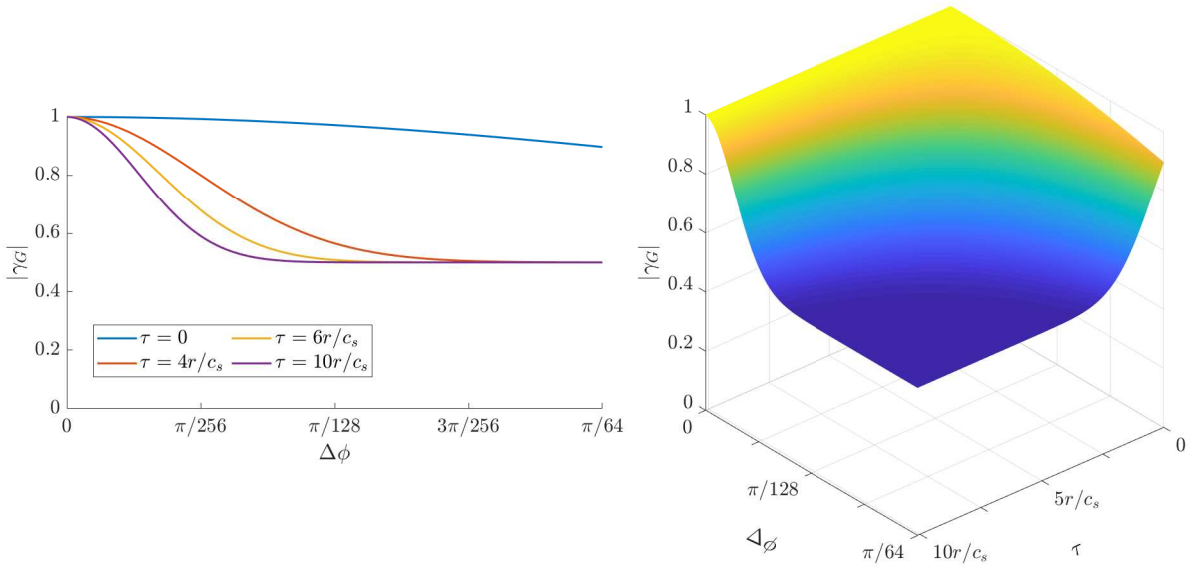

(b)

Figure 3.3: Correlation factor $|\gamma_{\rm G}|$ for horizontal array with monochromatic source of frequency $\nu_0 = 25$ kHz. Transmitter-receiver separation equals $r = 1000$ m.

3.7.1 Quasi-Monochromatic Source

Our focus is on studying the behavior of the correlation factor $|\gamma_{\rm G}|$ for vertical and horizontal receivers as a function of angular separation and the retarded time. As we will see this correlation dependence on space and time is inseparable.

Consider a horizontal array shown in Fig. 3.1 where $\theta_1 = \theta_2 = \frac{\pi}{2}$ or equivalently $\psi_1 = \psi_2 = 0$. The amplitude of the correlation factor $|\gamma_{\rm G}(\cdot)|$ (see (3.35)) reduces to

$$|\gamma_{\rm G}(\tau, \Delta\phi)| = \frac{1}{2}\left[1 + e^{-2\sigma_\perp^2 k_0^2 (\tau + r/c_{\rm s})^2 \sin^2(\Delta\phi/2)}\right], \tag{3.37}$$

with spatial dependence on angular separation $\Delta\phi$, group velocity factor $\sigma_\perp$, and retarded time τ. Fig. 3.3 depicts $|\gamma_{\rm G}(\tau, \Delta\phi)|$ for the case of two-element horizontal receiver array and a monochromatic transmitting source with carrier frequency $\nu_0 = 25$kHz and transmitter-receiver distance $r = 1000$ m.

Fig. 3.3 (a) depicts $|\gamma_{\rm G}|$ for several time instances τ as a function of the angular separation $\Delta\phi$. The surface plot Fig. 3.3 (b) demonstrates correlation dependence on both τ and $\Delta\phi$ and indicates correlation inseparability in space and time. Note that only for $\tau > 4r/c_{\rm s}$ or for $\Delta\phi \geq \pi/64$ the correlation $|\gamma_G|$ becomes virtually independent of the other spatial/temporal

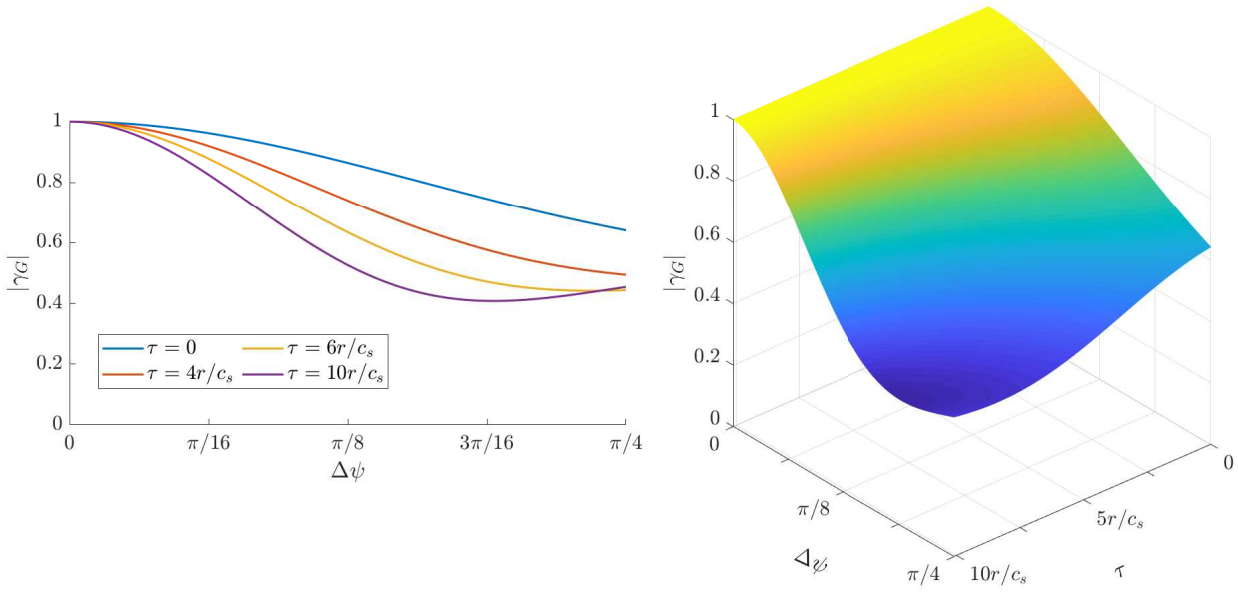

(b)

Figure 3.4: Correlation factor for the case of a vertical array and monochromatic source with $\nu_0 = 25$ kHz with transmitter-receiver distance $r = 1000\ m$.

component respectively.

Consider now a vertical array shown in Fig. 3.2, with $\phi_1 = \phi_2$. With the monochromatic source the correlation factor (3.35) reduces to

$$|\gamma_{\mathrm{G}}(\tau, \Delta\psi)| = \frac{1}{2}\left\{1 + J_0\left[k_0\left(\tau + r/c_s\right)\bar{v}_{||}\Delta\psi\right]e^{-2k_0^2\sigma_{\mathrm{h}}^2(\Delta\psi)^2}\right\}, \tag{3.38}$$

where $\Delta\psi$ is the angular separation, $\bar{v}_{||}$ the speed of the gravity wave pack, and σ_{h}^2 the variance of the wave heights. Fig. 3.4 (a) shows the correlation as a function of the angular difference $\Delta\psi$ for several time instances τ while Fig. 3.4 (b) shows how the correlation dependence on τ and $\Delta\psi$. The dependence of the correlation on time and space and its inseparability is even more pronounced for the vertical case.

Our next step is to compare the correlation factors $|\gamma_{\mathrm{G}}^{\mathrm{V}}|$ and $|\gamma_{\mathrm{G}}^{\mathrm{H}}|$ of the vertical and horizontal arrays respectively for ocean environments with with Beaufort numbers and parameters given in Table 3.1. We use $|\gamma_{\mathrm{G}}^{\mathrm{H}}|/|\gamma_{\mathrm{G}}^{\mathrm{V}}|$ ratio as a function of angular separation $\Delta\phi = \Delta\psi$ to decide under what conditions the vertical/horizontal array offers lower correlation for the case of $\tau = 0$. The latter case is the most interesting for communications, since we typically receive and sample information bearing signals as they arrive.

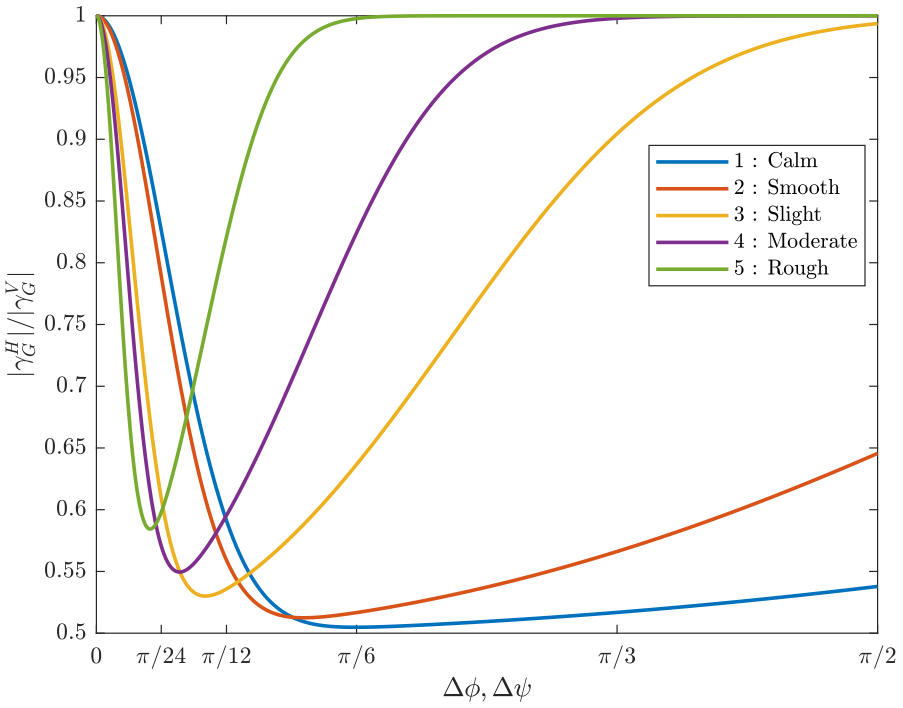

Figure 3.5: Ratio of the vertical and horizontal array correlation factors $|\gamma_{\mathrm{G}}^{\mathrm{H}}|$ and $|\gamma_{\mathrm{G}}^{\mathrm{V}}|$ for a monochromatic source with $\nu_0 = 25$ kHz and $r = 1000\ m$ taken at time $\tau = 0$.

The results are shown in Fig. 3.5 where different colors correspond to different sea states with Beaufort numbers from 1 to 5. For clam and smooth sea states, the correlation coefficient ratio decays sharply from 1 to almost 0.5 for angular separation $\Delta\psi = \Delta\phi > \frac{\pi}{12}$ before it starts to gradually increase again for $\Delta\psi = \Delta\phi > \frac{\pi}{8}$. Similar behavior is showcased for slight, moderate and rough sea states. However, for states 3–5, after the initial deep the correlation ratio approaches unity faster as the angular separation grows.

The results presented in Fig. 3.5 suggest that for the chosen parameter values, the horizontal array offers weaker correlations compared to the vertical array for a large interval of angular separation values. We comment on the factors influencing the relative magnitude of vertical and horizontal pressure correlations at the end of the section. By substituting $\tau = 0$ in (3.38) and (3.37), we obtain

$$
\begin{aligned}
|\gamma_{\mathrm{G}}^{\mathrm{H}}(\Delta\phi)| &= \frac{1}{2}\left[1 + e^{-2\sigma_\perp^2 k_0^2 (r/c_{\mathrm{s}})^2 \sin^2(\Delta\phi/2)}\right] \\
|\gamma_{\mathrm{G}}^{\mathrm{V}}(\Delta\psi)| &= \frac{1}{2}\left\{1 + J_0\left[k_0\left(\tau + r/c_{\mathrm{s}}\right)\bar{v}_{||}\Delta\psi\right] e^{-2k_0^2\sigma_{\mathrm{h}}^2(\Delta\psi)^2}\right\}.
\end{aligned}
$$

Both horizontal and vertical correlations are decaying functions with respect to $\sigma_\perp$, and

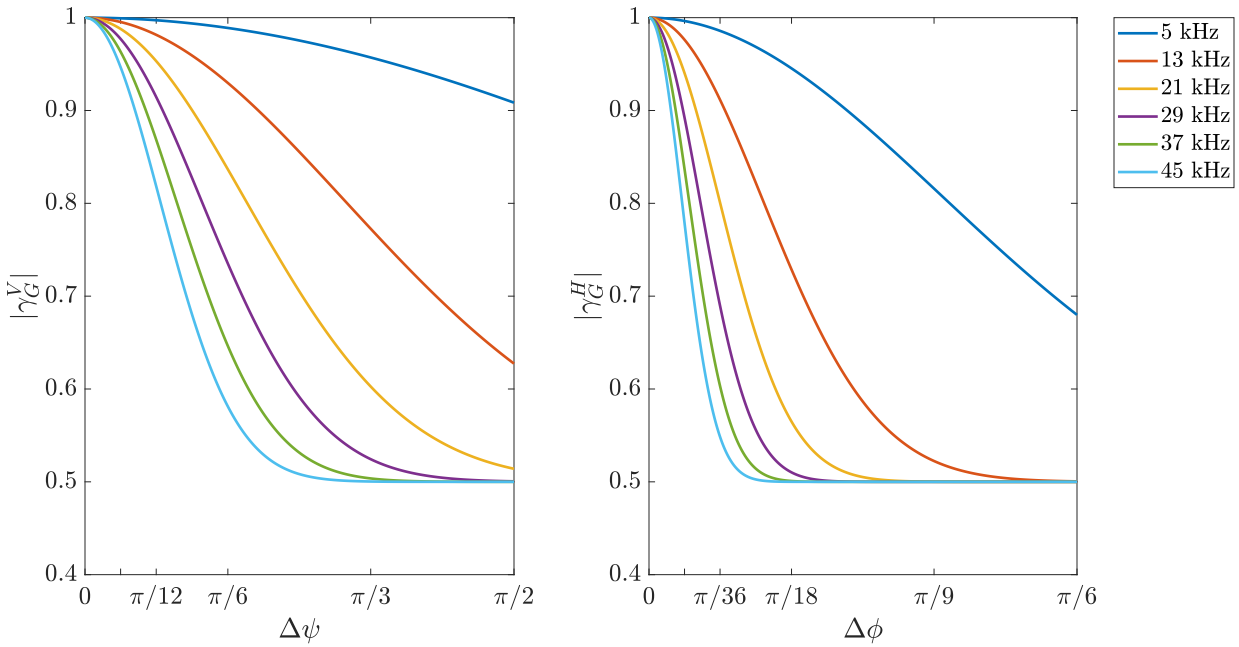

Figure 3.6: Vertical (left) and horizontal (right) array correlation factors $|\gamma_{\mathrm{G}}^{\mathrm{V}}|$ and $|\gamma_{\mathrm{G}}^{\mathrm{H}}|$ respectively as a function of the source frequency ν_0 for monochromatic source. Ocean environment with Beaufort number equal to 3 is considered.

$\sigma_{\mathrm{h}}, \bar{v}_{||}$ respectively. From Table 3.1 we can see that the parameter of the horizontal wave motion $\sigma_{\perp}$ is significantly larger than σ_{h} and $\bar{v}_{||}$ the characterize the vertical movement. This explains the sharp decay of $|\gamma_{\mathrm{G}}^{\mathrm{H}}|$ compared to $|\gamma_{\mathrm{G}}^{\mathrm{V}}|$ for the monochromatic source in consideration.

Finally, we study the behavior of $|\gamma_{\mathrm{G}}^{\mathrm{V}}|$ and $|\gamma_{\mathrm{G}}^{\mathrm{H}}|$ for the slight ocean environment (Beaufort number equal to 3) and $\tau = 0$, as a function of transmission frequency ν_0 of the monochromatic transmitter. Fig. 3.6 shows $|\gamma_{\mathrm{G}}^{\mathrm{H}}|$ and $|\gamma_{\mathrm{G}}^{\mathrm{V}}|$ for different ranges of $\Delta\phi$ and $\Delta\psi$ respectively. We clearly see that both vertical and horizontal arrays correlation factors imitate a spatial high-pass filter with respect to the angular separation $\Delta\phi$ or $\Delta\psi$.

3.7.2 Band-Limited Source with Raised Cosine Pulse as Spectral Amplitude Function

In this section we study a polychromatic source particularly important to underwater communication systems. The source emits a raised-cosine (RC) pulse, operates at the central frequency ν_0, and uses bandwidth B or, equivalently, pulse duration $T = 1/B$. The RC

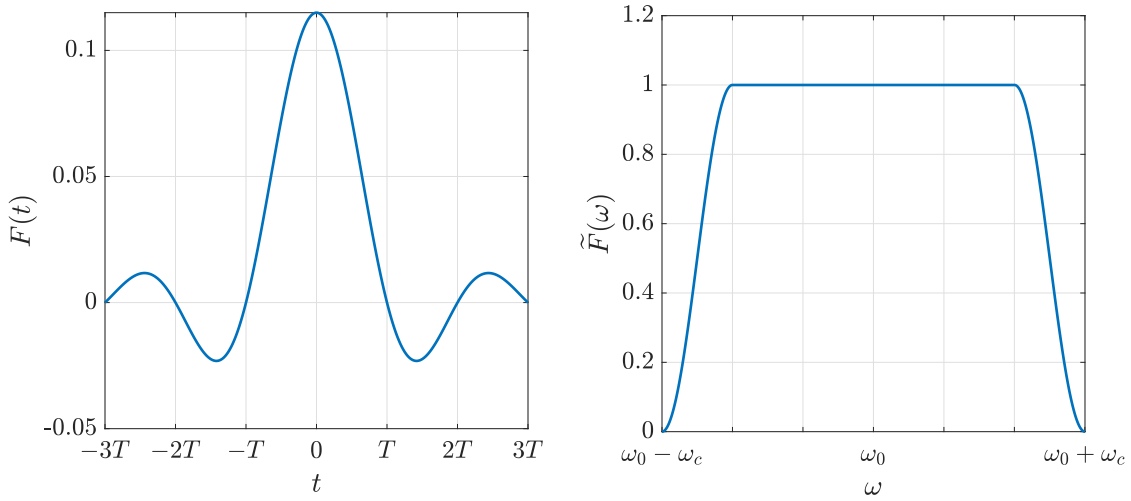

Figure 3.7: Temporal profile $F(t)$ (left) and frequency response $\tilde{F}(\omega)$ (right) for an RC pulse of duration T and central frequency $\omega_0 = 2\pi\nu_0$.

pulse temporal and spectral profiles $F(t)$ and $\tilde{F}(\omega)$ are shown in Fig. 3.7. We consider a carrier frequency (central frequency) $\nu_0 = 25$ kHz and bandwidth $B = 8$ kHz. Note that the temporal profile $F(t) = 0$ at $t = T, 2T, \ldots$ and $F(t = 0) = 1$. This property of RC pulses allows to avoid inter-symbol interference (Nyquist condition) in case the receiver samples a sequence of transmitted pulses at times $\tau = 0, T, 2T, \cdots$ etc. In our experiment we are transmitting a single pulse since we are focused on correlation properties rather than on data transmission directly.

Fig. 3.8 depicts the correlation coefficient $|\gamma_{\mathrm{G}}|$ for the horizontal array as a function of $\Delta\phi$ and τ. Fig. 3.8 (a) shows the correlation dependence on spatial parameter $\Delta\phi$ for several time instants τ. For higher values of τ the correlation decays quickly as a function of $\Delta\phi$ while for $\tau = 0$ its decay with $\Delta\phi$ is very slow. Fig. 3.8 (b) confirms the inseparable dependence of the correlation on time and space. We also note that for higher values of $\Delta\phi$ the correlation inherits the temporal behaviour of the source (see Fig. 3.7) as it reaches its maximum at $\tau = 0$ and 0 for $\tau = T, 2T, \cdots$. This happens due to the dominance of the direct propagation path that carries the properties of the transmitted pulse itself. The dips at $\tau = T, 2T, \cdots$ will not occur when a sequence of such data-carrying pulses is transmitted since for each $\tau = T, 2T, \cdots$ there will be a pulse which is sampled at its peak value.

The behavior of the correlation with respect to τ and $\Delta\psi$ for the case of vertical array is very similar. As in the horizontal array case, the correlation behaviour mimics the RC temporal profile and reaches its maximum value for $\tau = 0$. It reaches 0 for τ equal to

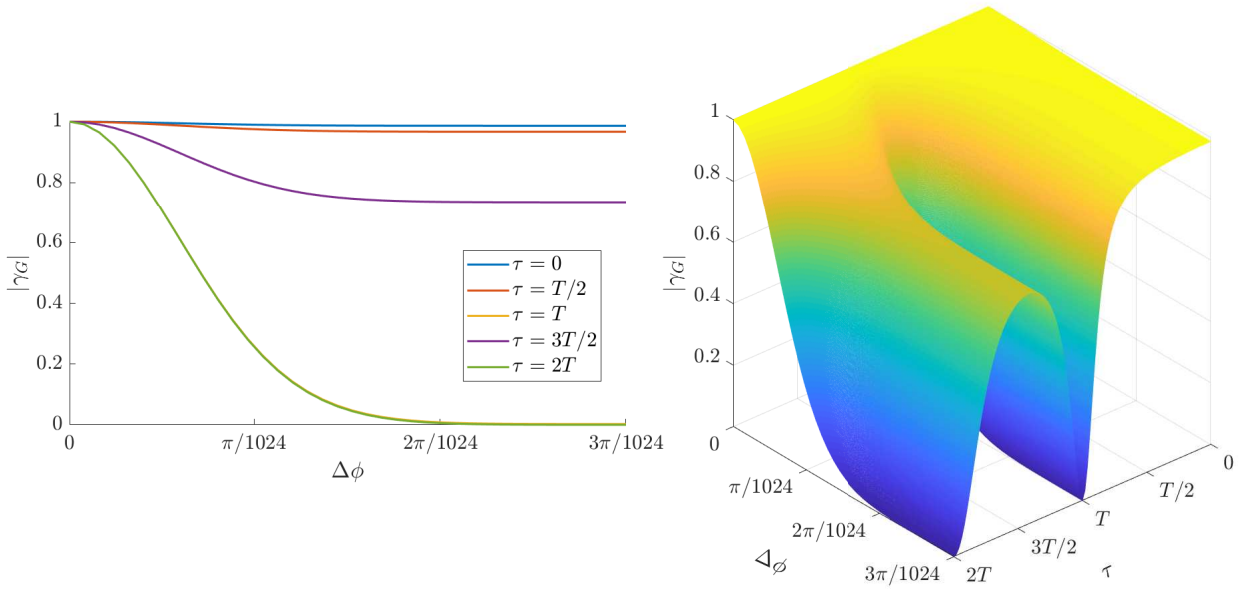

(b)

Figure 3.8: Correlation factor $|\gamma_G(\tau, \Delta\phi)|$ for the horizontal array setting when a band-limited RC source with $\nu_o = 25$ kHz and $B = 8$ kHz is utilized; Beaufort number equals 3.

multiples of T. The decay of the correlation with respect to $\Delta\psi$ for higher values of τ is slightly slower than for the horizontal case.

A comparison between the vertical (left) and horizontal (right) array correlations for range of transmission bandwidths B is given in Fig. 3.9. The results demonstrate that the correlation factors increase as the bandwidth of the pulse grows. This is opposite to the behavior of the correlation with respect to the central frequency ν_0. Fig. 3.6 computed for the case of a monochromatic source shows that the correlation decreases as a function of the source frequency ν_0.

Fig. 3.9 also demonstrates that the horizontal array offers lower correlation compared to the vertical array because of the fact that group velocity parameter $\sigma_\perp$ is much larger than wave vertical movement σ_{h} and $\bar{v}_{||}$. As we can infer from Appendix B, the Fetch distance is a significant factor that influences $\sigma_\perp$: a shorter fetch distance could result in a smaller $\sigma_\perp$ potentially reversing the observed trend.

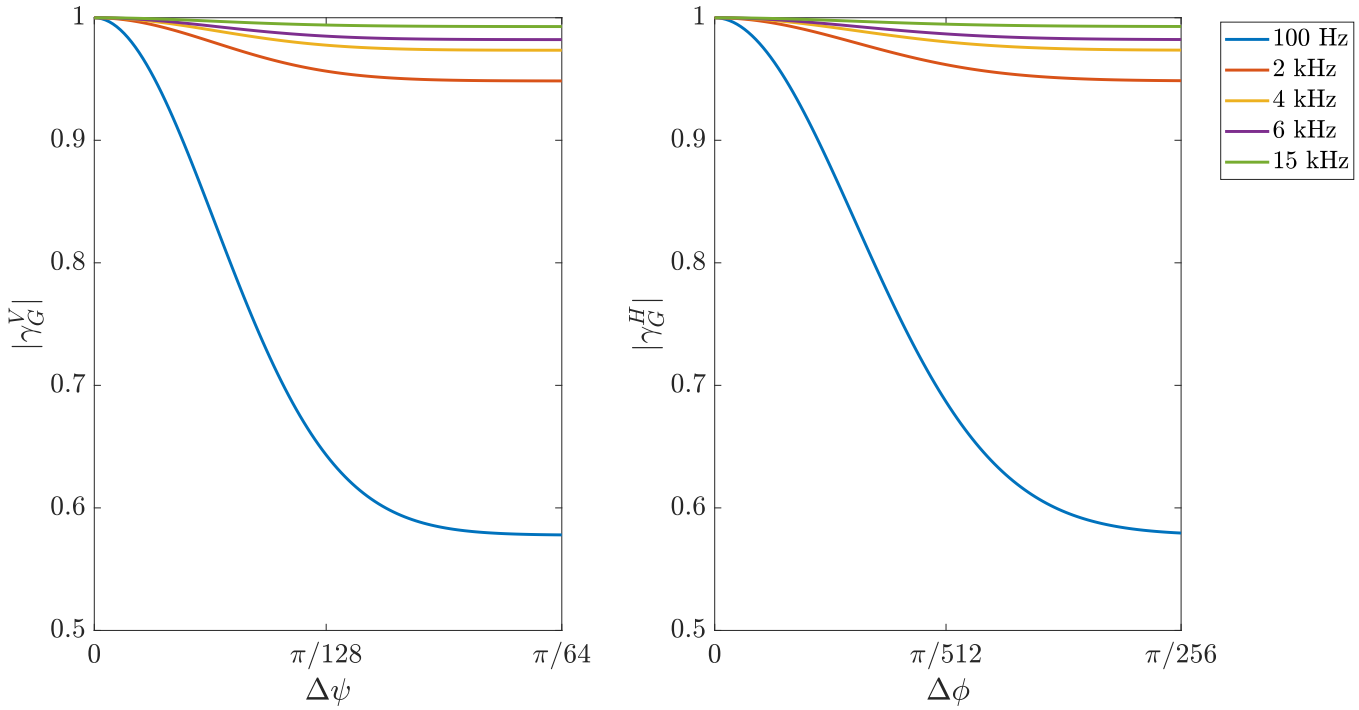

Figure 3.9: Vertical (left) and horizontal (right) correlation coefficients, plotted as functions of $\Delta\psi$ and $\Delta\phi$ respectively for band-limited RC source with carrier frequency $\nu_0 = 25$ kHz and for $\tau = 0$. Ocean environment with Beaufort number 3 is considered.

3.7.3 Correlation Dependence on the Beaufort Number

Based on (3.19) we can compute the normalized correlation factors for the direct and indirect (surface reflection) paths separately to study their contributions to the overall correlation coefficient. The direct and indirect correlations are given by

$$\gamma_{\mathrm{G}}^{\mathrm{direct}} = \frac{\frac{|F(\tau)|^2}{r^2}}{\sqrt{\Gamma_{\mathrm{tot}}(\boldsymbol{r}_1;t_1)\Gamma_{\mathrm{tot}}(\boldsymbol{r}_2;t_2)}}, \tag{3.39}$$

$$\gamma_{\mathrm{G}}^{\mathrm{indirect}} = \frac{\Gamma(\boldsymbol{r},t)}{\sqrt{\Gamma_{\mathrm{tot}}(\boldsymbol{r}_1;t_1)\Gamma_{\mathrm{tot}}(\boldsymbol{r}_2;t_2)}}. \tag{3.40}$$

Fig. 3.10 demonstrates the correlation factors for the vertical (left) and horizontal (right) array receivers in an ocean environment with Beaufort number equal to three. The receiving arrays are located at distance of 1000 meters from the transmitter.

From (3.32) and (3.30) we can see that the direct path contribution to the correlation is dominant compared to the indirect path. The indirect path component (integrand in (3.32)) is smaller that the direct path component (integrand in (3.30)). As the angular

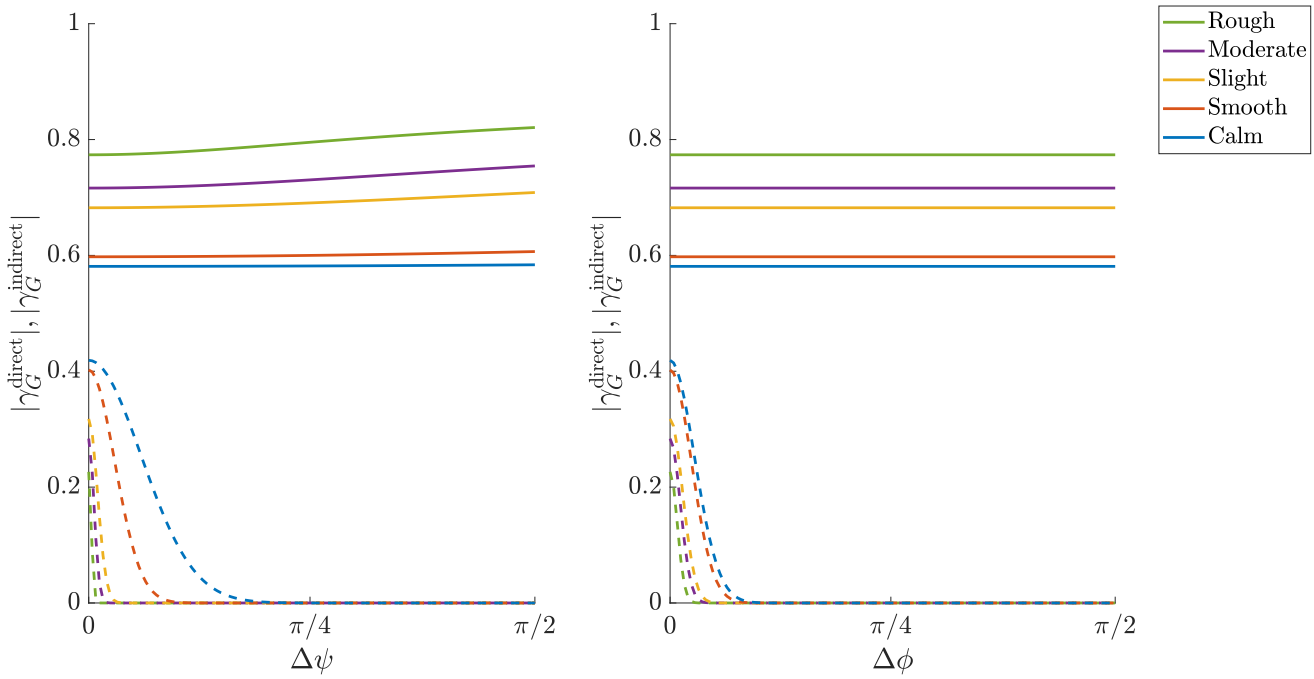

Figure 3.10: Correlation factors $|\gamma_G^{\text{direct}}|$ (solid lines) and $|\gamma_G^{\text{indirect}}|$ (dashed lines) for vertical (left) and horizontal (right) array located at distance of 1000 m from the transmitter, for $\tau = 0$.

separation $\Delta\psi$ or $\Delta\phi$ increases this dominance becomes even more pronounced. The indirect contribution decays with $\Delta\psi$ and $\Delta\phi$ for both vertical and horizontal array case but the rate of the decay depends on the Beaufort number. The higher the Beaufort number the faster is the decay since the parameters $\sigma_{\text{h}}, \bar{v}_{||}$ and $\sigma_{\perp}$ take higher values. For both array types the direct path contribution is insensitive to angular separation $\Delta\psi$ or $\Delta\phi$ between the array elements (it changes slightly due to overall normalization).

The results of Fig. 3.10 and 3.9 confirm that in the communication scenario we consider we can expect strongly correlated links between transmitters and receivers in an underwater MIMO acoustic communication system. This can negatively affect the rank of the MIMO channel as well as its capacity [55]. In an extreme case when the correlations are close to unity the channel degrades into a *keyhole* channel in which any transmitter-receiver link experiences exactly same channel coefficient. The rank of such channel matrix degrades to unity as well and its capacity scales logarithmically with the number of transmit/receive elements.

In other potential scenarios where such direct link is absent, quick degradation of correlations resulting from surface fluctuations would lead to uncorrelated MIMO channels with high rank and capacity. The absence of a direct link would obviously result in diminished signal-to-noise ratio at the receiver. Therefore, in order to exploit the potential of such MIMO links much higher transmit power levels would have to be utilized.

3.8 Discussion and Conclusions

In this chapter we advance a theoretical framework to determine space-time correlations of pressure waves generated by a polychromatic acoustic point source underwater. We derive a general expression for two-point space-time pressure field correlation function and demonstrate the inseparability of the correlation function in space and time. The correlation functions for two sources (a monochromatic source and a polychromatic source transmitting raised-cosine pulses) have been studied in detail along with two types of receiver arrays: vertical and horizontal. The derived expression quantifies the surface-induced correlation component that vanishes as a function of the angular separation between the receiver elements as well as Beaufort number that dictates the surface variation. This effect would give a promise to a high-rank and capacity MIMO communications channel. However, the dominance of the direct component which is insensitive to angular separation and Beaufort number leads to high overall correlation and hinders MIMO communications. Therefore, beam-forming with multiple transmit and receive elements and their utilization to increase the signal-to-noise ratio via signal combining is, in general, more practical under water compared to signalling techniques tailored for high-rank MIMO channel that can be encountered in terrestrial wireless applications.

It is instructive to compare our approach to the related work by Dahl, [48] that treated the same subject. There are several key differences between the two approaches. First, Dahl considers the case of rather large surface wave swells, such that the surface slopes are large and should be treated within the Kirchhoff approximation in the single-scattering regime. We, on the other hand, focus on the case of fairly smooth surfaces such that the surface can be viewed as quasi-flat (small local curvature) with random parameters determined by the surface wave motion. Second, Dahl's statistical model is oversimplified: the surface wave influence enters only through a single parameter, the root mean-square slope of the wave, and hence the model is capable of describing pressure correlations in the horizontal plane only. In

contrast, we take into account in-plane (horizontal) as well as vertical motion of the surface waves and their effect on Doppler shifts of the scattered acoustic waves. Therefore, we are able to quantitatively describe in-plane as well as vertical pressure correlations. Third, Dahl's approach is limited to strictly monochromatic sources, as no temporal pressure fluctuations are taken into account, while we consider a general polychromatic source. Most importantly, Dahl's approach is semi-phenomenological in nature, combing ray tracing with a simplified version of Kirchhoff's approximation for scattering of a single plane wave (ray). By contrast in the present manuscript, we offer a first-principles approach rooted in the wave equation and revealing the crucial role the space-time coupling plays in entangling vertical and in-plane pressure correlations as well as providing accurate dependence of the said correlations on the frequency of any monochromatic component within the source spectrum. Interestingly, Dahl's phenomenological exponential correlation function does qualitatively captures the in-plane pressure correlations in the quasi-monochromatic case, although their dependence on the surface wave parameters is quite a bit more complicated as we discover in the present work.

Further, we point out that our model assumes clear water, thereby neglecting any volume scatterers as well as surface bubble plumes that can form by the ocean surface for large enough surface gravity waves. Any volume scatterers, be they internal waves, turbulent fluctuations as well as macro- or microorganisms, such as fish or copepods, will degrade correlations among the plane waves propagating directly to the receivers as well as among those scattered from the ocean surface, thereby weakening pressure correlations at the receiver arrays. As far as communication applications of our theory are concerned, such additional subtle effects that we have neglected at this stage, will only boost the underwater MIMO prospects.

Air bubbles will in general attenuate the waves transmitted through bubble plumes near the surface. In addition, the monochromatic components of the acoustic waves at the frequencies in resonance with the internal oscillation frequencies of the bubbles of all sizes present by the surface will suffer spectacular attenuation by virtue of transferring their acoustic energy to bubble oscillations. Therefore, these monochromatic components will be virtually absent from the spectrum of the waves captured by the receivers. As a result, the correlations will have a more pronounced dependence on the spectral content of the source.

Appendix A: Raised Cosine Filter Spectral Amplitude Function

The polychromatic raised-cosine source has the following spatial spectral amplitude function [56]

$$\widetilde{F}(\omega) = \begin{cases} 1, & \omega_0 - \frac{(1-\beta)\pi}{T} < \omega \leq \omega_0 + \frac{(1-\beta)\pi}{T} \\ \frac{1}{2}\left[1 + \cos\left(\frac{T}{2\beta}\left[|\omega - \omega_0| - \frac{(1-\beta)\pi}{T}\right]\right)\right], & \omega_0 + \frac{(1-\beta)\pi}{T} < \omega \leq \omega_0 + \frac{(1+\beta)\pi}{T} \\ \frac{1}{2}\left[1 + \cos\left(\frac{T}{2\beta}\left[|\omega - \omega_0| - \frac{(1-\beta)\pi}{T}\right]\right)\right], & \omega_0 - \frac{(1+\beta)\pi}{T} \leq \omega < \omega_0 - \frac{(1-\beta)\pi}{T} \\ 0, & \text{otherwise} \end{cases} \tag{3.41}$$

The source temporal profile shown in Fig. 3.7 is given by

$$F(t) = \frac{1}{T}\text{sinc}\left(\frac{t}{T}\right)\frac{\cos(\frac{\pi\beta t}{T})}{1 - (\frac{2\beta t}{T})^2}e^{-i\omega_0 t}, \tag{3.42}$$

where

$$\text{sinc}(x) = \frac{\sin(\pi x)}{\pi x}.$$

Appendix B : Calculation of Significant Wave Height H_{s}, T_{avg}, σ_{h}, $\bar{v}_{||}$, $\bar{v}_{\perp}$, $\sigma_{\perp}$ using JONSWAP distribution

From Beaufort scale, we read the wind speed U_{10} and the corresponding probable wave height H_{avg}. Note that H_{s} is defined as the mean of the recorded trough to crest heights H_{r} of the highest third of the waves. The wave height h that we employ is assumed to be Gaussian with mean $\mu = 0$. We now attempt to find H_{s} and the variance σ_{h}^2, using H_{avg} and the fact that H_{r} (recorded heights) follow the folded normal distribution where $H_{\text{r}} \approx 2|h|$ (assuming the waves are symmetric).

The average wave height is then given by

$$H_{\text{avg}} = 2\sigma_{\text{h}}\sqrt{\frac{2}{\pi}}\ , \tag{3.43}$$

and, equivalently,

$$\sigma_{\text{h}} = H_{\text{avg}}\sqrt{\frac{\pi}{8}}\ . \tag{3.44}$$

The significant height of H_{r} is given by (see Appendix C)

$$H_{\mathrm{s}} = 6\sqrt{\frac{2}{\pi e}}\sigma_{\mathrm{h}} \ .$$

Using the wind speed U_{10}, JONSWAP angular frequency ω_{p} [57] is given by

$$\omega_{\mathrm{p}} = 22\left(\frac{g^2}{U_{10}F \times 10^3}\right)^{\frac{1}{3}} \ . \tag{3.45}$$

The fetch distance F is the distance over which the wind blows with constant velocity. We find the value of F that matches the sea-state indices to the Beaufort wind scale indices, using the following relationship between fetch, significant height and wind speed for practical JONSWAP data [52]

$$F = \left(\frac{H_{\mathrm{s}}}{0.0163 \times U_{10}}\right)^2 , \tag{3.46}$$

see Table 3.1. The average angular frequency is approximated to the probable angular frequency ω_{p}

$$\omega_{\mathrm{avg}} \ = \ \omega_{\mathrm{p}},$$

and the corresponding average period

$$T_{\mathrm{avg}} \ = \ \frac{2\pi}{\omega_{\mathrm{avg}}}. \tag{3.47}$$

Using average wave heights H_{avg} (3.43) and average periods T_{avg} (3.47), we calculate average vertical velocity $\bar{v}_{||}$

$$\bar{v}_{||} = \frac{\pi H_{\mathrm{avg}}}{T_{\mathrm{avg}}} \tag{3.48}$$

The average group velocity $v_{\perp}$ is computed using the average wave period T_{avg} with $g = 9.8$ m/s^2 and

$$\bar{v}_{\perp} = \frac{gT_{\mathrm{avg}}}{2\pi} \ . \tag{3.49}$$

Finally, the group velocity parameter $\sigma_{\perp}$ is given by

$$\sigma_{\perp} = \frac{\bar{v}_{\perp}}{\sqrt{\pi/2}} \ . \tag{3.50}$$

Appendix C: Significant Height H_s for half-Normal distribution

Starting with $h \approx \mathcal{N}(0, \sigma_{\mathrm{h}}^2)$ we have

$$x = |h| \ , \tag{3.51}$$

where x is the wave height from sea level to crest. The probability distribution of x is a modified normal distribution with PDF

$$P_X(x) = \sqrt{\frac{2}{\pi\sigma_{\mathrm{h}}^2}} e^{-\frac{x^2}{2\sigma_{\mathrm{h}}^2}} \ . \tag{3.52}$$

The half-normal distribution of x implies

$$\int_{\sigma_{\mathrm{h}}}^{\infty} P_X(x)\delta x \ = \ \frac{1}{3}, \tag{3.53}$$

and $[\sigma_{\mathrm{h}}, \infty]$ is the range of the third highest wave heights. The conditional distribution of the wave heights over the mentioned range is given by

$$\begin{aligned} P_{X\in[\sigma_{\mathrm{h}},\infty]}(x) \ &= \ \frac{P_X(x)}{P[X \in [\sigma_{\mathrm{h}}, \infty]]} \\ &= \ 3\sqrt{\frac{2}{\pi\sigma_{\mathrm{h}}^2}} e^{-\frac{x^2}{2\sigma_{\mathrm{h}}^2}} \end{aligned} \tag{3.54}$$

The significant height of x is then given by

$$\begin{aligned} \bar{H}_s \ &= \ \int_{\sigma_{\mathrm{h}}}^{\infty} x P_{X\in[\sigma_{\mathrm{h}},\infty]}(x)\delta x \\ &= \ 3\sqrt{\frac{2}{\sigma_{\mathrm{h}}^2\pi}} \int_{\sigma_{\mathrm{h}}}^{\infty} x e^{-\frac{x^2}{2\sigma_{\mathrm{h}}^2}} \delta x \\ &= \ 3\sqrt{\frac{2}{\sigma_{\mathrm{h}}^2\pi}} (-\sigma_{\mathrm{h}}^2) e^{-\frac{x^2}{2\sigma_{\mathrm{h}}^2}} \Big|_{\sigma_{\mathrm{h}}}^{\infty} \\ &= \ 3\sqrt{\frac{2}{\pi e}} \sigma_{\mathrm{h}} \ . \end{aligned} \tag{3.55}$$

For $y = |2h|$, we have the following PDF

$$\begin{aligned} P_Y(y) &= \frac{1}{\sqrt{2\pi\sigma_{\mathrm{h}}^2}} e^{-\frac{y^2}{8\sigma_{\mathrm{h}}^2}} \\ \int_{2\sigma_{\mathrm{h}}}^{\infty} \frac{1}{\sqrt{2\pi\sigma_{\mathrm{h}}^2}} e^{-\frac{y^2}{8\sigma_{\mathrm{h}}^2}} &= \frac{1}{3}, \end{aligned} \tag{3.56}$$

where $[2\sigma_{\mathrm{h}}, \infty]$ is the range of the highest third of the wave heights. The significant height of y is then

$$\begin{aligned} H_s &= 6\sqrt{\frac{2}{\pi}}\sigma_{\mathrm{h}} e^{-\frac{1}{2}} \\ &= 6\sqrt{\frac{2}{\pi e}}\sigma_{\mathrm{h}} \ . \end{aligned} \tag{3.57}$$

Chapter 4

Joint Iterative Interference Cancellation and Channel Estimation for Underwater OFDM

4.1 Introduction

Underwater communication enabled numerous applications ranging from wireless submarine to submarine communication in military, to domestic underwater and marine environment monitoring using autonomous underwater vehicles (AUVs) [58]. In many of these applications, the data generated from sensors and AUVs is increasingly large, and commands the need for communication system that teams well with the mobility aspect of underwater assets. Wireless communication systems present themselves as a solution with either light signal [59] for short distances data exchange, or sound for relatively longer transmission reach. In both cases, the developed systems follows one (or more) of the well known fixed allocation schemes : Time Division Multiple Access (TDMA); Frequency Division Multiple Access (FDMA) and Code Division Multiple Access (CDMA). With sound waves as media of transmission, TDMA implementation is challenging because of strong synchronization requirement, especially in network settings. Moreover, large delays and strong multi-path presence prevents scalability of point to point to the eventual network settings [60] faced in many applications. The mentioned tremendous challenges faced in implementing underwater sound-based TDMA motivated research and development of frequency or code based underwater communication schemes.

Direct Spread − Code Division Multiple Access (DS − CDMA) transmitter/receiver design is advocated in [61]. Spatial diversity weights combiners, forward and backward filters are jointly optimized and updated at the symbol rate for slow time varying channels. As channel variability increases it becomes imperative to update the channel at the chip level to maintain the same performance, at additional cost of computation complexity. Similar approach is presented in [62] where a filter with tasks of equalization, and multi-access interference cancellation is updated every symbol, and deteriorates in performance as the

channel variability increases. In [63], channel variability is found to be the limiting factor to CDMA systems, the chip rate processing complexity increases significantly to maintain the benchmark performance of static channel.

Orthogonal Frequency Division Multiplexing (OFDM) has been advocated for underwater communication [64], since OFDM is not only computationally efficient because of the use of the Fast Fourier Transforms, but allows as well for efficient utilization of bandwidth and enables high data rates. OFDM is chosen as a modulation scheme for many of the wireless communication standards (including the 4G LTE). OFDM is typically utilized in frequency-selective channels and known for its sensitivity to time selectivity since it results in carriers orthogonality loss. The obstacle of time selectivity however did not hinder the adoption for OFDM for doubly selective channels arise in communication with rapidly moving objects such high speed trains [65] [66].

In underwater acoustic communications, because of the use of sound (with bandwidth comparable to the carrier frequency), Doppler spread is much more pronounced then in terrestrial Electromagnetic (EM). Underwater channels have long impulse responses caused by slow propagation sound waves and numerous surface and bottom reflections. The combined effect of multi-path channel impulse response and fast channel variability results in a Doubly selective channel with both frequency selectivity and inter-carrier interference.

Several methods presented in literature to tackle the double selectivity nature. In [67] [68] an oversampling approach is applied to unpack the observed frequency-domain signal. Each sub-carrier received signal is decomposed into finer sub-carriers using oversampling, and apply weight vectors to cancel the interference. The weights are updated such that the resultant system is ICI-free. Similar approach is applied in [69] [70] where oversampling results in a Doppler-frequency channel representation and the transmitted symbols are collected from both dimensions, and ICI is exploited as source of observations. An estimation of interference coefficients (off-diagonal elements) and mitigation approach is shown in [11] where the estimation of the off diagonal elements is implemented using the Least Mean Square (LMS) algorithm, and cancelled using decision feedback filter effectively treating ICI as Inter symbol (ISI) interference in frequency domain. Feed-forward, phase-correction unit, and feed-backward filter coefficients are optimized in the MSE sense.

System parameters optimization to minimize ICI approach is found in [71] where the

both the transmitter and receiver pulses are optimized, for non coherent soft symbol detectors that uses only Doppler-delay profile as a prior for data detection. A data and pilot allocation strategy in OFDM frame is presented in [72] to effectively treat residual Doppler shift induced ICI - assuming ICI is limited to window of neighbouring sub-carriers. Orthogonal Matching Pursuit (OMP) algorithm is applied in [72] to explore the channel sparsity structure, a feature in many communication channels, including underwater. In [73] a comparison is conducted between the ICI-ignorant, the Bases Expansion Model (BEM) based, and the discrete-delay channel receivers, respectively in their treatment of ICI. The study concludes that the best performance of presented receivers is under slow varying channels, and deteriorates as channel variability increases. The best performance is for discrete channel impulse response based receivers where BEM deteriorates even worse than ICI ignorant. Coherent OFDM systems require channel knowledge for equalization, and in many cases channel instances estimation is implemented to acquire this channel knowledge, either using pilot signals or data-aided channel estimation. Many systems couple channel estimation and data detection through information exchange to improve the performance of both units to reduce low Bit Error Rate (BER) further. In [74] [75], a spares channel estimator, carrier frequency offset estimator and Low Density Parity Check (LDPC) decoder coupled to exchange both soft and hard symbols generated by the decoder to the estimator to produce a refined channel estimate. Similarly, in [76] a turbo equalizer is coupled with LMMSE channel estimator. In [77] a CDMA based system, that employs Cyclic coordinate descent (CCD) strategy where the detector cycles through symbol estimates, channel estimates, and carrier phase estimates, adjusting each one in turn while holding the other two constant. OFDM system with LDPC decoder and ICI estimation and canceller that extends its span (number of off-diagonal) in case of decoding failure is presented in [78] and for MIMO-OFDM in [79] with BEM channel estimation. In [80], a turbo equalization with Recursive Least Square (RLS) is used to estimate a time in-variant channel with ICI caused by frequency offset. Turbo equalization with sparse estimation algorithm is presented in [81] for MIMO-OFDM system, and for Single Carrier (SC)-MIMO in [82]. Note for all of these system, the decoder exhibits high computational complexity of the whole system since it is part of the interference cancellation loop. In this chapter, we present a simple iterative interference cancellation receiver that utilizes a simple repetition−permeation code [83], coupled with data-aided channel estimation, to reach interference free performance with low complexity.

After reviewing OFDM transmitted/received signal format, pilot signal format, underwater synthetic channel generation, we present the iterative interference cancellation receiver and its detailed operation with perfect channel knowledge. Then we study the problem for doubly selective channel estimation and propose pilot only Forward-backward Kalman Filter as a solution, and study its data aided version. The channel estimator integration process with the interference cancellation receiver is then presented, where we show the benefit of interaction between the two units.

4.2 OFDM Transmitted and Received Signalling Format

In this section, we present the encoding and modulation process to construct the transmitted signal. As well, the pilot signal and its correlation properties useful for synchronization and start of frame detection. For ease of reference, we review the synthetic channel generation process detailed in chapter.

4.2.1 OFDM Transmitted Frame

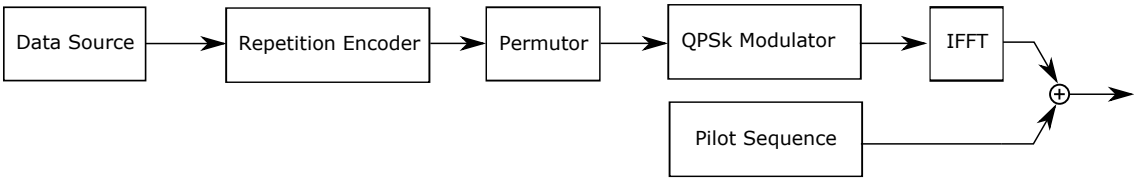

Figure 4.1: shows transmitter units and steps to convert information bits frame $\boldsymbol{B}[\boldsymbol{l}]$ to transmitted signal $\boldsymbol{x}$.

We consider an OFDM transmitter setup depicted in Fig. 4.1. The data source generates 512 data bits frame $\boldsymbol{B}[l]$ where l indicates frame index. The frame $\boldsymbol{B}[l]$ is input to repetition unit with reparation factor $M = 4$. The output block $\boldsymbol{B}^{\text{rep}}[l]$ (2048 bits) is permuted (with permutation matrix $\mathbf{P}$) to spread bits over the frame. The output of the permutor $\boldsymbol{B}^{\text{perm}}[l]$ is mapped to Quadrature Phase Shift Keying (QPSK) symbols vector $\boldsymbol{D}$ with $N = 1024$ sub-carriers. Using Inverse Fourier Transform (IFFT), $\boldsymbol{D}$ is converted to time domain data signal $\boldsymbol{d}$. The frequency domain pilot signal $\boldsymbol{P}$ is an FFT of repeated Zadoff-Chu sequence with correlation properties showed in Figure (4.4a). The time domain pilot signal $\boldsymbol{p}$ is added

to $\boldsymbol{d}$ to produce the signal $\boldsymbol{x}$,

$$\boldsymbol{x} = \boldsymbol{p} + \boldsymbol{d}, \tag{4.1}$$

which has corresponding frequency domain representation,

$$\boldsymbol{X} = \boldsymbol{P} + \boldsymbol{D}. \tag{4.2}$$

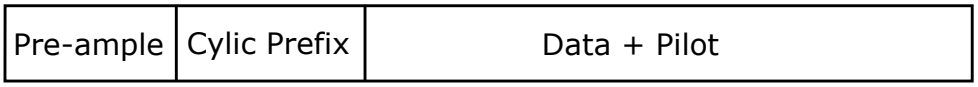

Figure 4.2: OFDM frame structure

Figure 4.2 depicts a block of transmitted frame contains the data−pilot block $\boldsymbol{x}$, cyclic prefix $\boldsymbol{x}_{\mathrm{CP}}$ and preamble $\boldsymbol{p}_{\mathrm{Pre}}$. The preamble $\boldsymbol{p}_{\mathrm{Pre}}$ (with length N_{Pre}) is repeated pilot structure utilized by the receiver to estimate the power-delay profile and frame synchronization. Removal of cyclic prefix block $\boldsymbol{x}_{\mathrm{CP}}$ (length N_{CP}) mitigates Inter symbol-Interference and insure sub-carriers orthogonality in case of frequency-selective only channels. The transmitted frame $\boldsymbol{x}_{\mathrm{t}}$ is given by

$$\boldsymbol{x}_{\mathrm{t}} = \begin{bmatrix} \boldsymbol{p}_{\mathrm{Pre}} \\ \boldsymbol{x}_{\mathrm{CP}} \\ \boldsymbol{x} \end{bmatrix}, \tag{4.3}$$

with length $N_{\mathrm{t}} = N_{\mathrm{Pre}} + N_{\mathrm{CP}} + N$.

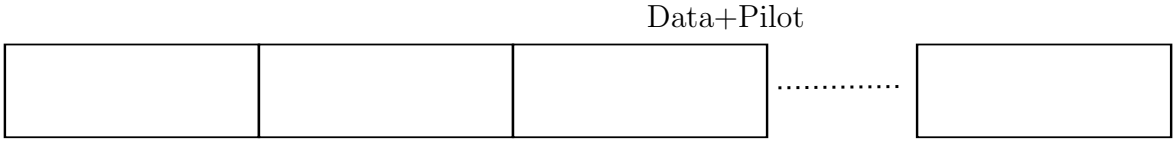

Figure 4.3: Transmission Protocol

Figure (4.3) shows the transmission protocol for multiple data blocks. All blocks have length N_{t} including the silence period. The transmission starts with a pilot-only block, that serves start-of-frame detection, Doppler shift compensation, and Auto-regressive (AR) channel model parameter setting. The silence period can be utilized in synchronization as well.

4.2.2 Pilot Signal

Both the pilot-only and the preamble blocks employ the pilot signal shown in Figure 4.4. The time domain pilot signal is a Zadoff–Chu sequence of the form

$$\boldsymbol{p}_{\text{base}} = \frac{1}{\sqrt{N_{\text{ZC}}}} \mathcal{F}^{-1}\{\exp(-2\pi i \boldsymbol{q})\} \tag{4.4}$$

where N_{P} is length of sequence, $\mathcal{F}^{-1}$ is the inverse Fourier Transform operator and $\boldsymbol{q}$ is a vector with length N_{P} with elements randomly selected from the 8-PSK constellation. By repeating the base signal in Figure 4.4 $\frac{N_{\text{total}}}{N_{\text{NC}}}$ times the repeated pilot signal is built. Figure (4.4a) shows the correlation function of the repeated pilot signal $\boldsymbol{p}$. The correlation function of the signal $\boldsymbol{p}$ is shown in (4.4b).

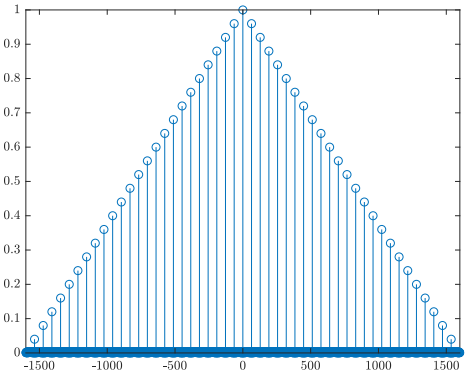

(a) Correlation function of repeated pilot signal $\boldsymbol{p}$

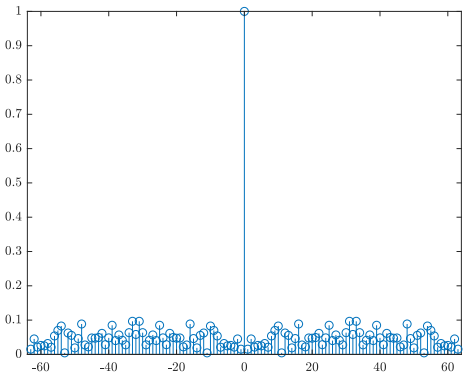

(b) Correlation function of pilot signal $\boldsymbol{p}_{\text{base}}$

4.2.3 OFDM Received Frame

Following the Inter-symbol-interference (ISI) channel representation, the time domain received signal $y[i]$ is given by

$$y[i] = \sum_{k=0}^{L-1} f_k[i] x_{\text{t}}[i-k] + n_i, \tag{4.5}$$

where L is the number of discrete channel taps and $f_k[i]$ is the k^{th} tap in the channel impulse response $\boldsymbol{f}[i]$ at time instance i. The discrete channel taps takes into account both transmit and receiver filters effects. The time domain received frame in matrix format is given by

$$\boldsymbol{y}_{\text{r}} = \mathbf{H}_{\text{w}} \boldsymbol{x}_{\text{t}} + \boldsymbol{n}. \tag{4.6}$$

where $\mathbf{H}_{\mathrm{w}}$ is convolution matrix of underwater channel impulse responses. An elaborate form of (4.6) in terms of preamble and cyclic prefix transmitted signals is given by

$$\begin{bmatrix} \boldsymbol{y}_{\mathrm{Pre}} \\ \boldsymbol{y}_{\mathrm{CP}} \\ \boldsymbol{y} \end{bmatrix} = \begin{bmatrix} \mathbf{H}_{\mathrm{Pre}} & \mathbf{0} & \mathbf{0} \\ \mathbf{0} & \mathbf{H}_{\mathrm{CP}} & \mathbf{0} \\ \mathbf{0} & \mathbf{0} & \mathbf{H} \end{bmatrix} \begin{bmatrix} \boldsymbol{p}_{\mathrm{Pre}} \\ \boldsymbol{x}_{\mathrm{CP}} \\ \boldsymbol{x} \end{bmatrix} + \boldsymbol{n}, \tag{4.7}$$

where $\boldsymbol{n}$ is the measurement noise which is modeled as Additive White Gaussian Noise (AWGN).

The received signal $\boldsymbol{y}_{\mathrm{Pre}}$

$$\boldsymbol{y}_{\mathrm{Pre}} = \mathbf{H}_{\mathrm{re}}\boldsymbol{p}_{\mathrm{pre}} + \boldsymbol{n} \tag{4.8}$$

is used to estimate initial model parameters for later channel estimation. $\boldsymbol{y}_{\mathrm{CP}}$ is removed to cancel inter−symbol interference. Finally, the received signal $\boldsymbol{y}$ corresponds to the Data-pilot block $\boldsymbol{x}$

$$\boldsymbol{y} = \mathbf{H}\boldsymbol{x} + \boldsymbol{n}, \tag{4.9}$$

serves the task of joint-channel estimation and data detection. In OFDM wireless communication systems, the time domain channel matrix $\mathbf{H}$ is circulant since the channel impulse response is constant during the OFDM symbol [84]. In underwater communication systems however, the channel impulse response varies within the OFDM symbol, because of the high Doppler spread factors compared to wireless channels. This fact translates into $\mathbf{H}$ semi-circulant has the following structure

$$\mathbf{H} = \Big[\boldsymbol{f}[1], \ldots, \boldsymbol{f}[i], \boldsymbol{f}[i+1], \ldots, \boldsymbol{f}[N]\Big]^{T}, \tag{4.10}$$

where $\boldsymbol{f}[i]$ is the discrete channel impulse response of the channel at discrete time i (rotated). The frequency domain received signal $\boldsymbol{Y}$ has the form

$$\boldsymbol{Y} \;=\; \mathbf{H}^{(f)}\boldsymbol{X} + \boldsymbol{\Phi}, \tag{4.11}$$

where $\mathbf{H}^{(f)}$ is the frequency domain channel matrix given by

$$\mathbf{H}^{(f)} \;=\; \mathbf{F}\mathbf{H}\mathbf{F}^{\mathrm{H}}, \tag{4.12}$$

where $\mathbf{F}$ is Discrete Fourier Transform (DFT) matrix of size $N \times N$. The frequency domain measurement noise $\boldsymbol{\Phi}$ is modeled as AWGN.

4.2.4 Underwater Channel Model

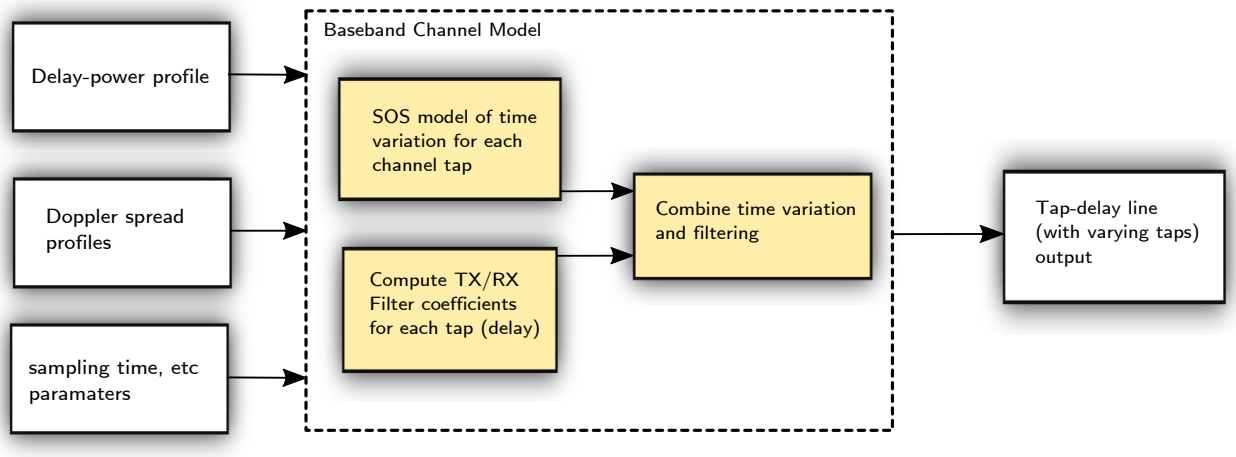

Figure 4.5: Channel model block diagram

For channel generation to produce the time-varying channel taps $f_k[i]$ to build channel matrix $\boldsymbol{H}$, we use the developed model of base-band underwater acoustic channel [1]. Figure 4.5 shows the stages of the channel generation procedure. First, a tap-delay profile of the underwater channel is selected, generated using a ray-tracing software such as Bellhop [2], or obtained from sea trials. The next step is to add the feature of channel path variation with time to each channel path l, $l = 1, 2, \cdots, L_p$ via the sum-of-sinusoids (SOS) approach [85].

$$f_l^{SoS}[i] = \sqrt{\frac{P_l}{M}} \sum_{m=1}^{M} e^{j(\phi_m + 2\pi f_m i T_s)}, \tag{4.13}$$

where P_l is the power of the l^{th} path extracted from the normalized power delay profile (PDP) of the channel. The initial phases ϕ_m, $m = 1, 2, \cdots, M$ are chosen uniformly randomly within the interval $[0, 2\pi)$ while the frequencies f_m are chosen such that the scattering function (Doppler spread function) of the tap follows

$$S(\nu) = \frac{1}{2\alpha_l} e^{\frac{-|\nu|}{\alpha_l}}, \tag{4.14}$$

typical for underwater acoustic channels [41], where α_l is the root-mean square (rms) of the Doppler spread for channel path l. Higher values of α_l corresponds to larger time variations in the channel impulse response, since (4.14) contains higher frequencies with considerable power. Clearly different channel taps may have different α_l's and it can be motivated that

higher α_l's correspond to the paths with larger number of the surface bounces [4]. If the number of surface bounces per channel tap is available via modeling (from Bellhop) we set the base value α per bounce and compute α_l per tap as the base value α multiplied by the number of the surface bounces experienced by the tap.

Channel taps $f_k[i]$, for $i = 1, 2, \cdots, N$ and $k = 1, 2, \cdots, N$ are obtained by applying transmit−receive root raised cosine (RRC) to each of the channel paths generated above (4.13), considering appropriate delays τ_l, $l = 1, 2, \cdots, L_{\mathrm{p}}$ from the power-delay profile. An example channel matrix $\mathbf{H}$ is visualized in Fig. 4.6. The channel PDP depicted in Fig. 4.6(c) extracted from sea trials performed in St Margaret's Bay of the coast off Nova Scotia. The Root Mean Square (RMS) Doppler per bounce has been set to $\alpha = 0.25$ Hz. Figure (4.6) shows instances for different values of RMS Doppler spread. The figures shows the multi-path effect and the time variation of taps amplitude within one OFDM symbol.

4.3 Iterative Interference Cancellation Receiver

In this section, we introduce the iterative receiver cancellation receiver for underwater doubly selective channel, and evaluate its performance using perfect channel knowledge. We show that through experiments that the described ICI cancellation process is effectively able to reach the interference free performance − for wide range of Doppler spread values.

4.3.1 Description of Operation

The iterative interference cancellation process flow diagram is shown in Figure 4.7. Using the given channel matrix $\mathbf{H}^{(f)}$, the received signal $\boldsymbol{Y}$ is matched filtered and the resultant $\boldsymbol{Y}_{\mathrm{MF}}$ is given by

$$\begin{aligned} \boldsymbol{Y}_{\mathrm{MF}} &= \mathbf{H}^{(f)*}\boldsymbol{Y} = \mathbf{H}^{(f)*}\mathbf{H}^{(f)}\boldsymbol{X} + \mathbf{H}^{(f)*}\boldsymbol{\Psi} \\ &= \mathbf{R}\boldsymbol{X} + \boldsymbol{\phi} \\ &= \mathbf{R}\boldsymbol{D} + \mathbf{R}\boldsymbol{P} + \boldsymbol{\phi}. \end{aligned} \tag{4.15}$$

where $\mathbf{R} = \mathbf{H}^{(f)*}\mathbf{H}^{(f)} =$, and is composed of data, pilot and measurement noise parts respectively. To retrieve the data part only, the pilot part signal is subtracted to yield

$$\begin{aligned} \boldsymbol{r} &= \boldsymbol{Y}_{\mathrm{MF}} - \mathbf{R}\boldsymbol{P} \\ &= \mathbf{R}\boldsymbol{D} + \boldsymbol{\phi}. \end{aligned} \tag{4.16}$$

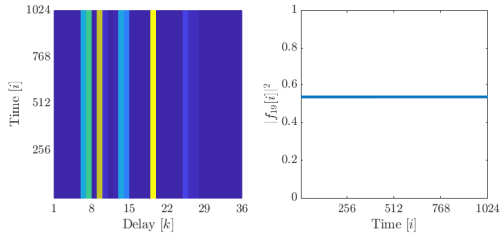

(a) $\alpha = 0.001$

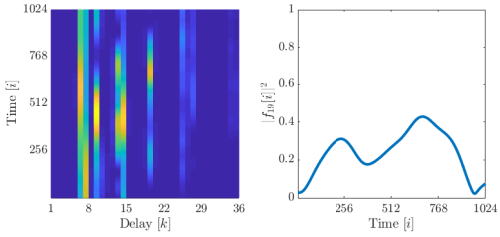

(b) $\alpha = 0.1$

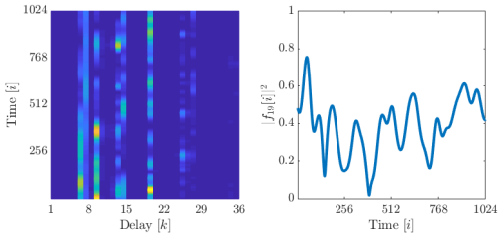

(c) $\alpha = 0.5$

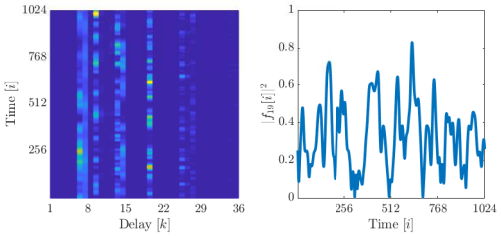

(d) $\alpha = 1.2$

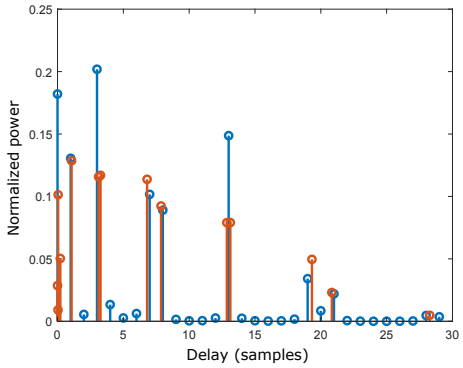

(e) Power Delay profile of measured Saint Margaret's Bay Channel

Figure 4.6: shows four instances of underwear channel impulse responses generated using the model shown in Figure 4.5, for different Doppler spread factors α. The bandwidth of RC filter = $B = 320Hz$. Figures to the left show evolution power of the channel impulse responses over the duration of OFDM symbol, and on the right shown the evolution of the power of one tap.

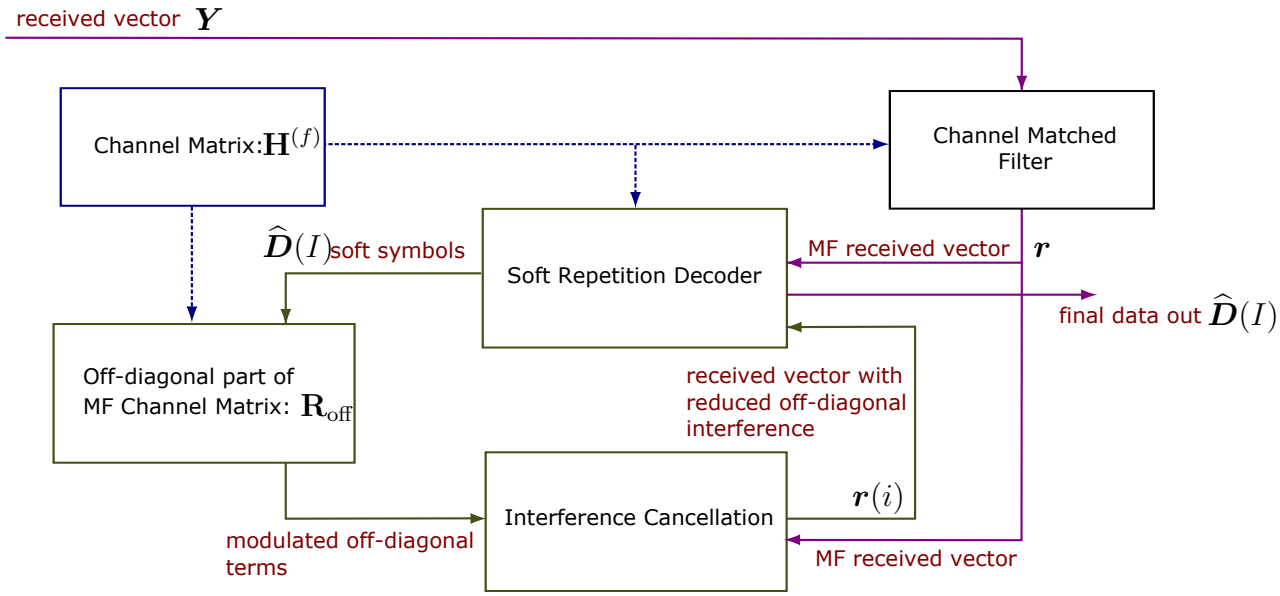

Figure 4.7: Iterative receiver diagram

For frequency selective only channel, the the matrix $\mathbf{H}^{(f)}$ is diagonal because time domain channel matrix $\mathbf{H}$ is perfectly circulant. For this case, the demodulation process is straight forward given by

$$D_k = \frac{r_{\text{D}}[k]}{R_{kk}} \tag{4.17}$$

where k is the index of the sub-carrier. This simple efficient data retrieval process is one of the reason behind adoption OFDM for frequency selective channels.

For Doubly selective channels, the matrix $\mathbf{R}$ is band diagonal, because of the semi-circulant nature of the time domain channel impulse response matrix $\mathbf{H}$. The higher the Doppler spread, the stronger the power of off-diagonal terms. By decomposing the matrix $\mathbf{R}$ into diagonal and non-diagonal elements,

$$\mathbf{R} = \mathbf{R}_{\text{diag}} + \mathbf{R}_{\text{off}} \tag{4.18}$$

where,

$$\mathbf{R}_{\text{diag}} = \text{diag}(\mathbf{R}), \tag{4.19}$$

$$\mathbf{R}_{\text{off}} = \mathbf{R} - \mathbf{R}_{\text{diag}}. \tag{4.20}$$

we can see clearly that by cancelling the off-diagonal we can implement the simple OFDM data demodulation in (4.17). The matrix $\mathbf{R}_{\text{diag}}$ represents the frequency selectivity of the channel, where time selectivity or Inter-carrier Interference is captured by $\mathbf{R}_{\text{off}}$.

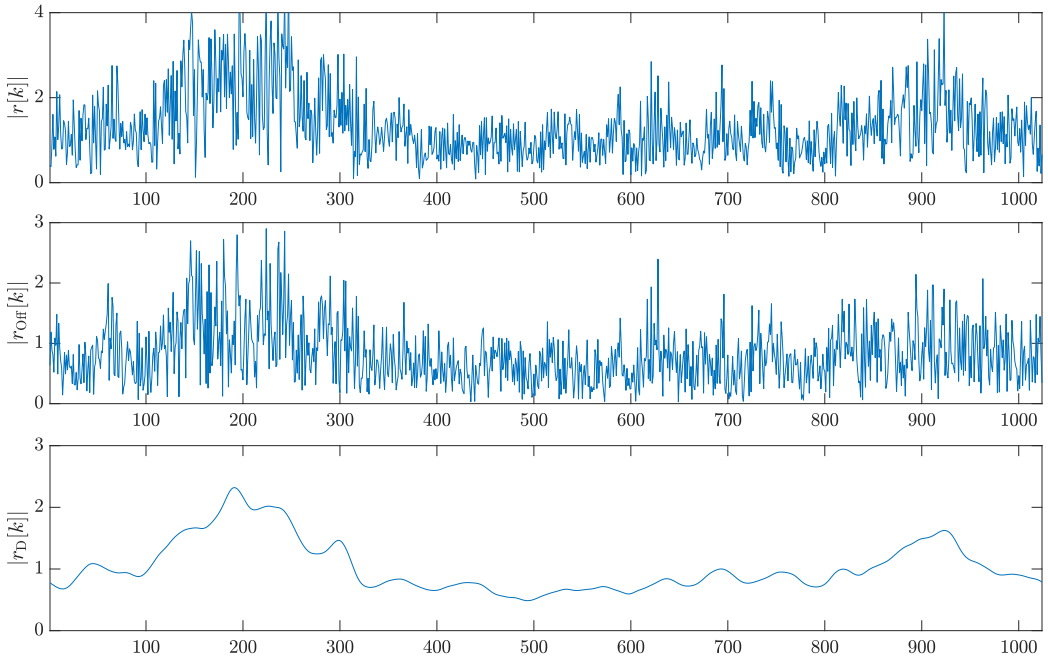

Figure 4.8: shows the matched filtered data only signal $\boldsymbol{r}$, interference signal $\boldsymbol{r}_{Off}$ and the interference-free signal $\boldsymbol{r}_{\text{D}}$. The iterative receiver cancellation iteratively cancel signal $\boldsymbol{r}_{\text{Off}}$ and produce $\boldsymbol{r}_{\text{D}}$ for demodulation. The bandwidth is $B = 320$ Hz, with Doppler spread of $\alpha = 1.2$ Hz.

The task of the setting in Figure 4.7 is to iteratively decode transmitted symbols $\boldsymbol{D}$ and remove the Inter-carrier Interference, or time selectivity effect of the channel. Figure 4.8 shows the target signal for interference free signal $r_{\text{D}}[k]$. Using $\boldsymbol{r}[0] = \boldsymbol{r}$, the soft repetition decoder/soft modulator unit shown in Figure 4.8 produces soft symbols $\widetilde{\boldsymbol{D}}[0]$. With the knowledge of the inter-carrier interference matrix $\mathbf{R}_{\text{off}}$, the interference signal is calculated as

$$\widetilde{\boldsymbol{r}}[0] = \mathbf{R}_{\text{off}}\widetilde{\boldsymbol{D}}[0] \tag{4.21}$$

which is then subtracted form the matched filter signal to cancel part of the inter-carrier interference, that is

$$\boldsymbol{r}[1] = \boldsymbol{r} - \widetilde{\boldsymbol{r}}[0],$$

and $\boldsymbol{r}[1]$ contains lower interference compared to $\boldsymbol{r}$. Similarly, at $i = 1$ with $\boldsymbol{r}[1]$, the estimate $\widetilde{\boldsymbol{D}}[1]$ is produced. The new data estimate is used to estimate the interference signal

$$\widetilde{\boldsymbol{r}}[1] = \mathbf{R}_{\text{diag}}\widetilde{\boldsymbol{D}}[1].$$

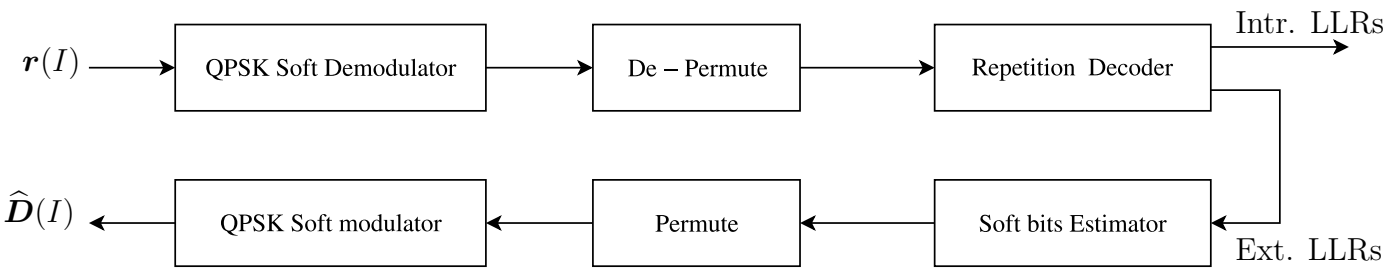

Figure 4.9: shows repetition decoder and and soft data generation.

The resulting interference signal is as well subtracted from the matched filter $\boldsymbol{r}$, and produce the signal

$$\boldsymbol{r}[2] = \boldsymbol{r} - \boldsymbol{r}_{\text{off}}[1],$$

which has lower inter-carrier interference compared to $\boldsymbol{r}[1]$ and $\boldsymbol{r}$. The cancellation process continues following

$$\boldsymbol{r}[I] = \boldsymbol{r} - \boldsymbol{r}_{\text{off}}[I-1]$$

until we reach the final iteration I_{final}, and the final data estimate then $\widetilde{\boldsymbol{D}}(I_{\text{final}})$. The described operation of the interference cancellation requires the channel knowledge represented by the two matrices $\mathbf{R}_{\text{off}}$ and $\mathbf{R}_{\text{diag}}$.

Figure (4.9) shows the steps to produce the soft symbols $\widehat{\boldsymbol{D}}$. At the QPSK soft demodulator, with the input $\boldsymbol{r}[i]$ and diagonal element $\mathbf{R}_{\text{diag}}$, we create an estimate of the QPSK symbol

$$\widehat{\boldsymbol{D}}[I] = \boldsymbol{r}[I]\mathbf{R}_{\text{diag}}^{-1} = \frac{\boldsymbol{r}[I]}{\mathbf{R}_{\text{diag}}}, \tag{4.22}$$

taking frequency-selectivity only, note as well we can employ the LMSSE estimate but comes at additional complexity especially the matrix inversion will be calculated at every iteration. The demodulaotr require the variance of interference and measurement noise

$$\sigma_{\text{D}}^2 = \frac{1}{N}\sum_k \text{var}\big(\widehat{D}_k[I-1] - D_k\big), \tag{4.23}$$

and practically we use $\widehat{\boldsymbol{D}}[I]$, that is

$$\sigma_{\mathrm{D}}^2 = \frac{1}{N}\sum_k \mathrm{var}\big(\widehat{D}[I]\big) \tag{4.24}$$

where we assume that $\sigma_{D_k}^2[I] \propto \sigma_D^2[I]$, where $\sigma_{D_k}^2[I]$ is the data variance at the tone k. we assume QPSK symbols at different frequency tones are independent from each other because of repetition with permutation. Optimal Conditional expectation for BPSK symbols in AWGN channel is used to calculate Log Likelihood Ration (LLR) for reapted BPSK symbols. The LLRs vector (size 2048) that is de-permuted to produce $\boldsymbol{s}[I]$ and forwarded to the Soft bits repetition decoder. The LLR of a bit b_i in $\boldsymbol{B}^{\mathrm{rep}}$ is calculated as following

$$\lambda(b_i)[I] = \frac{\sqrt{E_b}}{N_0 + \sigma_D^2[I]} s_i[I]. \tag{4.25}$$

To estimate the LLR of the information bit, the four replica of the soft bits are averaged, that is

$$\lambda(b_k)[I] = \frac{1}{M}\sum_{i\in\mathcal{K}} \lambda(b_i)[I], \tag{4.26}$$

where $\mathcal{K}$ is m elements set of indices of repeated bits correspond to information bit b_k. The extrinsic LLRs of the repeated bits is calculated

$$\lambda^{\mathrm{ext}}(b_i)[I] = \lambda(b_i)[I] - \lambda(b_k)[I], \tag{4.27}$$

and forwarded to the soft bits estimator, permuted and used to create the soft QPSK symbols $\widehat{\boldsymbol{D}}[I]$ is given by

$$\widehat{D}_j[I] = \tanh\left(\frac{\lambda(b_i)[I]}{2}\right) + \sqrt{-1}\,\tanh\left(\frac{\lambda(b_{i'})[I]}{2}\right), \tag{4.28}$$

where i and i' are two soft bits that make up the QPSK symbol and $\widehat{\boldsymbol{D}}[I]$ that is used for further interference cancellation in iteration $I+1$. Figure 4.10 shows the state evolution $(\sigma_{\mathrm{I}}^2, \sigma_{\mathrm{D}}^2)$ at each iteration I, where

$$\sigma_{\mathrm{I}}^2 = \frac{1}{N}\sum_k \mathrm{var}(r_{\mathrm{k}}[I]). \tag{4.29}$$

At first, the data estimate is poor but biased enough to reduce noise and interference power σ_{I}^2. In all cases of Doppler spread, the second iteration presents significant improvement in data estimate σ_{D}^2. The reduction of interference continues until $\sigma_{\mathrm{I}}^2 \approx \sigma_n^2$ where the interference is almost perfectly cancelled.

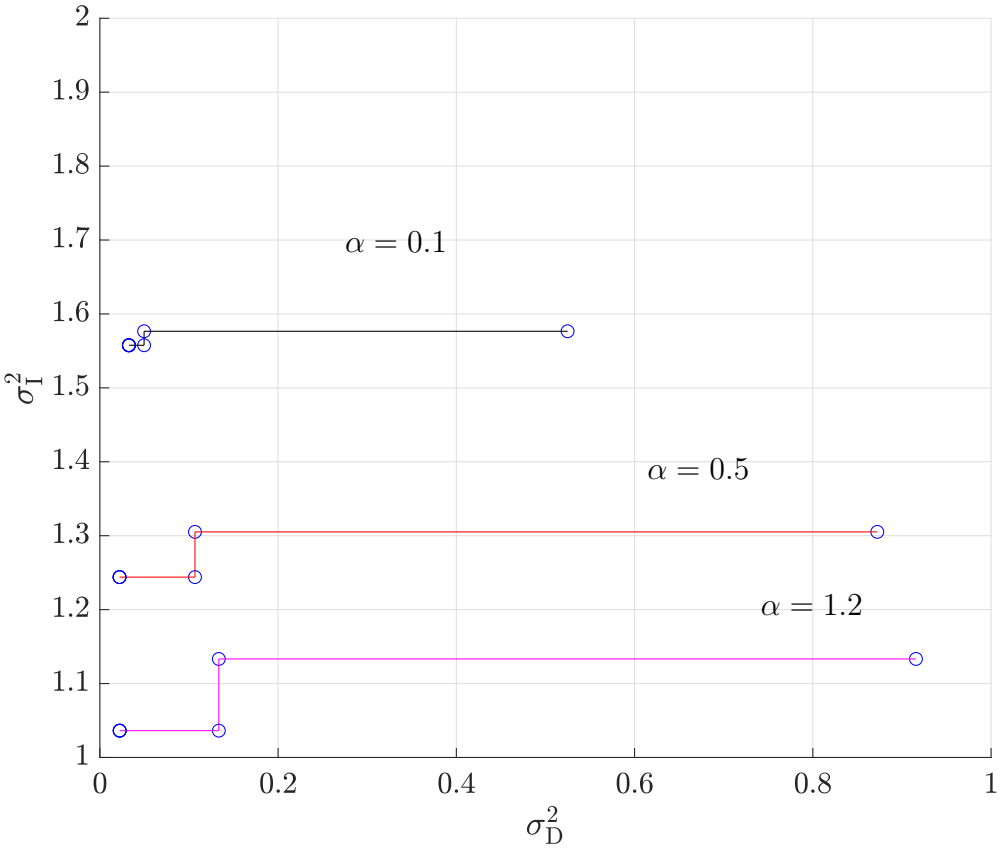

Figure 4.10: shows the evolution the reduction of σ_{D}^2 and σ_{I}^2 through the interference cancellation process. The final σ_{D}^2 values are 0.03257, 0.02206, 0.02222 for $\alpha = 0.1$, 0.5 and 1.2 respectively. The noise power $\sigma_n^2 = 0.2$ for $\frac{E_b}{N_o} = 10$ dB.

4.3.2 Experimental Performance

Figure (4.11) shows averaged Bit Error Rate (BER) of three underwater channels with Doppler spread of $\alpha = 0.1, 0.5$ and 1.2 Hz, with $B = 320$ Hz compared with the theoretical ML performance of QPSK over the AWGN channel. Noticeably, the higher the Doppler spread of the channel, the lower the BER because of the diversity introduced by the high fading, since fewer bits falls in deep fade as shown in Figure 4.12. The iterative receiver process can effectively remove the Inter-carrier Interference in case where we have full knowledge of the Channel information. In the next section we propose a channel estimation algorithm to be employed by the iterative receiver and can use the soft estimates $\widehat{\boldsymbol{D}}[I]$ to further enhance the channel estimate quality.

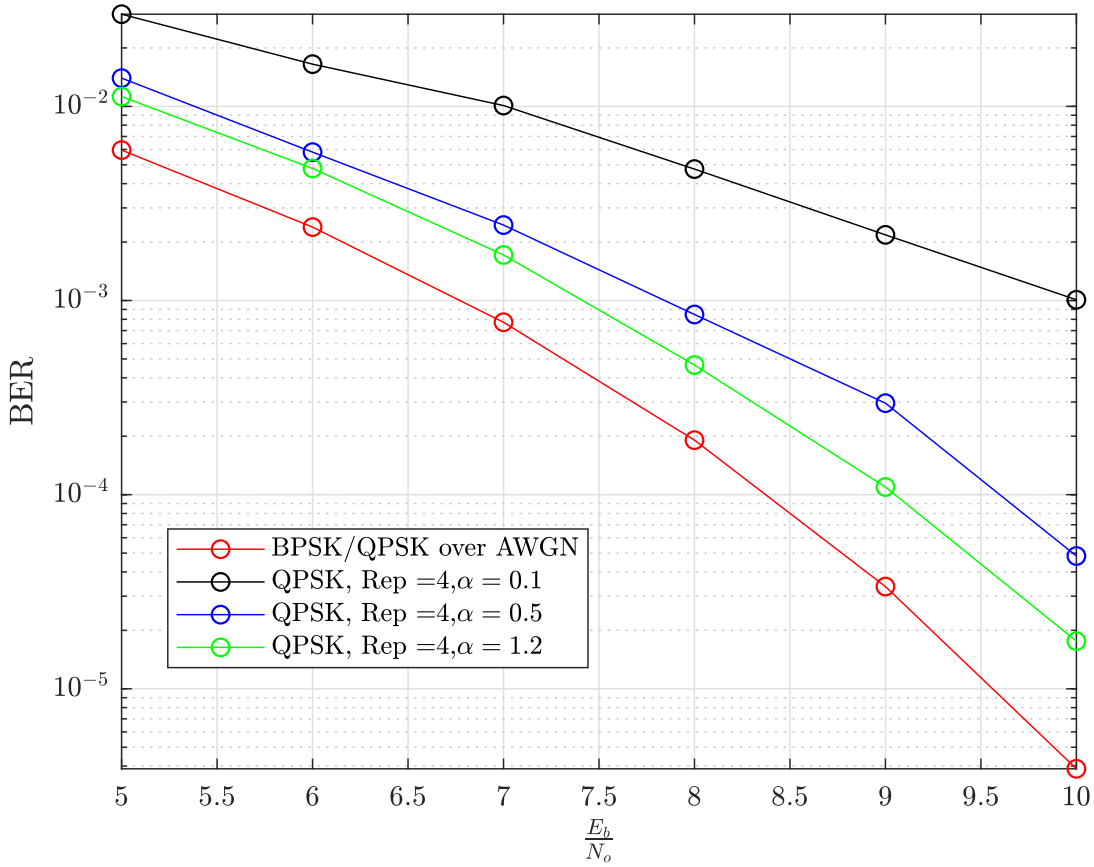

Figure 4.11: Simulated BER for the iterative receiver for the three channels, with Doppler spreads $0.1, 0.5$ and 1.2 Hz.

4.4 Chanel Estimation Algorithms for Underwater Channels

The iterative receiver described in Figure 4.7 fundamentally requires knowledge of channel matrix $\mathbf{H}$ to iterativly cancel ICI. In this section, we review available channel estimation algorithms utilized to acquire such channel knowledge.

Least mean Square adaptive filter is utilized in [86] to estimate and track residual Doppler shift change from one OFDM symbol to the next, with channel impulse response static during the symbol. The recursive least square (RLS) algorithm is employed in [87] to track frequency domain throughout OFDM symbols. It is well knows that as the step size of LMS algorithm increases, channel tracking ability is enhanced at the cost of estimation performance [88]. RLS algorithm converges much faster to solution compared to LMS but has poorer tracking ability.

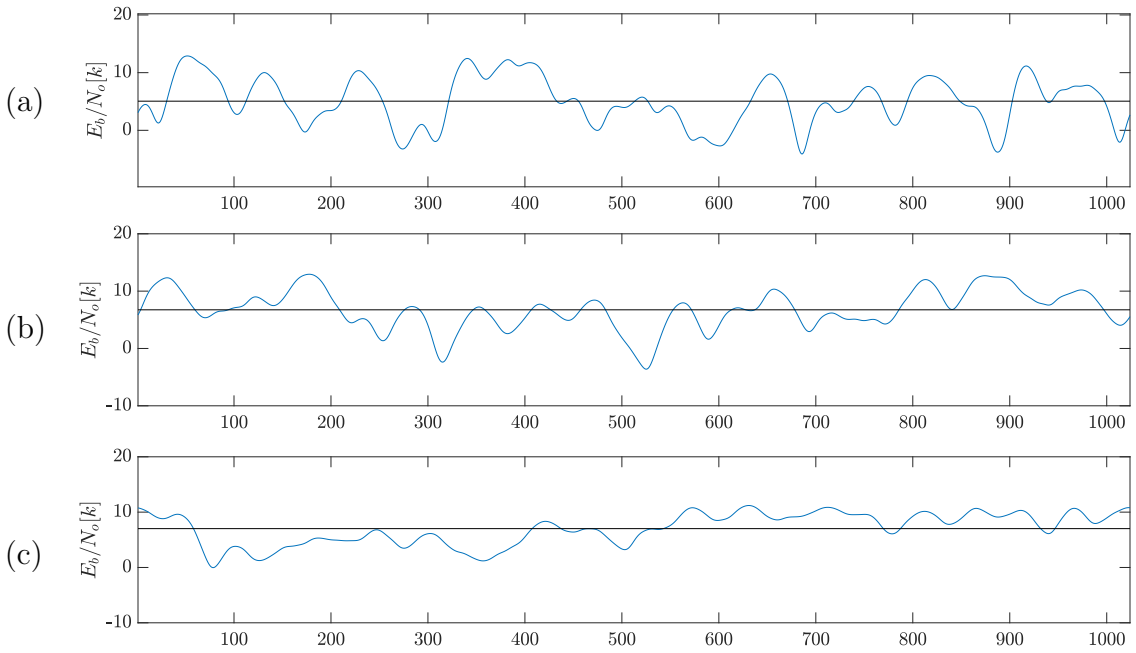

Figure 4.12: shows Eb/N_o [dB] for each frequency tone k in the interference free signal $r_{\mathrm{D}}[k]$ for Doppler spread values of $\alpha = 0.1, 0.5, 1.2$ respective to (a), (b) and (c). The higher the Doppler spread value, the less variation of the E_b/N_o and lower probability that $r_{\mathrm{D}}[k]$ falls into a deep fade, hence less construction errors.

Another model agnostic approach is presented in [89] where subspace projections methods of multiple signal classification (MUSIC) and Estimation of signal parameters via rotational in-variance techniques (ESPIRT) algorithms are employed for small to moderate Doppler spreads, and Compressing sensing approaches like orthogonal matching pursuit (OMP) and basis pursuit (BP) for high Doppler at cost of increasing the delay resolution and dictionary sizes. The various algorithms presented compared with Least Squares (LS) and found that compressed sensing is the most performant. Note that these methods don't rely on channel models. A Bayesian model based solution for a case when the channel is static throughout the duration of one OFDM symbol is detailed in [90], where the channel is estimated in frequency domain. The latter approach, however, can only be applied for low Doppler spreads. In [91] OMP is applied to underwater channels, after Carrier frequency offset removal and the impulse response is assumed constant during OFDM symbol with carrier offset as source of ICI. In [92], various algorithms investigated and sparse estimation OMP, BP is shown to provide better performance than diversity combing algorithms like MUSIC and ESPIRT. The channel taps are assumed constant during the block with residual mean Doppler shift as source of ICI.

In [93], instead of explicit estimation of the channel, a sparse estimate of delay−Doppler spread function that captures both channel structure and dynamics (time variation of paths and Doppler variation with each path) is found using OMP, BP and LS-OMP assuming the function stays constant for window of time. The validity of this assumption depends on the length of the window and the rate of change of the function. Path Identification (PI) algorithms are presented in [94] [95][96] to target the analog path estimation without relying on channel model. Low rank OFDM approximation is used to enhance the channel estimation of frequency selective channels is shown in [97].

Another cohort of algorithms is focused in changing the nature of the channel from doubly selective to frequency selective using transformations. In [98] an exponential basis expansion model (EBEM) is applied to model doubly selective wireless channels. For a time block, the channel is represented by the EBEM expansion coefficients that are assumed to change slowly from one time block to next − but time invariant within the block. First order auto regressive AR(1) model is assumed for parameter evolution and Kalman filter is presented for tracking and data detection. A polynomial based BEM is utilized in [99] to model the evolution of each channel tap independently, and a Kalman filter is applied to track each

tap. The model serves as a compression method to reduce Kalman filters complexity. The Doppler spread range is relatively small $0.1 - 0.3$, as it is used for EM wireless doubly selective channels. In [100] it is shown that discrete prolate spheroidal sequence (DPSS) BEM represents the channel better than discrete Fourier transform DFT BEM in terms of modeling error and bias.

Most of the methods mentioned assume quasi static channel during OFDM symbol, and ICI resulting from Doppler shifts. Additionally, depending on the bandwidth and carrier frequency, the underwater channel may not exhibit the sparse paths structure. What we target here is simple model based, that can perform both initial channel estimation and tracking − for wide range of Doppler spreads factors.

In this section we consider a time domain channel estimation approach[101]. The time domain formulation lends itself to state space models and utilizes statistical information about the channel and provide the estimation algorithm with an ability to track the evolution of the channel throughout each OFDM symbol. Given the linear observation model of the received sequence, state-space model for the channel evolution, the Kalman filter presents itself as the optimal estimator and tracker. It is important to note, however, that the entire vector of received samples is provided to the estimator upon reception of each OFDM symbol. Hence, we propose to utilize two Kalman filter estimators to run simultaneously, one in forward time direction and the other in backward, and combine the results of each run. The forward backward estimator is designed to operate as a part of the iterative receiver. At each iteration the estimator provides the interference canceller and the soft-bit decoder with an estimate of the channel, and the estimator receives back a soft-data pilot. At the beginning of the iterations the estimator starts from a known pilot sequence which is superimposed on the OFDM data symbol. As iterations progress the estimator is able to benefits from partially decoded data in addition to the pilot sequence to improve channel estimation quality and consequently lower error of decoded bits. The section is organized as follows: quick review of system model, the channel estimation setup and channel-state space model are presented in Section 5.3 and Section 4.5 respectively. The estimator and combiner are described in in Section 4.6. The experimental results are presented in Section 4.8. Section 4.10 presents the iterative OFDM receiver with channel estimation and soft decoding.

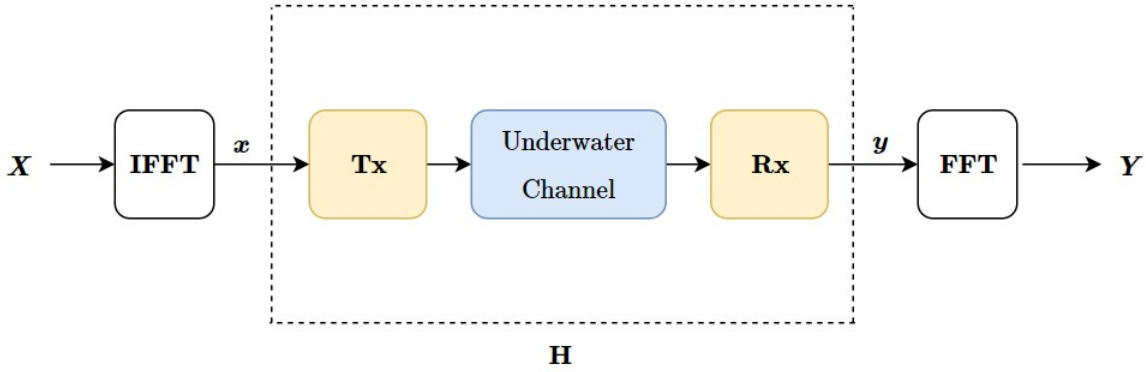

Figure 4.13: Equivalent channel **H** used in the linear OFDM model.

System model review

We consider an OFDM underwater acoustic communication system setup depicted in Fig. 4.13. The N transmitted signal samples in the frequency domain (that form one OFDM symbol) are denoted by $\boldsymbol{X} = (X_1, X_2, \cdots, X_N)$. The vector $\boldsymbol{X}$ is modulated into the time domain sampled signal vector $\boldsymbol{x} = (x_1, x_2, \cdots, x_N)$ using an inverse Fourier transform of size N and transmitted through underwater acoustic channel. The received time domain observations vector $\boldsymbol{y}$ is supplied to a Fourier transform to generate the frequency domain observations $\boldsymbol{Y}$. The physical channel (in blue) is sampled and the resulting channel impulse response matrix is denoted by **H**. The OFDM time domain observation model, after removing the cyclic prefix, is given by (ISI model)

$$y_i = \sum_{k=0}^{L-1} f_k[i] x_{i-k} + n_i \tag{4.30}$$

where L is the number of discrete channel taps and $f_k[i]$ is the kth term of the channel impulse response $\boldsymbol{f}[i]$ at time i. In matrix format

$$\boldsymbol{y} = \mathbf{H}\boldsymbol{x} + \boldsymbol{n} \tag{4.31}$$

where $\boldsymbol{y}$, $\boldsymbol{x}$, **H** and $\boldsymbol{n}$ are the $N \times 1$ time domain observation vector, the $N \times 1$ OFDM time domain symbols, the $N \times N$ time domain channel matrix and the $N \times 1$ observation noise,

and N is the size of one OFDM symbol. The matrix $\mathbf{H}$ has the general form

$$\mathbf{H} = \begin{bmatrix} \boldsymbol{f}[1] \\ \vdots \\ \boldsymbol{f}[i] \\ \boldsymbol{f}[i+1] \\ \vdots \\ \boldsymbol{f}[N] \end{bmatrix}. \tag{4.32}$$

Note that, because of the convolution and removed cyclic prefix, the elements of consecutive rows (channels) are right−shifted by one position. A visual representation of $\mathbf{H}$ is shown in Figure 4.15. The channel equation in frequency domain in matrix form is given by

$$\boldsymbol{Y} = \mathbf{H}^{(f)}\boldsymbol{X} + \boldsymbol{\Psi} = \mathbf{F}\mathbf{H}^{(f)}\mathbf{F}^{-1}\boldsymbol{X} + \mathbf{F}\boldsymbol{n} \tag{4.33}$$

where $\mathbf{F}$ is the matrix of the Fourier transform coefficients.

4.5 Channel estimation setup

Consider the task of estimating the channel matrix $\mathbf{H}$ based on the signal $\boldsymbol{x}$ that consists solely of a pilot signal. To be specific, the pilots-only minimum mean-squared error (MMSE) channel estimator is the solution to the minimization problem

$$\begin{aligned} \hat{\mathbf{H}} &= \arg\min_{\widetilde{\mathbf{H}}} \mathbb{E}\left\{ \left| \widetilde{\mathbf{H}} - \mathbf{H} \right|_F^2 \middle| \boldsymbol{y} \right\} \\ &= \sum_{i=1}^{N} \arg\min_{\widetilde{\boldsymbol{f}}[i]} \mathbb{E}\left\{ \left| \widetilde{\boldsymbol{f}}[i] - \boldsymbol{f}[i] \right|^2 \middle| \boldsymbol{y} \right\} \end{aligned} \tag{4.34}$$

where F is the Frobenius norm, and $\widetilde{\mathbf{H}}$ and $\widetilde{\boldsymbol{f}}[i]$ are optimization variables. The solution to (4.34) is minimum mean square error (MMSE) estimator of the form

$$\widehat{\mathbf{H}} = \mathbb{E}_{\mathbf{H}}\left\{ \mathbf{H} \middle| \boldsymbol{y} \right\} \tag{4.35}$$

or

$$\widehat{\boldsymbol{f}}[i] = \mathbb{E}_{\boldsymbol{f}[i]}\left\{ \boldsymbol{f}[i] \middle| \boldsymbol{y} \right\} \tag{4.36}$$

We notice that a direct attempt to solve (4.35) would require solving for N^2 unknowns based on a vector $\boldsymbol{y}$ of N observations. This is in contrast with the estimator (4.36), where the

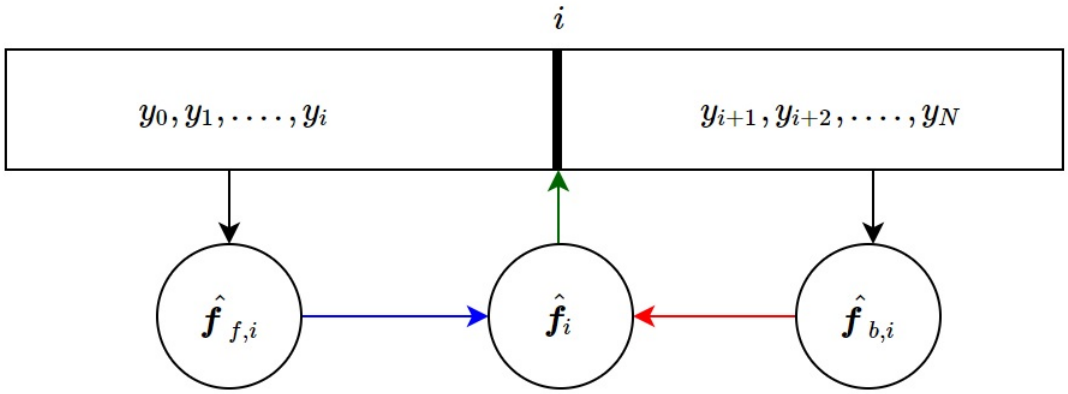

Figure 4.14: Illustration of the estimator in (4.36). The first step is to calculate the estimates $\hat{\boldsymbol{f}}_{b,i}$ and $\hat{\boldsymbol{f}}_{f,i}$ using past and future observations ,respectively. Then we combine the two estimates to find the final estimate $\hat{\boldsymbol{f}}_i$.

estimator conserves the number of variables to be estimated but requires a more structured implementation — through the vehicle of state-space model. The estimator (4.36) seeks the channel impulse response at discrete time instants i *using observations available from time* 0 *up to time* N, that is, it uses the *past* observations in the interval $[0 \rightarrow i]$ and the *future* observations in the interval $[i+1 \rightarrow N]$. One way to address this is to employ a two−step estimation strategy depicted in Figure 4.14. First, estimate the channel using *past* observations alone and then estimate the channel using *future* observations, that is

$$\widehat{\boldsymbol{f}}_f[i] = \mathbb{E}\left\{\boldsymbol{f}[i] | \{y[0], y[1], \ldots, y[i]\}\right\} \tag{4.37}$$

$$\widehat{\boldsymbol{f}}_b[i] = \mathbb{E}\left\{\boldsymbol{f}_i | \{y[i+1], y[i+2], \ldots, y[N]\}\right\} \tag{4.38}$$

where $\widehat{\boldsymbol{f}}_f[i]$ is the forward direction estimate and $\widehat{\boldsymbol{f}}_b[i]$ is the backward direction estimate. The second step is to combine the estimates optimally, that is

$$\bar{\boldsymbol{f}}[i] = \mathbb{E}_{\boldsymbol{f}[i]}\left\{\boldsymbol{f}[i] \middle| \widehat{\boldsymbol{f}}_f[i], \widehat{\boldsymbol{f}}_b[i]\right\}. \tag{4.39}$$

The estimate (4.39) considers the information from time 0 up to time N. Another approach to accumulating information is applying a smoother to the calculated forward estimates.

The estimators (4.37), (4.38) and (4.39) hint at how consecutive estimates (for example $\widehat{\boldsymbol{f}}_f[i]$ and $\widehat{\boldsymbol{f}}_f[i+1]$) can be computed if we have a model that describes the evolution of channel

$$\begin{bmatrix} f_1[i] \\ f_2[i] \\ \vdots \\ f_L[i] \end{bmatrix} = \begin{bmatrix} a_{AR(1)} & 0 & \dots & 0 \\ 0 & a_{AR(1)} & \dots & 0 \\ \vdots & \dots & \ddots & \vdots \\ 0 & 0 & \dots & a_{AR(1)} \end{bmatrix} \begin{bmatrix} f_1[i-1] \\ f_2[i-1] \\ \vdots \\ f_L[i-1] \end{bmatrix} + \begin{bmatrix} v_1[i] \\ v_2[i] \\ \vdots \\ v_L[i] \end{bmatrix} \tag{4.40}$$

impulse response. Such a model will allow the estimators to become trackers. Moreover, the model allows us to exploit the fact that consecutive channel impulse responses are highly correlated. Motivated by these two observations, we develop a state space model for the channel, and with it we can move the estimator into the Kalman filter form.

4.5.1 Channel State Space Model

The estimator in (4.37) relies on calculating the conditional expected value which requires the probability density function (pdf) $p(\boldsymbol{f}[i])$. Even if we have the joint pdf of the channel impulse response taps, calculating $\mathbb{E}\{.\}$ is computationally expensive. This observation motivates us to model the channel evolution $\boldsymbol{f}[i]$ taps over time using a simple state-space model for the channel. Flexibility of simple state space model allows Kalman filter, as a tracking algorithm, to augment additional information in its state-space model such as motion models for the transmitter or receiver. State space models allow for separation of physical environment information from tracking algorithm and reduce the need to customize tracking algorithms steps itself.

4.5.2 AR(1) Model

The AR(1) model is the simplest model for the channel and has the form (4.40), where $f_k[i]$ is the k^{th} active tap (non-zero) in the channel impulse response $\boldsymbol{f}[i]$, and $v_k[i]$ is the corresponding Gaussian innovation noise of the AR(1) process of tap k. Note that here we are assuming that the taps are uncorrelated for simplicity. Because of filtering, adjacent channel taps are expected to be correlated (effectively the same analog tap). We explore a model without exploiting this potential correlation among neighboring taps. The model in (4.40) assumes an AR(1) process for each active tap, and all the taps share the same regression factor $a_{AR(1)}$ but differ in the innovation noise power $\sigma_v^2[k]$. The compact form of the state-space model of (4.40) is

$$\boldsymbol{f}[i] = \mathbf{A}^{(1)}\boldsymbol{f}[i-1] + \boldsymbol{v}[i]\,. \tag{4.41}$$

$$\begin{bmatrix} f_1[i+1] \\ f_2[i+1] \\ \vdots \\ f_L[i+1] \\ f_1[i] \\ f_2[i] \\ \vdots \\ f_L[i] \end{bmatrix} = \begin{bmatrix} a_{AR(2)} & 0 & \dots & b_{AR(2)} & \dots & 0 \\ 0 & a_{AR(2)} & \dots & 0 & b_{AR(2)} & 0 \\ \vdots & \dots & \dots & \dots & \vdots & \\ 0 & \dots & a_{AR(2)} & \dots & 0 & b_{AR(2)} \\ 1 & 0 & \dots & \dots & 0 & 0 \\ 0 & 1 & \dots & \dots & 0 & 0 \\ \vdots & \dots & \dots & \dots & \dots & \vdots \\ 0 & \dots & 1 & \dots & \dots & 0 \end{bmatrix} \begin{bmatrix} f_1[i] \\ f_2[i] \\ \vdots \\ f_L[i] \\ f_1[i-1] \\ f_2[i-1] \\ \vdots \\ f_L[i-1] \end{bmatrix} + \begin{bmatrix} v_1[i] \\ v_2[i] \\ \vdots \\ v_L[i] \\ 0 \\ 0 \\ \vdots \\ 0 \end{bmatrix} \tag{4.42}$$

4.5.3 The AR(2) Model

The AR(2) model has the form (4.42) and a compact representation

$$\boldsymbol{f}[i+1] = \mathbf{A}^{(2)}\boldsymbol{f}[i] + \boldsymbol{v}[i] \tag{4.43}$$

With the state-space models (4.41) and (4.43) for the channel, along with the linear observation model (4.31), we can use the Kalman filter to perform the channel estimation and tracking.

4.6 Kalman Filter and Combiner

In this section we first review Kalman filter recursions for for the first step in estimation, and then present combining strategy of estimates. The results is compared with model agnostic adaptive algorithms widely used in literature of channel estimation and tracking.

4.6.1 Kalman filter formulation

Consider a known pilot signal $\boldsymbol{x}$ and the linear observation model and the state space model assumed for the channel evolution

$$y[i] = \boldsymbol{f}[i]\,\boldsymbol{x} + n[i] \tag{4.44}$$

$$\boldsymbol{f}[i+1] = \mathbf{A}^{(1)}\boldsymbol{f}[i] + \boldsymbol{v}[i]\,. \tag{4.45}$$

The Kalman filter for the forward estimates of $\hat{\boldsymbol{f}}_f[i] = \mathbb{E}\left\{\boldsymbol{f}[i]\middle|\{y[0]\dots y[i]\}\right\}$. is given by

$$\begin{aligned}
\sigma_e^2[i] &= \sigma_n^2 + \boldsymbol{x}^*\mathbf{M}_f[i|i-1]\boldsymbol{x} && (4.46)\\
\boldsymbol{K}_f[i] &= \tfrac{\mathbf{M}_f[i|i-1]\boldsymbol{x}}{\sigma_e[i]^2} && (4.47)\\
e[i] &= y[i] - \hat{\boldsymbol{f}}_f[i|i-1]\boldsymbol{x} && (4.48)\\
\hat{\boldsymbol{f}}_f[i|i] &= \hat{\boldsymbol{f}}_f[i|i-1] + \boldsymbol{K}_f[i]e[i] && (4.49)\\
\hat{\boldsymbol{f}}_f[i|i+1] &= \mathbf{A}^{(1)}\hat{\boldsymbol{f}}_f[i|i] && (4.50)\\
\mathbf{M}_f[i|i] &= \mathbf{M}_f[i|i-1] \\
&\quad - \tfrac{\mathbf{M}_f[i|i-1]\boldsymbol{x}\boldsymbol{x}^*\mathbf{M}_f[i|i-1]}{\sigma_e^2[i]} && (4.51)\\
\mathbf{M}_f[i+1|i] &= \mathbf{A}^{(1)H}\mathbf{M}_f[i|i]\mathbf{A}^{(1)} + \mathbf{Q}^{(1)} && (4.52)
\end{aligned}$$

where the subscript f indicates the forward estimate $\mathbf{M}_f[i]$ is its error co-variance matrix. The forward Kalman filter runs from time $i = 0$ up to $i = N$. For backward run from time $i = N$ up to time $i = 0$, change the subscript to b indicating the *backward* filter. Similarly, for the AR(2) channel model we have

$$\begin{aligned}
\begin{bmatrix} y[i] \\ y[i-1] \end{bmatrix} &= \boldsymbol{f}[i]^{(2)} \begin{bmatrix} \boldsymbol{x} & 0 \\ 0 & \boldsymbol{x} \end{bmatrix} + \begin{bmatrix} n[i] \\ n[i-1] \end{bmatrix} \\
\boldsymbol{y}[i] &= \boldsymbol{f}[i]\boldsymbol{x} + \boldsymbol{n}[i] && (4.53)\\
\boldsymbol{f}[i+1] &= \mathbf{A}^{(2)}\boldsymbol{f}[i] + \boldsymbol{v}[i] && (4.54)
\end{aligned}$$

and the Kalman recursion for the AR(2) setting is

$$\begin{aligned}
\mathbf{R}_e[i] &= \sigma_n^2\mathbf{I}_2 + \boldsymbol{x}^*\mathbf{M}_f[i|i-1]\boldsymbol{x} && (4.55)\\
\boldsymbol{K}_f[i] &= \mathbf{M}_f[i|i-1]\boldsymbol{x}\mathbf{R}_e[i]^{-1} && (4.56)\\
\boldsymbol{e}[i] &= \boldsymbol{y}[i] - \hat{\boldsymbol{f}}_f[i|i-1]\boldsymbol{x} && (4.57)\\
\hat{\boldsymbol{f}}_f[i|i] &= \hat{\boldsymbol{f}}_f[i|i-1] + \boldsymbol{K}_f[i]\boldsymbol{e}[i] && (4.58)\\
\hat{\boldsymbol{f}}_f[i|i+1] &= \mathbf{A}^{(2)}\hat{\boldsymbol{f}}_f[i|i] && (4.59)\\
\mathbf{M}_f[i|i] &= \mathbf{M}_f[i|i-1] \\
&\quad - \mathbf{M}_f[i|i-1]\mathbf{x}\mathbf{R}_e[i]^{-1}\mathbf{x}^*\mathbf{M}_f[i|i-1] && (4.60)\\
\mathbf{M}_f[i+1|i] &= \mathbf{A}^{(2)H}\mathbf{M}_f[i|i]\mathbf{A}^{(2)} + \mathbf{Q}^{(2)} && (4.61)
\end{aligned}$$

4.6.2 Combining of the Estimates $\hat{\boldsymbol{f}}_f[i|i]$ and $\hat{\boldsymbol{f}}_b[i|i]$

Up to this point we have two estimates of the channel, forward and a backward, namely $\hat{\boldsymbol{f}}_f[i|i]$ and $\hat{\boldsymbol{f}}_b[i|i]$ with error co-variance matrices $\mathbf{M}_f[i|i]$ and $\mathbf{M}_b[i|i]$ respectively. The task now is to merge the two estimates into one refined estimate. We first explain optimal combing in its general setting as in [102] and then apply the result to the channel estimation case in hand. Consider the following two linear systems:

$$\boldsymbol{y}_1 = \mathbf{A}_1\boldsymbol{w} + \boldsymbol{q}_1 \tag{4.62}$$

$$\boldsymbol{y}_2 = \mathbf{A}_2\boldsymbol{w} + \boldsymbol{q}_2 \tag{4.63}$$

where $\boldsymbol{y}_1$, $\boldsymbol{y}_2$ are observation vectors, $\mathbf{A}_1$,$\mathbf{A}_2$ are the sensing matrices, and $\boldsymbol{q}_1$,$\boldsymbol{q}_2$ are Gaussian observation noise vectors and independent from each other. The task is to estimate $\boldsymbol{w}$. The linear minimum mean-square estimator of $\boldsymbol{w}$ for each system separately is given by

$$\begin{aligned}\widehat{\boldsymbol{w}}_1 &= [\mathbf{R}_w^{-1} + \mathbf{B}_1^*\mathbf{R}_{q1}^{-1}\mathbf{B}_1]^{-1}\mathbf{B}_1^*\mathbf{R}_{q1}^{-1}\boldsymbol{z}_1 \\ &= \mathbf{M}_1\mathbf{B}_1^*\mathbf{R}_{q1}^{-1}\boldsymbol{z}_1 \end{aligned} \tag{4.64}$$

where $\mathbf{M}_1$ is the error co-variance matrix of the estimate $\widehat{\boldsymbol{w}}_1$ using the observations model (36) only. Similarly, the estimate of $\boldsymbol{w}$ using the linear model in (4.63) only is

$$\widehat{\boldsymbol{w}}_2 = \mathbf{M}_2\mathbf{R}_{q2}^{-1}\boldsymbol{z}_2\,. \tag{4.65}$$

Now we calculate the estimate given both $\boldsymbol{z}_1$ and $\boldsymbol{z}_2$ and to do that we find the concatenated linear system of (4.62) and (4.63), which has the form

$$\begin{aligned}\begin{bmatrix}\boldsymbol{y}_1\\ \boldsymbol{y}_2\end{bmatrix} &= \begin{bmatrix}\mathbf{A}_1\\ \mathbf{A}_2\end{bmatrix}\boldsymbol{w} + \begin{bmatrix}\boldsymbol{q}_1\\ \boldsymbol{q}_2\end{bmatrix} \\ \boldsymbol{y} &= \mathcal{A}\boldsymbol{w} + \boldsymbol{q}\end{aligned} \tag{4.66}$$

which has the solution

$$\begin{aligned}\widehat{\boldsymbol{w}} &= \left(\mathbf{R}_w^{-1} + \mathcal{A}^*\mathcal{R}_q\mathcal{A}\right)^{-1}\mathcal{A}^*\mathcal{R}_q^{-1}\boldsymbol{y} \\ &= \left(\mathbf{R}_w^{-1} + \mathbf{B}_1^*\mathbf{R}_{q1}^{-1}\mathbf{B}_1 + \mathbf{B}_2^*\mathbf{R}_{q2}^{-1}\mathbf{B}_2\right)^{-1} \\ &\quad \cdot \left(\mathbf{B}_1^*\mathbf{R}_{q1}^{-1}\boldsymbol{z}_1 + \mathbf{B}_2^*\mathbf{R}_{q2}^{-1}\boldsymbol{z}_2\right) \\ &= \left(\mathbf{M}_1^{-1} + \mathbf{M}_2^{-1} - \mathbf{R}_w^{-1}\right)^{-1}\left(\mathbf{B}_1^*\mathbf{R}_{q1}^{-1}\boldsymbol{z}_1 + \mathbf{B}_2^*\mathbf{R}_{q2}^{-1}\boldsymbol{z}_2\right) \\ &= \mathbf{M}\left(\mathbf{B}_1^*\mathbf{R}_{q1}^{-1}\boldsymbol{z}_1 + \mathbf{B}_2^*\mathbf{R}_{q2}^{-1}\boldsymbol{z}_2\right)\,. \end{aligned} \tag{4.67}$$

Using (4.62) and (4.63), the relationship between $\hat{\boldsymbol{w}}$, $\hat{\boldsymbol{w}}_1$ and $\hat{\boldsymbol{w}}_2$ is given by:

$$\mathbf{M}^{-1}\hat{\boldsymbol{w}} = \mathbf{M}_1^{-1}\hat{\boldsymbol{w}}_1 + \mathbf{M}_2^{-1}\hat{\boldsymbol{w}}_2 \tag{4.68}$$

$$\mathbf{M}^{-1} = \mathbf{M}_1^{-1} + \mathbf{M}_2^{-1} - \mathbf{R}_w\,. \tag{4.69}$$

Note that we can drop the term $\mathbf{R}_w$ when we have no prior auto-correlation information about $\boldsymbol{w}$. The Kalman filter is the implementation of the LMMSE when we have a state-space model of the channel, hence, we apply the above to the results of the forward-backward filter as follows:

$$\mathbf{M}[i|i] = [\mathbf{M}_f^{-1}[i|i] + \mathbf{M}_b^{-1}[i|i]]^{-1} \tag{4.70}$$

$$\begin{aligned}\hat{\boldsymbol{f}}^c[i|N] &= \mathbf{M}[i|i] \\ &\quad \cdot \left(\mathbf{M}_f^{-1}[i|i]\boldsymbol{f}_f[i|i] + \mathbf{M}_b^{-1}[i|i]\boldsymbol{f}_b[i|i]\right).\end{aligned} \tag{4.71}$$

4.6.3 Model Agnostic Channel Estimation

In this section we present standard methods to estimate the channel that do not assume the availability of a channel model, then compare with the Kalman filter combiner presented in previous section. If a channel is static during the OFDM symbol duration then the least-squares estimation of the channel along with the shift orthogonality property of the pilots results in a matched filter solution, which is optimal. When the channel starts to build up dynamics, the matched filter deteriorates and recursive least square (RLS) and least mean-squares (LMS) algorithms are typically employed.

Exponentially Weighted Recursive Least Squares (λ-RLS)

The λ-RLS [88] is a recursive linear MMSE estimator that puts more weight on the recent observation y_i using forgetting factor λ. The formulation is given by

$$\begin{aligned}\mathbf{M}_{\mathrm{RLS}}[i] &= \lambda^{-1}\mathbf{M}_{\mathrm{RLS}}[i-1] \\ &\quad - \lambda^{-2}\frac{\mathbf{M}_{\mathrm{RLS}}[i-1]\boldsymbol{x}_i^H\boldsymbol{x}_i\mathbf{M}_{\mathrm{RLS}}^H[i-1]}{\sigma_n^2 + \lambda^{-1}\boldsymbol{x}_i\mathbf{M}_{\mathrm{RLS}}[i-1]\boldsymbol{x}_i^H}\end{aligned} \tag{4.72}$$

$$e(i) = y_i - \hat{\boldsymbol{f}}_{\mathrm{RLS}}[i-1]\boldsymbol{x}_i \tag{4.73}$$

$$\begin{aligned}\hat{\boldsymbol{f}}_{\mathrm{RLS}}[i] &= \hat{\boldsymbol{f}}_{\mathrm{RLS}}[i-1] \\ &\quad + \frac{\lambda^{-1}\mathbf{M}_{\mathrm{RLS}}[i-1]\boldsymbol{x}_i}{\sigma_n^2 + \lambda^{-1}\boldsymbol{x}_i\mathbf{M}_{\mathrm{RLS}}[i-1]\boldsymbol{x}_i}e(i)\,.\end{aligned} \tag{4.74}$$

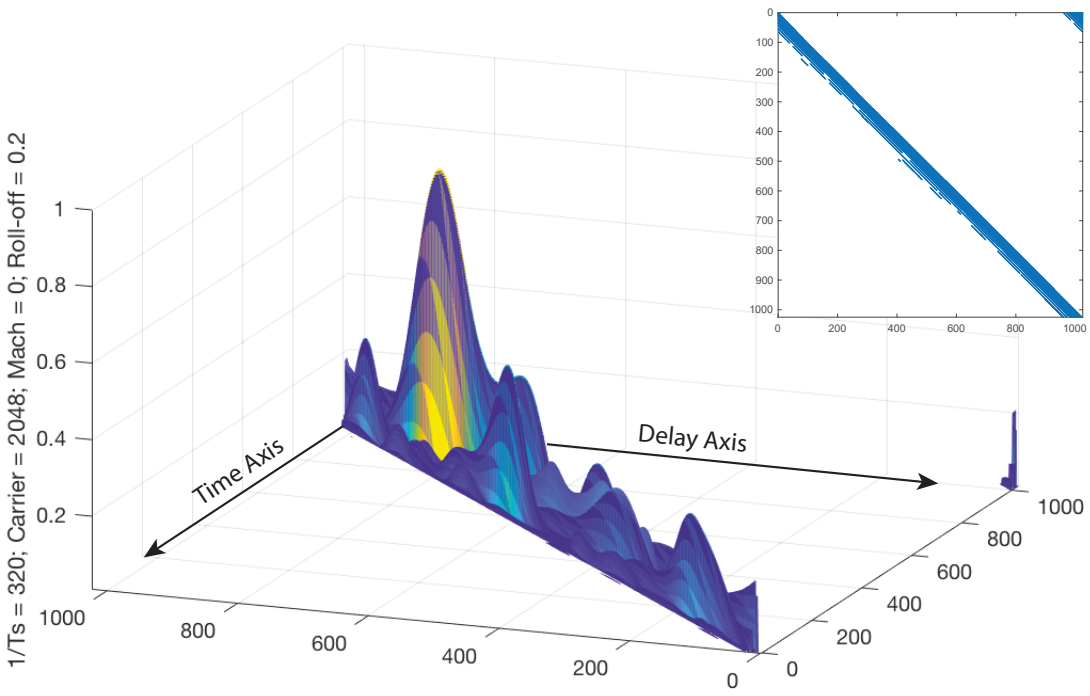

Figure 4.15: 3-D plot of the absolute value of the pseudo-circulant channel matrix **H** for the 1-km St. Margaret's Bay channel. The inset shows the significant values and illustrates the structure of **H**.

Note that we can run the RLS algorithm forward and backward and combine the resulting estimates using the optimal combiner.

Least Mean-Square (LMS) algorithm

The LMS algorithm is as well-known model-agnostic algorithm that is known for its robustness and tracking ability. The LMS algorithm for time-varying underwater channels has the form

$$\hat{\boldsymbol{f}}_{\mathrm{LMS}}[i] = \hat{\boldsymbol{f}}_{\mathrm{LMS}}[i-1] + \mu \boldsymbol{x}_i^H e(i) \tag{4.75}$$

$$e(i) = y_i - \boldsymbol{x}_i^T \hat{\boldsymbol{f}}_{\mathrm{LMS}}[i-1]\,. \tag{4.76}$$

where μ is the step size. The convergence condition for the LMS is given by

$$0 \;<\; \mu < \frac{2}{\mathrm{Tr}(\mathrm{R})_{\boldsymbol{x}}} \tag{4.77}$$

where N_L is the number of active taps under tracking. LMS algorithms are known for their slow convergence time compared to RLS algorithm.

4.7 Channel State Space Model Parameters

The parameter $a_{AR(1)}$ is found by fitting the auto-correlation function of the taps (4.13) with the auto-correlation function of the assumed AR(1) channel

$$R_{k,1}(m) = \mathbb{E}\left\{f_k[i] f_k^*[i+m]\right\} = R_{k,tr}(0) a_{AR(1)}^m \tag{4.78}$$

where $R_{k,1}(m)$ is the auto-correlation of tap k that follows the AR(1) model. The auto-correlation of $f_k^{SoS}[i]$ is

$$R_{k,SoS}[m] = \frac{P_k}{1 + (2\pi m \alpha T_s)^2} \tag{4.79}$$

where $R_{k,SoS}[m]$ is the auto-correlation of tap k that follows the SoS model, α is the Doppler exponential factor, and T_s is the sampling time. Th parameter $a_{AR(1)}$ is the solution to the minimization problem

$$a_{AR(1)} = \arg \min_{\bar{a}_{AR(1)}} \sum_m \|R_{k,1}[m] - R_{k,SoS}[m]\|^2 \tag{4.80}$$

and is independent of P_k. The power delay profile is needed to find the noise power $\sigma_v^2[k]$, that is

$$\sigma_v^2[k] = P_k (1 - a_{AR(1)})^2 . \tag{4.81}$$

4.8 Experimental Results

The algorithm is tested using a channel impulse response profile for the underwater channel measured in Saint Margaret's Bay located off the coast of Nova Scotia, Canada, where recent under-water channel sounding experiments have been performed. The acoustic environment is a shallow-water (depth of about $60 - 80$m) 1-km channel with hard bottom. The transmit carrier frequency was set to 2048 Hz, bandwidth to 320 Hz, and root-raised cosine filtering with 0.2 roll-off was applied at the transmitter and receiver. The high-resolution power delay profile of the channel is depicted in Fig. 4.16, where the x-axis represents the delay given in terms of signal samples. A snapshot of the time varying channel matrix $\mathbf{H}$ corresponding to this profile and the Doppler spread of $\alpha = 0.25$Hz per surface bounce is given in Fig. 4.15.

The channel is used to transmit the time-domain pilot sequence $\boldsymbol{x}$, and the observations $\boldsymbol{y}$ are used to run the Kalman filters. Two cases are considered for the Doppler spread, $\alpha = 0.1, 0.5$ Hz representing a calmer and a heavier sea environment. The number of surface

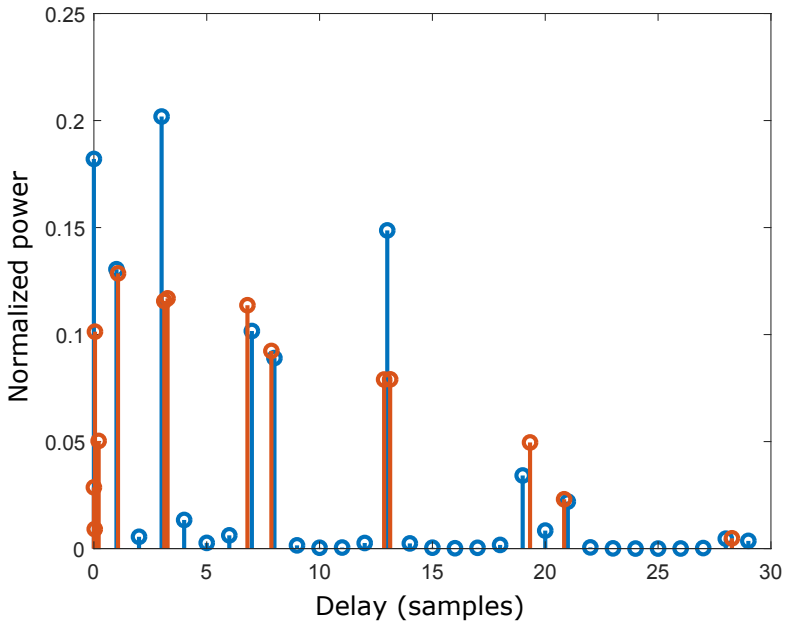

Figure 4.16: The high-resolution (orange) and post-filtered (blue) normalized power delay profiles of the Saint Margret's Bay channel.

bounces per tap varies from 0 to 6 depending on the tap. OFDM symbol duration is set to $N = 1024$ samples. The normalized mean-squared channel estimation error is plotted as a function of the system SNR in Fig. 4.17 results for $\alpha = 0.1$ (left) and $\alpha = 0.5$ (right). The Kalman filter is able to offer better estimates than LMS and RLS thanks to the knowledge about the channel exploited using state-space representation. The combiner offers an even better estimate because it can account for simultaneous availability of all observations.

4.8.1 AR(1) vs AR(2)

Before studying the channel estimator as a part of the iterative decoder, we first compare the Kalman filter optimal combiners with AR(1) and AR(2) channel state-space models. Fig. 4.18 shows the normalized MSE of the estimators with the two models. The performances provided by the two models are close. The Doppler spread factor used for the experiments presented in the figure equals $\alpha = 0.25$. The results suggest that further increasing the model order may not provide tangible gain. Investigation of AR(p) and improved models are a part of our ongoing work.

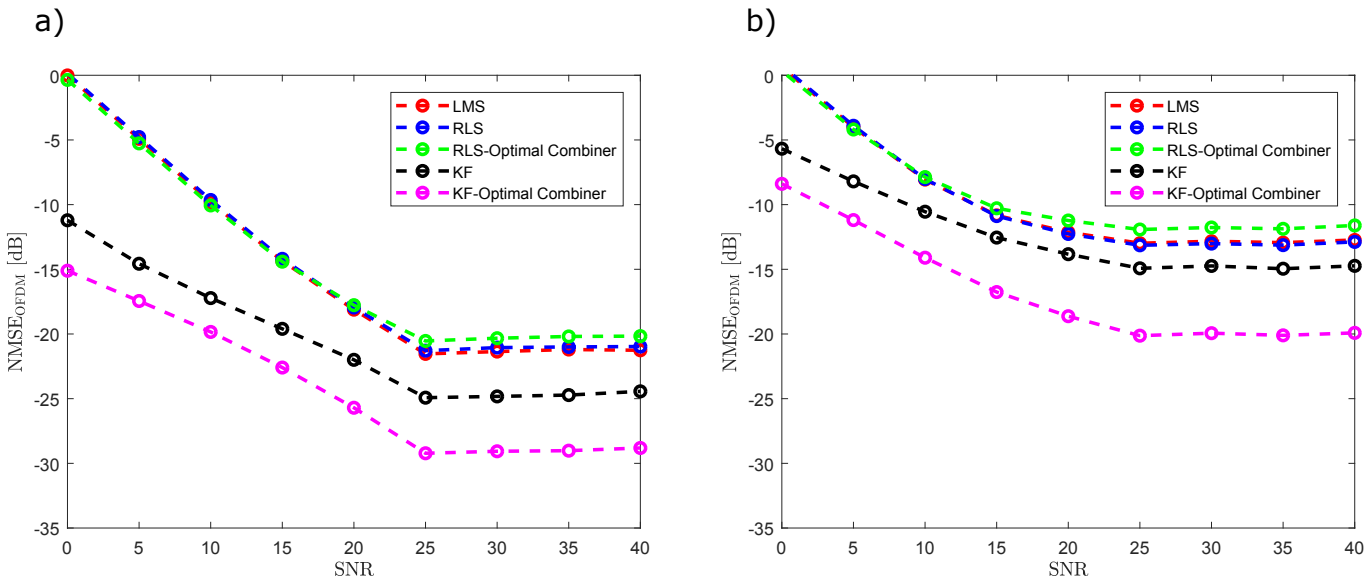

Figure 4.17: Estimation error vs SNR for different values of Doppler spread environments a) $\alpha = 0.1$ (rms Doppler spread per bounce) b) and $\alpha = 0.5$

4.9 Data-Aided Channel Estimation

In this section we study the Kalman filter estimation using data as pilots. For each OFDM symbol, the decoder generates the vector $L(\boldsymbol{d})$ which can be used to calculate the soft data $\tilde{\boldsymbol{d}}$ which is expected to biased, hence help in channel estimation process.

4.9.1 Soft-Symbols Kalman Filter

Modeling the time domain data $\boldsymbol{d}$ as [103]

$$\boldsymbol{d} = \widehat{\boldsymbol{d}} + \boldsymbol{\eta} \tag{4.82}$$

where $\widehat{\boldsymbol{d}}$ is time domain estimated data and $\boldsymbol{\eta}$ is Gaussian with $\mathbf{R}_{\boldsymbol{\eta}} = \sigma_d^2 \mathbf{I}$ — where the data symbols are assumed to be independent from each other. The data *and* pilots observation model is given by

$$\begin{aligned} y[i] &= \boldsymbol{f}[i](\boldsymbol{x} + \boldsymbol{d}) + n[i] \\ y[i] &= \boldsymbol{f}[i](\boldsymbol{x} + \widehat{\boldsymbol{d}}[i] + \boldsymbol{\eta}) + n[i] \\ &= \boldsymbol{f}[i](\boldsymbol{x} + \widehat{\boldsymbol{d}}[i]) + \boldsymbol{f}[i]\boldsymbol{\eta} + n[i] \\ &= \boldsymbol{f}[i](\boldsymbol{x} + \widehat{\boldsymbol{d}}[i]) + z[i] \end{aligned} \tag{4.83}$$

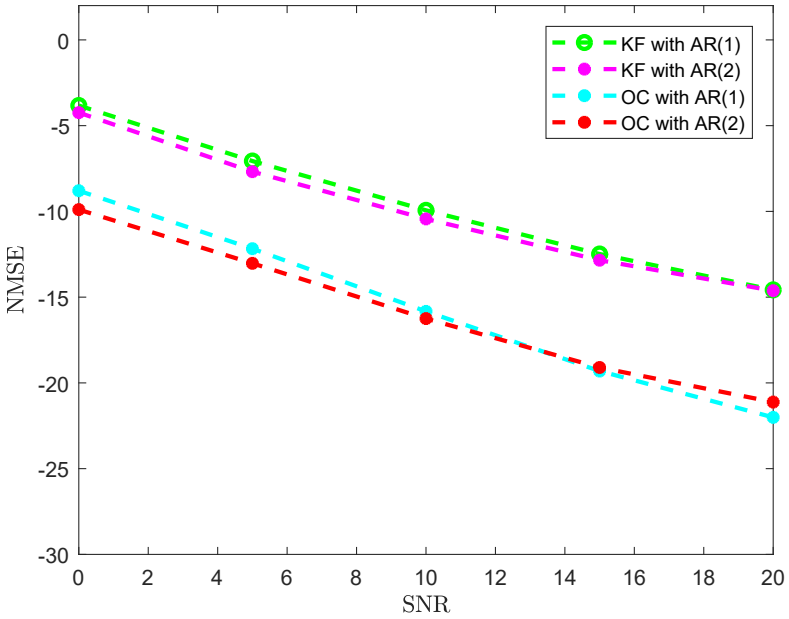

Figure 4.18: Estimation error vs SNR for KF with AR(1) and AR(2) with Doppler $\alpha = 0.25$ fixed for all paths. OC denoted optimal combining of Forward-backward filters.

and

$$z[i] = n[i] + \boldsymbol{f}[i]\boldsymbol{\eta} \tag{4.84}$$

where $z[i]$ is the total noise, with variance

$$\sigma_z^2 = \sigma_n^2 + \sigma_d^2 \mathrm{Tr}(\mathbf{R}_\mathrm{f}) \tag{4.85}$$

$$= \sigma_n^2 + \sigma_d^2 \sum_{k=1}^{N_{active}} P_k \tag{4.86}$$

where P_k is the power of the k^{th} discrete tap. The noise variance σ_z^2 depends on the uncertainty in the data $\boldsymbol{d}$ represented by σ_d^2. The Soft-Symbols *and* pilots channel estimator is

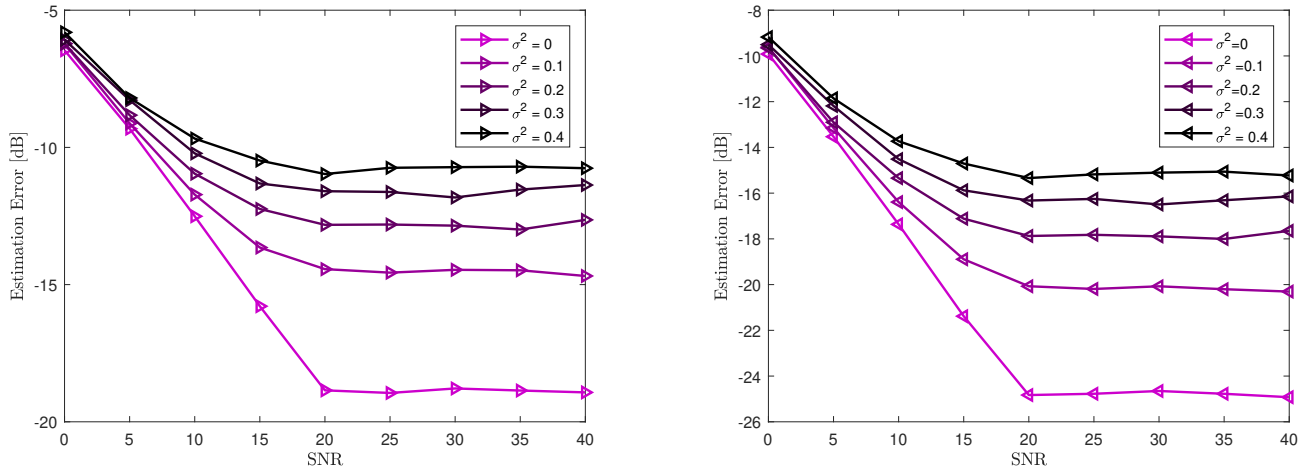

(a) (b)

Figure 4.19: (a) NMSE for Kalman Filter with Soft symbols, and (b) with optimal combining, with $\alpha = 0.1$.

given by

$$\sigma_z^2 = \sigma_n^2 + \sigma^2 \sum_{k=1}^{N_{active}} P_k \tag{4.87}$$

$$\sigma_e^2[i] = \sigma_z^2 + (\boldsymbol{x} + \widehat{\boldsymbol{d}})^H \mathbf{M}_f[i|i-1](\boldsymbol{x} + \widehat{\boldsymbol{d}}) \tag{4.88}$$

$$\boldsymbol{K}_f[i] = \frac{\mathbf{M}_f[i|i-1](\boldsymbol{x} + \widehat{\boldsymbol{d}})}{\sigma_e[i]^2} \tag{4.89}$$

$$e[i] = y[i] - \hat{\boldsymbol{f}}_f[i|i-1](\boldsymbol{x} + \widehat{\boldsymbol{d}}) \tag{4.90}$$

$$\hat{\boldsymbol{f}}_f[i|i] = \hat{\boldsymbol{f}}_f[i|i-1] + \boldsymbol{K}_f[i]e[i] \tag{4.91}$$

$$\hat{\boldsymbol{f}}_f[i|i+1] = \mathbf{A}^{(1)} \hat{\boldsymbol{f}}_f[i|i] \tag{4.92}$$

$$\mathbf{M}_f[i|i] = \mathbf{M}_f[i|i-1] - \frac{\mathbf{M}_f[i|i-1](\boldsymbol{x} + \tilde{\boldsymbol{d}})(\boldsymbol{x} + \tilde{\boldsymbol{d}})^H \mathbf{M}_f[i|i-1]}{\sigma_e^2[i]} \tag{4.93}$$

$$\mathbf{M}_f[i+1|i] = \mathbf{A}^{(1)H} \mathbf{M}_f[i|i] \mathbf{A}^{(1)} + \mathbf{Q}^1 \tag{4.94}$$

The Soft symbols Kalman filter and its combiner are tested using QPSK soft symbols as $\widehat{\boldsymbol{d}}$ and the pilots with the shift orthogonality property. Figures 4.19, 4.20 and 4.21 show the results for stretching factor $\alpha = 0.1$, 0.5 and 1.2 respectively. The algorithms are tested for range of noise variance σ_d^2, and as the noise increases the error of the estimate rises.

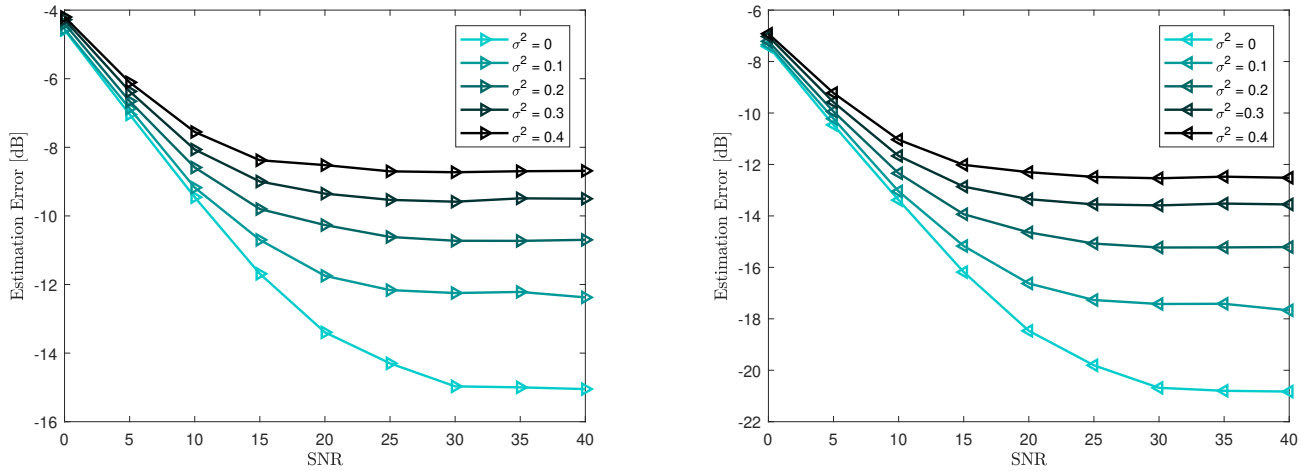

Figure 4.20: (a) NMSE for Kalman Filter with Soft symbols, and (b) with optimal combining, with $\alpha = 0.5$.

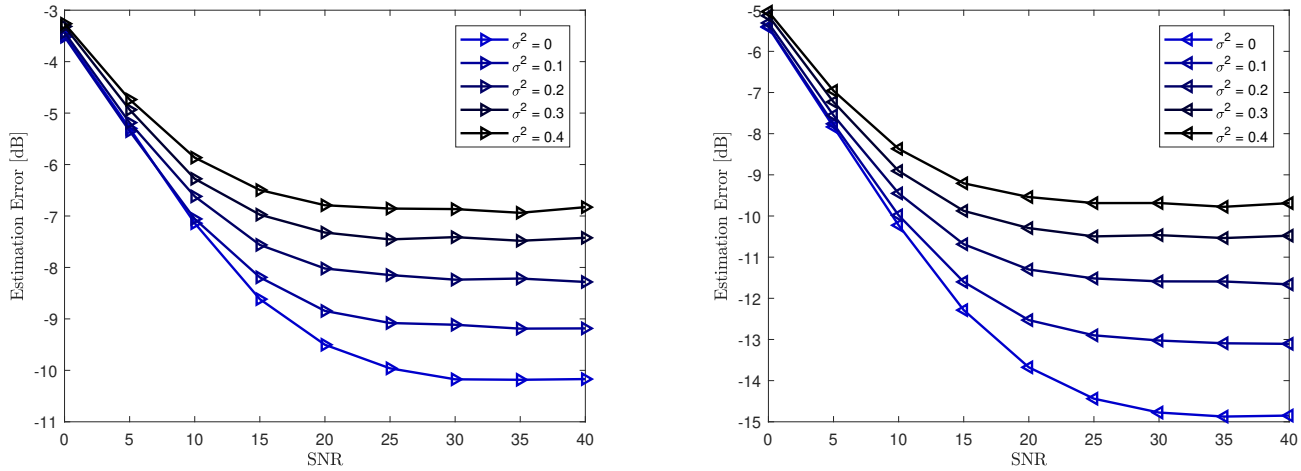

Figure 4.21: (a) NMSE for Kalman Filter with Soft symbols, and (b) with optimal combining, with $\alpha = 1.2$.

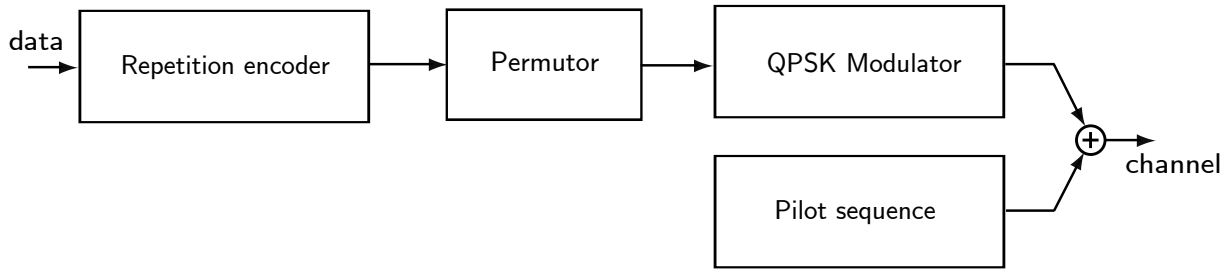

Figure 4.22: Transmitter diagram.

4.10 Iterative Receiver for OFDM and Channel Tracking Based on Soft Symbols

This section is dedicated to an application of the channel estimation and tracking technique presented in the previous sections to an OFDM system designed for underwater acoustic communications shown in Figure 4.7. For ease of reference we review the transmitter and receivers main functions.

Consider a system model depicted in Fig. 5.1 presented in [104]. A vector of data symbols $\boldsymbol{d}$ is encoded by an M-times repetition code (we choose $M = 4$ in our experiments) into a vector $\boldsymbol{d}'$ of length $2N$ which is permuted and mapped into a vector $\boldsymbol{D}$ composed of N quadrature phase-shift keying (QPSK) data symbols. The data signal is superimposed (added) in the time -domain to a known pilot sequence $\boldsymbol{p}$. The pilot sequence helps the channel estimator produce an initial channel estimate that can, in turn be used to initiate data decoding. Since we consider OFDM based transmission and reception, the vector $\boldsymbol{X} = \boldsymbol{D} + \boldsymbol{P}$ is transmitted over a vector channel described by

$$\boldsymbol{Y} = \mathbf{H}^{(f)}\boldsymbol{X} + \boldsymbol{\Psi}$$

where $\mathbf{H}^{(f)}$ is the $N \times N$ matrix of channel coefficients in frequency domain and $\boldsymbol{\Psi}$ is a vector of N iid circularly-symmetric Gaussian noise samples with power σ_n^2 in both complex dimensions combined (see (4.33)).

The repetition code in the system aids in the iterative interference cancellation of the ICI. A strong outer error correction code can be included to lower the resulting bit error-rate as desired at the cost of some loss on overall data rate. The iterative receiver diagram is given in Fig. 4.23. The received signal first arrives at the channel estimator and tracker that

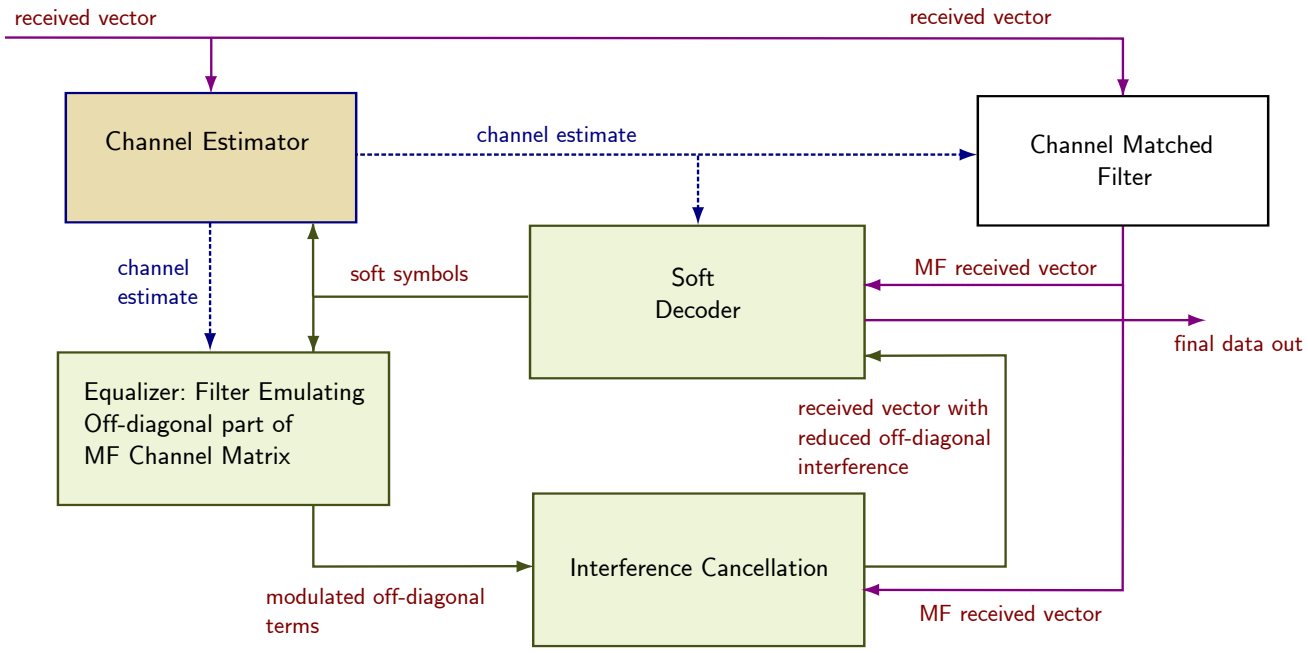

Figure 4.23: Receiver diagram.

performs estimation based on the known pilot sequence treating the unknown data signal as noise. The resulting channel estimate is transferred into the frequency domain $\widehat{\mathbf{H}}^{(f)}$ and is used to matched-filter the received signal as

$$\begin{aligned} \boldsymbol{r} &= \widehat{\mathbf{H}}^{(f)*}\boldsymbol{Y} = \widehat{\mathbf{H}}^{(f)*}\mathbf{H}^{(f)}\boldsymbol{X} + \widehat{\mathbf{H}}^{(f)*}\boldsymbol{\Psi} \\ &= \widehat{\mathbf{R}}\boldsymbol{X} + \boldsymbol{\phi} \\ &= \widehat{\mathbf{R}}\boldsymbol{D} + \widehat{\mathbf{R}}\boldsymbol{P} + \boldsymbol{\phi} \end{aligned}$$

where $\widehat{\mathbf{R}} = \widehat{\mathbf{H}}^{(f)*}\widehat{\mathbf{H}}^{(f)}$ and $\boldsymbol{\phi}$ is resulting colored noise. Since the ICI manifests itself in presence of the off-diagonal components in $\mathbf{H}^{(f)}$, the task of the matched filter is to consolidate the energy on the diagonal of the resulting matrix $\widehat{\mathbf{R}}$.

Before feeding the matched filtered output $\boldsymbol{r}$ to the soft demodulate-decoder, the pilot signal component $\widehat{\mathbf{H}}^{(f)*}\mathbf{H}^{(f)}\boldsymbol{P}$ is subtracted to produce

$$\widehat{\boldsymbol{r}} = \boldsymbol{r} - \widehat{\mathbf{H}}^{(f)*}\widehat{\mathbf{H}}^{(f)}\boldsymbol{P} + \boldsymbol{\phi} = \widehat{\mathbf{R}}\boldsymbol{D} + \boldsymbol{\phi}'$$

We also define the matrices of the diagonal and off-diagonal components of $\widehat{\mathbf{R}}$:

$$\widehat{\mathbf{R}}_{\text{diag}} = \text{diag}\left(\widehat{\mathbf{R}}\right); \qquad \widehat{\mathbf{R}}_{\text{off}} = \widehat{\mathbf{R}} - \widehat{\mathbf{R}}_{\text{diag}} \ .$$

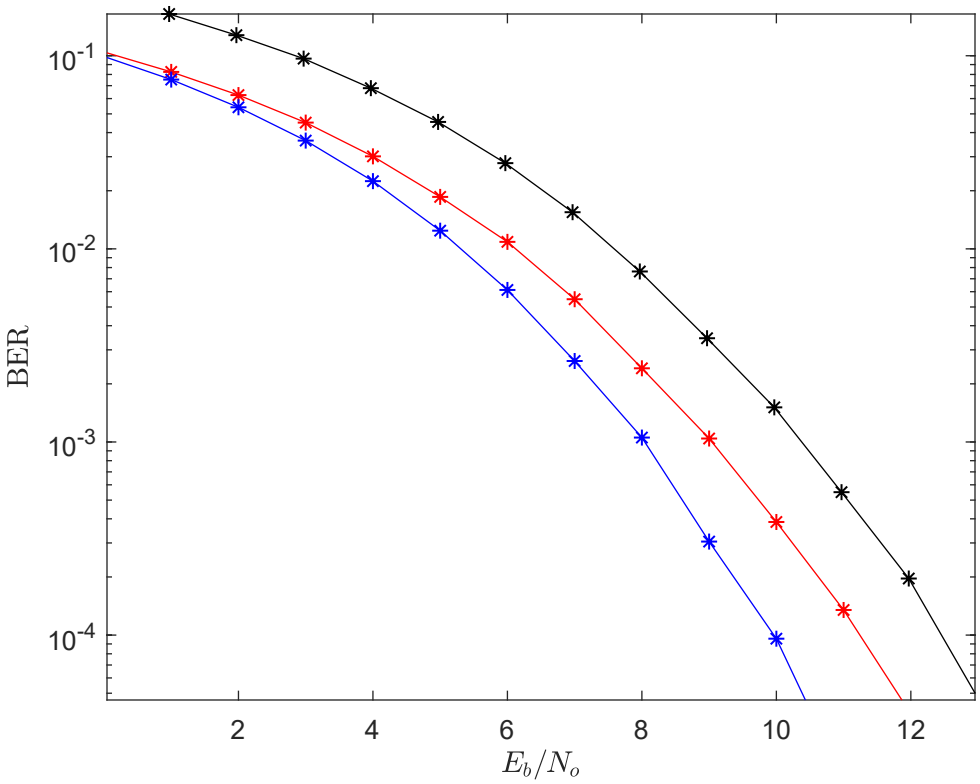

Figure 4.24: Bit Error Rate (BER) for the iterative receiver. The blue curve corresponds to the performance with perfect channel knowledge. The red curve corresponds to the (hypothetical system) performance where the channel estimation with 100% is performed first and then given to the iterative receiver. The black curves corresponds to the data-aided channel estimation with 15 iterations.

The soft decoder receives the signal $\widehat{\boldsymbol{r}}$ and produces a vector of soft-symbol estimates $\widehat{\boldsymbol{D}}^{(1)}$. It exploits the fact that each data bit participates in the data signal M times. It produces log-likelihood ratios (LLRs) of each replica of the received data bit and combines them in an optimal iterative decoding manner and uses a $\tanh(\cdot)$ function to produce soft-bit estimates. The channel estimate $\widehat{\mathbf{H}}^{(f)*}$ is also utilized by the soft decoder for LLR normalization.

In the sequel every iteration i starts from a new channel estimate obtained by the channel estimator and tracker from the received observation signal $\boldsymbol{Y}$ based on the known pilot sequence and the soft data symbols $\widehat{\boldsymbol{D}}^{(i-1)}$ supplied by the soft decoder. Then the interference cancellation unit produces the cancelled signal

$$\boldsymbol{r}^{(i)} = \widehat{\mathbf{H}}^{(f)(i)*}\boldsymbol{Y} - \widehat{\mathbf{R}}_{\text{off}}^{(i)}\widehat{\boldsymbol{D}}^{(i-1)} - \widehat{\mathbf{H}}^{(f),(i)*}\widehat{\mathbf{H}}^{(f),(i)}\boldsymbol{P}$$

with pilot removed. The signal $\boldsymbol{r}^{(i)}$ is forwarded to the soft decoder to produce the soft

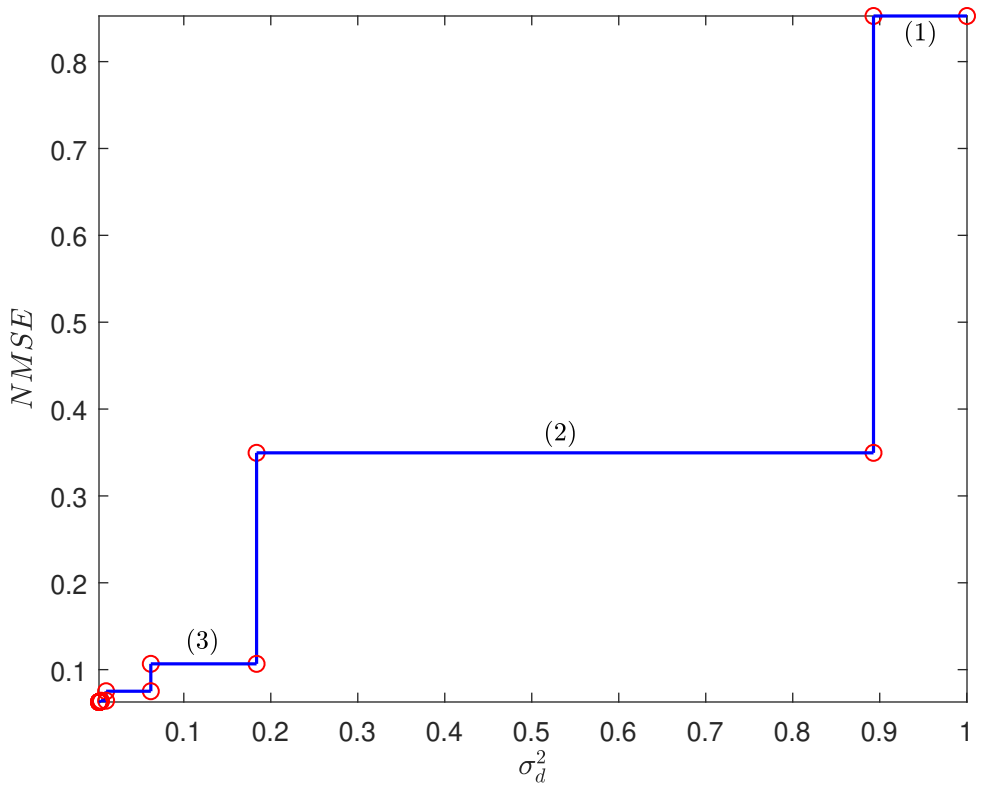

Figure 4.25: Variance Transfer Chart (VTC) shows the progressive reduction of the variance of soft symbols with the iterations. At the first iteration, the estimator relies exclusively on the pilot sequence to produce the channel estimate. The number of iterations is $I = 15$, and we can see that the soft symbols quickly become known and are used by the estimator together with the pilots.

symbols $\widehat{\boldsymbol{D}}^{(i)}$, and so on.

The progressive reduction of the soft symbol variance throughout the iterations is shown in Fig. 4.25. The normalized MSE of the channel estimator is given as a function of the soft-bit variance. The blue line shows change in the values as iteration progress. We can see that at the very beginning the estimation is noisy while the soft bits are completely unknown. At the end the estimation is very precise and the soft bits are decoded with high confidence.

The bit error rate (BER) performance curves are plotted in Fig. 4.24 as a function of the system SNR per bit E_b/N_0. The iterative receiver with perfect channel knowledge corresponds to the benchmark BER given by the blue curve. The red curve represents the BER for a hypothetical case when a channel estimation with 100% pilot density is performed

outside of the iterative received and the receiver is provided with the estimated channel knowledge. Finally the black curve corresponds to the actual bit error-rate performance of the iterative receiver with the iterative channel estimation. The pilot sequence power is chosen to be 0.25 of the data sequence power is accounted for in the E_b/N_0 computation. The iterative receiver performance with the estimator is just about 2dB away from the perfect channel knowledge case and about 3dB away from the AWGN (without time or frequency selectivity) case.

4.11 Conclusion

In this chapter we present a channel estimation technique for underwater acoustic channel. The method tailored to OFDM transmission systems and is based on utilizing forward and backward Kalman-filter trackers and combining of the estimates for each sample within an OFDM symbol. We demonstrate that the estimator can provide quality estimates even for realistic channels with long, dense power delay profiles and significant Doppler spreads. The estimator is a part of the iterative receiver used for decoding of data transmitted via OFDM signalling and shown it is capable to start the iterative process providing initial channel estimates using a low-power pilot. As the decoder learns the data throughout the iteration the estimator can improve the quality of the estimates benefiting from soft estimates of the OFDM symbol data and eventually converges to the interference free state.

Chapter 5

Unsourced Random Access over Fading Channels via Data Repetition, Permutation, and Scrambling

5.1 Abstract

We focus on an unsourced random access (URA) system for communication over fading channels where the payload of each packet is encoded for error-correction, repeated, permuted, and scrambled. Each packet is also equipped with a preamble that is used for channel estimation and encodes permutation and scrambling sequences utilized for payload encoding. We propose an algorithm to resolve multiple-access preamble transmission, based on the approximate message-passing (AMP), that is capable to support high numbers of active users and achieve low probabilities of miss-detection. We also develop a parallel interference cancellation technique for payload reception that iteratively refines the channel estimates and attempts to minimize the mean squared error (MSE) of the users' data via selective error-correction decoding. Finally we derive a detailed system performance analysis that closely matches the obtained numerical results. We demonstrate that the presented system can more than double the number of active users, supported by the state-of-the-art systems. Large gains in terms of the minimal required signal-to-noise ratios (SNR)s are also demonstrated for a wide range of active user numbers.

5.2 Introduction

The concept of random access received a lot of attention in multi-user communications since the design of the ALOHA system in 1970s [105]. A system where multiple users access a common transmission media on demand at random times (grant free) has proven to be important for a large variety of applications including cellular, ad hoc, and sensor networks. The random access functionality is even more important now, when the methodology and philosophy of the fifth generation of cellular systems (5G) and beyond (B5G) focus on incorporating new functionalities such as the Internet of things (IoT), machine-to-machine

(M2M) and others.

The unsourced random access is a novel random access paradigm [12] that targets short packet random access communication in wireless systems. A very large number of potential users is considered, while only a smaller subset of all potential users is active at any given time. The users communicate in a grant-free fashion without pre-allocation of time, space, or bandwidth resources. Due to a very large size of the overall user pool it is assumed that the receiver cannot be tailored to distinguish users based on their identities (IDs). Instead, the users utilize a common codebook to transmit their data. Hence, the receiver may not be able to identify the transmitters where the received data packets originated. Therefore, the URA concept is especially suitable for applications where it is important to deliver the data itself rather than trace back the origin of the data. In addition, the reliability measure defined for URA systems is the average per-user probability of error and error-free reception of all packets is not targeted.

A number of URA systems have been proposed, starting from a few approaches examined in [12, 13]. The main focus for most of the existing research is on the Gaussian multiple-access channel and the resolution of multi-user interference in the unsourced setting, rather than dealing with the channel impairments. A number of methods based on the ideas that stem from the compressed sensing (CS) domain were proposed in [13, 14, 15, 16, 17]. Some methods rely on the T-fold and irregular slotted ALOHA [18] where each packet time slot is further subdivided into sub-slots that may be accessed randomly by different active users [19, 20, 21] to transmit their data. Another cohort of methods uses a blend of CS-encoded preamble and a data payload [22, 23, 24, 19] encoded for multi-user access. It has been also shown [106] that for lower numbers of active users the preamble may be omitted [106] to increase the system's efficiency.

When URA is applied to a more general channel, the identification of active users and message decoding are further complicated by the necessity to perform channel estimation. Some packets may be lost due to poor channel conditions, and the inability of the receiver to recover these further complicates the decoding of the remaining packets. URA over Rayleigh channel is considered in [20, 21, 107, 108, 109, 110]. In [20, 21] it is performed via data-aided estimation in conjunction with T-fold ALOHA and parallel interference cancellation (PIC) or serial interference cancellation (SIC) processing. Multiple antennas in a massive multiple-input multiple-output (MIMO) setup aid channel diversity and facilitate decoding

and channel estimation for URA in [107, 108, 109, 110].

The methods proposed in [20, 21] prescribe each user to randomly pick a sub-slot within a frame dedicated to packet transmission and transmit a short block of data encoded by a low-density parity-check (LDPC) or polar code. This results in the T-fold ALOHA approach where T is the maximum number of blocks that can be simultaneously received and successfully decoded on a single sub-slot. The decoding capability T is related to the strength of the underlying error-correction code (ECC). The channel estimation and data decoding are preformed jointly on the entire system graph [20]. While the methods of [20, 21] are successful for small and medium numbers of active users, high numbers of active users, that lead to increased numbers of packet collisions, overwhelm the decoding capability of the system.

In this work we utilize packets with preamble/payload separation as suggested in [22, 23, 24, 19], build on the concept of a URA system [111], and focus on construction of transmission and reception algorithms for URA over fading channels, specifically the single-antenna block-fading Rayleigh channel. The payload data is encoded via an error-correction code and undergoes repetition, permutation, and scrambling to create a non-orthogonal multiple-access transmission. The preamble is used to communicate the pairs of permutation and signature sequences, selected by the active users to permute and scramble their payload data. The receiver recovers the signature and permutation pairs from the preambles received on the preamble multiple-access channel and uses them for decoding of the payloads received on the payload multiple-access channel.

The preamble is utilized for an initial channel estimation that starts the data-aided channel estimation process operating within the payload decoder. The preamble decoder has to be powerful enough to support high numbers of active users that inevitably lead to multiple user collisions, i.e. situations when several users pick the same pair of signature and permutation for their payload encoding. We demonstrate that the balance between the numbers of misses and false alarms produced by the preamble decoder has to be tipped towards lower numbers of misses. Moderate levels of false alarms can then be overcome by the iterative multiple-user payload decoder that alternates between the estimation of channel values and data bits, and cancellation of the multi-user interference. Our contributions are as follows:

- We propose a preamble detection algorithm, based on the AMP principle, that combines features of channel estimation, interference suppression via adaptive thresholding, the overall power constraint, and a tuned complex approximate message-passing (CAMP) [112]. We demonstrate that the proposed algorithm outperforms its existing counterparts and is capable to support the presented URA system in highly overloaded user regimes.

- We develop an iterative multi-user detection and decoding algorithm with channel estimation, a selective decoding and thresholding of the detected user packets based on their estimated SNR, and removal of successfully decoded packets.

- We present a detailed performance analysis of the payload decoder and the entire URA system that takes into account the error-correction code, probability of miss, and user collision distribution. The results of the analysis can closely predict the results achievable by simulations.

The presented URA system significantly outperforms the existing methods in terms of supported numbers of active users. It also requires less SNR to guarantee a given level of the per-user probability of error. We demonstrate that very high rate systematic codes (such as Hamming code and double error-correcting BCH [113, 114] code) with low-complexity encoding allow for successful system operation over a wide spectrum of active user loads. Finally we demonstrate that the system is scalable and can operate successfully on different slots sizes.

The chapter is organized as follows. Section 5.3 presents the system model, describes the packet structure, channel, and the decoding algorithms utilized at the receiver. Section 5.4 presents the performance analysis derived to track the evolution of the noise-and-interference power (NIP) throughout the decoding iterations. Section 5.5 presents the numerical simulation results and Section 5.6 concludes the chapter.

5.3 System Model

We consider a URA scenario with the overall pool of K_{tot} potential users where only K_{a} users out of K_{tot} are active, $K_{\text{a}} \ll K_{\text{tot}}$. The system is slotted and the active users start transmitting their packets at the beginning of time slots (frames). The length of each frame

equals N_{t} channel uses. The information message of the kth active user, $k = 1, 2, \cdots, K_{\mathrm{a}}$ is a binary vector $\boldsymbol{u}^k$ of length B that is mapped by the transmitter into a data message (packet) $\boldsymbol{x}^k = \boldsymbol{x}^k(\boldsymbol{u}^k)$ of length N_t. The power of each packet is constrained to P i.e. $||\boldsymbol{x}^k||^2 \leq N_{\mathrm{t}}P$, $k = 1, 2, \cdots, K_{\mathrm{a}}$. We focus on the case when each user's transmitter as well as the common receiver are all equipped with single antennas. Fading channel is considered and the received signal is given by

$$\boldsymbol{y} = \sum_{k=1}^{K_a} \mathbf{H}_k \boldsymbol{x}^k(\boldsymbol{u}^k) + \boldsymbol{z}, \tag{5.1}$$

where $\mathbf{z} \overset{\text{i.i.d.}}{\sim} \mathcal{CN}(0, N_0\mathbf{I}_{N_{\mathrm{t}}})$ is the complex additive white Gaussian noise (AWGN) vector and the channel coefficient matrix equals $\mathbf{H}_k = \mathrm{diag}(\boldsymbol{h}_k)$, where $\boldsymbol{h}_k$ is the channel coefficient vector of the kth user. The channel coefficient vector is independent of $\boldsymbol{x}^k$ and $\boldsymbol{z}$. In this work, block-fading Rayleigh channel is considered, where the channel coefficient of each user is constant during the entire transmission frame, i.e. $\mathbf{H}_k = h_k\mathbf{I}_{N_{\mathrm{t}}}$, where $h_k \overset{\text{i.i.d.}}{\sim} \mathcal{CN}(0, 1)$. We assume that the channel coefficients are unknown to both the transmitter and receiver (no-CSI assumption). In the remainder of the chapter we will use the short notation $\boldsymbol{x}^k$ instead of $\boldsymbol{x}^k(\boldsymbol{u}^k)$.

To evaluate the performance of a URA scheme, the per-user probability of error (PUPE) is defined in [12] as

$$P_e = \frac{1}{K_{\mathrm{a}}} \sum_{j=1}^{K_{\mathrm{a}}} \Pr[E_j], \tag{5.2}$$

where $E_j \triangleq \{\boldsymbol{u}^j \notin \phi(\boldsymbol{y})\} \cup \{\boldsymbol{u}^j = \boldsymbol{u}^i, i \neq j\}$ and $\phi(\boldsymbol{y})$ is the list of messages decoded by the receiver based on the received signal $\boldsymbol{y}$. URA algorithms are often compared based on the minimum SNR per information bit (E_{b}/N_0) they require in order to achieve a certain level of PUPE.

5.3.1 Packet Structure and Transmitter Model

We consider the concept of splitting a packet into a preamble and a payload, proposed in [22, 23] in context of URA, and follow the approach of [111] where data permutation and signature sequences were used in the payload encoding. We then develop the signal processing algorithms required for the receiver operation, given in Sections 5.3.2 and 5.3.3, to establish URA over block Rayleigh-fading channels.

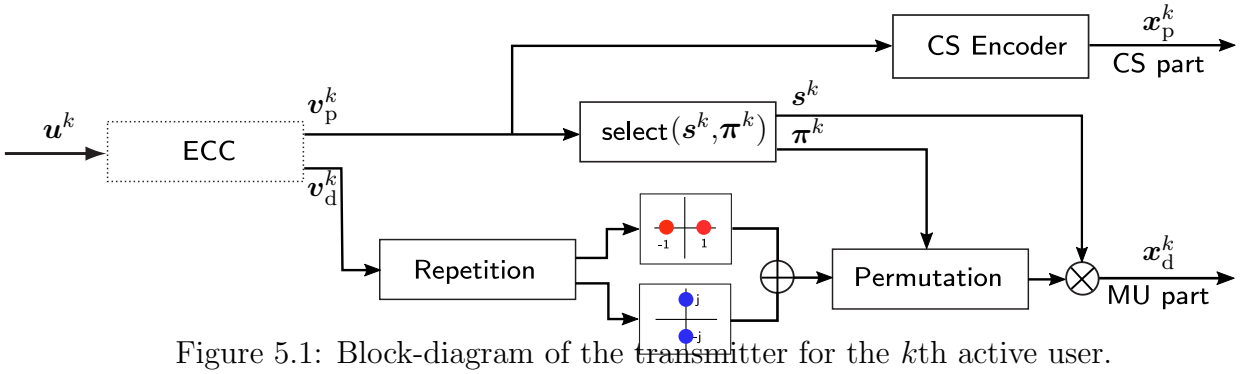

Figure 5.1: Block-diagram of the transmitter for the kth active user.

The transmitter of the kth active user is depicted in Figure 5.1. The B-bit information vector $\boldsymbol{u}^k$ of the kth active user, $k = 1, 2, \cdots, K_{\mathrm{a}}$, is first encoded by a binary (n, B) error-correction code of rate $R = B/n$. The encoded vector $\boldsymbol{v}^k$ is split into two parts $\boldsymbol{v}^k = [\boldsymbol{v}_{\mathrm{p}}^k, \boldsymbol{v}_{\mathrm{d}}^k]$. The sequence $\boldsymbol{v}_{\mathrm{p}}^k$ of length B_{p} is used to encode the preamble which we call the *CS part* of the packet since it is encoded and decoded via compressed-sensing. The sequence $\boldsymbol{v}_{\mathrm{d}}^k$ of length $B_{\mathrm{d}} = n - B_{\mathrm{p}}$ is used to encode the payload $\boldsymbol{x}_{\mathrm{d}}^k$ which we will call the *MU part* of the packet since it will be decoded via a multi-user detector (MUD). Thus, the message (packet) of the kth user is $\boldsymbol{x}^k = [\boldsymbol{x}_{\mathrm{p}}^k, \boldsymbol{x}_{\mathrm{d}}^k]$ and the lengths of the CS part and MU part of the message equal to N_{p} and N_{d} respectively where $N_{\mathrm{t}} = N_{\mathrm{p}} + N_{\mathrm{d}}$.

To encode the CS part, the B_{p}-bit sequence $\boldsymbol{v}_{\mathrm{p}}^k$ is converted to a decimal number $\nu^k \in [0, 2^{B_{\mathrm{p}}} - 1]$ and mapped into a sequence $\boldsymbol{x}_{\mathrm{p}}^k = \boldsymbol{a}_{\nu^k}$ of length N_{p}. The sequence $\boldsymbol{a}_{\nu^k}$ is a column in an $N_{\mathrm{p}} \times 2^{B_{\mathrm{p}}}$ matrix $\mathbf{A}$ composed of iid complex Gaussian $\mathcal{CN}(0, 1)$ entries.

To encode the MU part, kth active user selects a pair of signature and permutation sequences $(\boldsymbol{s}^k, \boldsymbol{\pi}^k)$ uniformly at random from a set of $2^{B_{\mathrm{p}}}$ of such pairs based on ν^k. Each signature sequence is constructed from iid unitary complex numbers with uniform random phase. The permutation sequences are selected uniformly at random from a set of all permutations of length $B_{\mathrm{d}}M/2$. At first, the bit sequence $\boldsymbol{v}_{\mathrm{d}}^k$ is repeated M times to generate a vector of length $B_{\mathrm{d}}M$. The repeated sequence is mapped to a sequence of QPSK symbols of length $B_{\mathrm{d}}M/2$ as shown in Fig. 5.1. The complex modulated signal is then permuted using $\boldsymbol{\pi}^k$ and multiplied symbol by symbol by the signature sequence $\boldsymbol{s}^k$ (scrambled) to produce the encoded MU part $\boldsymbol{x}_{\mathrm{d}}^k$.

As we will see later, the selection of the ECC depends on the URA operational regime. If the number of active users K_{a} is low, it is possible to apply a stronger code with lower rate (larger n) in order to reduce the required operational SNR. For highly overloaded systems

with large numbers of active users high-rate codes are more beneficial, since they allow to use higher repetition factors M, essential for successful convergence of the multi-user detection. The task of the code is two-fold. First of all it reduces the number of errors at the output of the URA receiver to guarantee the required level of PUPE. The second role the code plays is to help the multi-user detector working on the MU parts of the packets to converge to the "single-user" performance and aid the channel estimation within the iterative MUD process.

5.3.2 User Detection and Channel Estimation via AMP

The composite received signal for the CS parts of the users' packets is given by

$$\boldsymbol{y}_{\mathrm{p}} \;=\; \sum_{k=1}^{K_{\mathrm{a}}} h_k \boldsymbol{x}_{\mathrm{p}}^{k} + \boldsymbol{z}_{\mathrm{p}} = \sum_{k=1}^{K_{\mathrm{a}}} h_k \boldsymbol{a}_{\nu^k} + \boldsymbol{z}_{\mathrm{p}} = \mathbf{A}\mathfrak{h} + \boldsymbol{z}_{\mathrm{p}}, \tag{5.3}$$

where $\mathfrak{h}$ is a sparse $(2^{B_{\mathrm{p}}} \times 1)$ vector of user activity and channel coefficients, and $\boldsymbol{z}_{\mathrm{p}}$ is the complex AWGN $\mathcal{CN}(0, N_0\mathbf{I}_{N_{\mathrm{p}}})$. All entries of $\mathfrak{h}$ are zeros except for $\mathfrak{h}_{\nu^k}$ for $k = 1, 2, \cdots, K_{\mathrm{a}}$. Typically $\mathfrak{h}_{\nu^k} = h_k$, however, if two active users k_1 and k_2 select the same $\nu^{k_1} = \nu^{k_2}$ then $\mathfrak{h}_{\nu^{k_1}} = \mathfrak{h}_{\nu^{k_2}} = h_{k_1} + h_{k_2}$ (user collision). For the case of Gaussian only channel $h_k \in \{0, 1\}$ indicating the users status of active or dormant with probabilities p_0 and p_1 respectively. In case of collision, where tow or more users select the same signature sequence then $h_k > 1$, and pair collision $k_k = 2$ with probability p_2 . We treat the activity-collision detection first.

AMP Algorithms for Detection of Active Users and Collisions events

The power based activity-detection only AMP algorithm is presented in [115] [116] has the following form

$$\boldsymbol{z}^{l} = \boldsymbol{y}_{\mathrm{p}} - \mathbf{A}\widetilde{\mathfrak{h}}_{\mathrm{p}}^{l} + \boldsymbol{z}^{l-1}\left(P - ||\widetilde{\mathfrak{h}}_{\mathrm{p}}^{l}||^2\right) N_{\mathrm{p}}^{-1}\tau_{l-1}^{-2} \tag{5.4}$$

$$\widetilde{\mathfrak{h}}_{\mathrm{p}}^{l+1} = \sqrt{P_1}\left(1 + \frac{p_0}{1-p_0} e^{\sqrt{P_1}(0.5\sqrt{P_1} - \mathbf{A}^{\mathrm{T}}\boldsymbol{z}^{l} + \widetilde{\mathfrak{h}}_{\mathrm{p}}^{l})\tau_l^{-2}}\right)^{-1} \tag{5.5}$$

where $\tau_l^2 = ||\boldsymbol{z}^l||^2/N_{\mathrm{p}}$, $P = K_{\mathrm{a}}P_1$ and p_0 is the probability that an element of $\tilde{\boldsymbol{v}}_{\mathrm{p}}$ equals 0 (user inactivity rate). The recursion is initialized with $\boldsymbol{z}^0 = \mathbf{0}$, $\tilde{\boldsymbol{v}}_{\mathrm{p}}^0 = \mathbf{0}$ and l is the iteration index. The above algorithm assumes no collision event is present, and all users signatures are unique. As the number of users increase and subsequently probability of pair-collision (see Figure 5.6) the above AMP algorithm introduces additional missed detection and false alarms

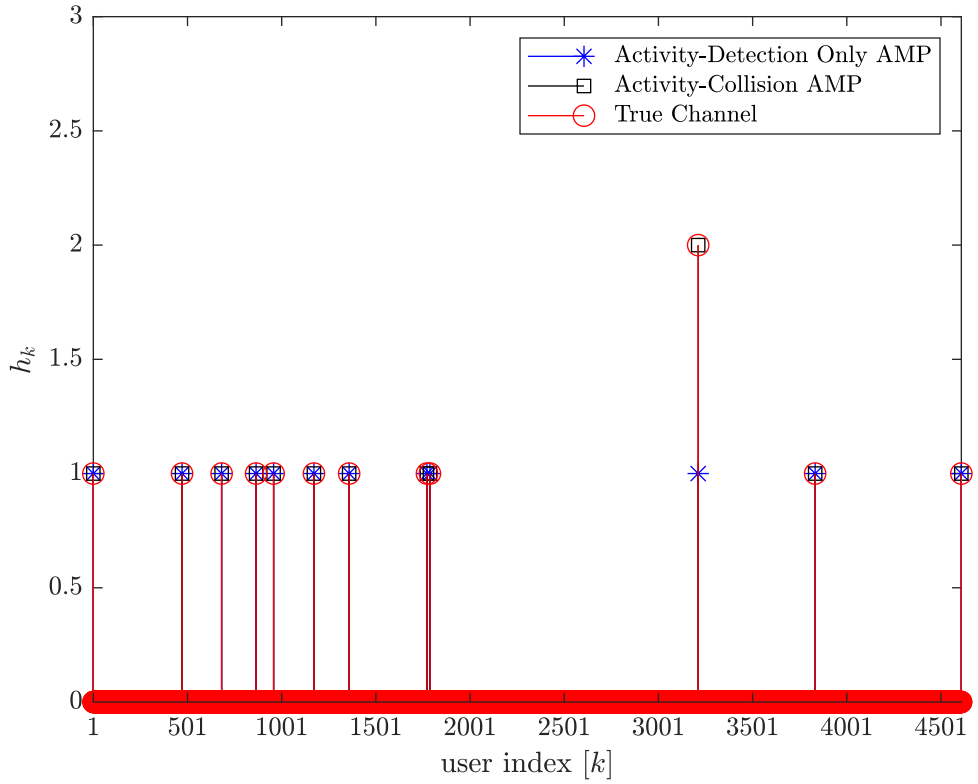

Figure 5.2: shows the estimates of $\mathfrak{h}$ produced using activity-detection (5.4) only and activity-collision AMP (5.7).

as it tries to gauge the estimate to have power P. Moreover, the MUD detector benefits form the knowledge of collision and enables the design of collision resolution techniques. By acknowledging the pair collision events the AMP algorithm can simultaneously detects activity and collision patterns. The modified algorithm first implements the cancellation step shown in equation (5.4), and then calculate the initial channel estimate

$$\boldsymbol{r}^{(l)} = \widehat{\boldsymbol{v}}^{(l)} + \mathbf{A}^T \boldsymbol{z}^{(l)}, \tag{5.6}$$

to finally estimate the activity-collision detection pattern

$$\widehat{\boldsymbol{v}}^{(l+1)} = \frac{p_1 e^{\frac{-(\boldsymbol{r}^{(l)}-1)^2}{2\tau_l^2}} + 2p_2 e^{\frac{-(\boldsymbol{r}^{(l)}-2)^2}{2\tau_l^2}}}{p_0 e^{\frac{-\boldsymbol{r}^{(l)2}}{2\tau_l^2}} + p_1 e^{\frac{-(\boldsymbol{r}^{(l)}-1)^2}{2\tau_l^2}} + p_2 e^{\frac{-(\boldsymbol{r}^{(l)}-2)^2}{2\tau_l^2}}}. \tag{5.7}$$

Figure 5.2 compares between activity-only and collision-aware AMP algorithms, where the AMP in 5.4 reduces collision to activity event. The following table summarizes the effects of

this reduction on missed detection and false alarms rates, where missed detection rate are consistently lower for collision aware algorithm.

	Collision-Aware		Collision-Blind	
K_{a}	Missed Detection	False Alarms	Missed Detection	False Alarms
400	4/100	3/100	6/100	2/100
500	1/100	0	3/100	0
600	0	2/100	3/100	1/100

Table 5.1: shows missed detection and false alarms for the collision aware and blind AMP respectively. Number of channel uses is 4000 for $K_{\mathrm{a}} = [400, 500]$, and 5000 for $K_{\mathrm{a}} = 600$.

Complex AMP Algorithms for Detection of Active Users and Channel Estimation

The setting in equation (5.3) is a typical compressed sensing problem, where the task is to estimate a long sparse vector $\mathfrak{h}$ based on a much shorter vector of observations $\boldsymbol{y}_{\mathrm{p}}$. Numerous methods to approach this problem exist such as orthogonal matching pursuit (OMP) [117], l_1-regularized least squares (LASSO) [118], non-negative least squares (NNLS) [119] and others. While many algorithms are designed for the case of real-valued measurements and unknowns, only a subset of these is applicable to the more challenging case of complex measurements, unknowns and sensing matrices. Joint channel estimation and user detection algorithms were proposed in [107, 109] for the case of massive MIMO receiver where they rely on the multiple antenna diversity.

A complex version of one of the most successful algorithms, the AMP [120] (which was used to approach the asymptotic information-theoretic CS limit in [121]) has been developed in [112]. The complex AMP (CAMP) presented in [112] is a method to study asymptotic behavior of the complex LASSO. The following recursive equations describe CAMP algorithm applied to (5.3), where l is the iteration index and $\widehat{\mathfrak{h}}_j^l$ is the estimated vector

$$\widehat{\mathfrak{h}}_j^{l+1} = \eta(\widehat{\mathfrak{h}}_j^l + \sum_b A_{bj}^* z_b^l; \tau_l) \quad j = 1, 2, \cdots, 2^{B_{\mathrm{p}}} \tag{5.8}$$

$$\begin{aligned} z_a^{l+1} = y_a &- \sum_j A_{aj} \widehat{\mathfrak{h}}_j^{l+1} \\ &- \sum_j A_{aj} \left(\frac{\delta \eta^R}{\delta \mathfrak{h}} (\widehat{\mathfrak{h}}_j^l + \sum_b A_{bj}^* z_b^l) \right) \mathrm{Re}(A_{aj}^* z_a^l) - \sum_j A_{aj} \left(\frac{\delta \eta^R}{\delta \mathfrak{h}} (\widehat{\mathfrak{h}}_j^l + \sum_b A_{bj}^* z_b^l) \right) \mathrm{Im}(A_{aj}^* z_a^l) \\ &- i \sum_j A_{aj} \left(\frac{\delta \eta^I}{\delta \mathfrak{h}} (\widehat{\mathfrak{h}}_j^l + \sum_b A_{bj}^* z_b^l) \right) \mathrm{Re}(A_{aj}^* z_a^l) - i \sum_j A_{aj} \left(\frac{\delta \eta^I}{\delta \mathfrak{h}} (\widehat{\mathfrak{h}}_j^l + \sum_b A_{bj}^* z_b^l) \right) \mathrm{Im}(A_{aj}^* z_a^l), \\ &a = 1, 2, \cdots, N_{\mathrm{p}} \quad l = 0, 1, \ldots \end{aligned} \tag{5.9}$$

The initial conditions are given by $\widehat{\mathfrak{h}}^0 = \mathbf{0}$ and $\boldsymbol{z}^0 = \mathbf{0}$. The complex soft thresholding function

$$\eta(u+iv;\tau_l) = \left(u+iv-\frac{\tau_l(u+iv)}{\epsilon+\sqrt{u^2+v^2}}\right)\mathbf{1}(u^2+v^2>\tau_l^2)$$

is applied element-wise, and ϵ is a small positive number used to preserve numerical stability. The function suppresses small entries in the estimated user activity and channel coefficient vector. The entries with the amplitude that falls below the threshold τ_l are set to zero since they are likely caused by the noise. At every iteration the algorithm performs thresholding with $\eta(\cdot)$ to produce a new estimate $\widehat{\mathfrak{h}}^{l+1}$ of $\mathfrak{h}$ and computes the residual noise and interference $\boldsymbol{z_a}^{l+1}$ that results from cancellation of the interference caused by $\widehat{\mathfrak{h}}^{l+1}$ and the correction term (the last four terms in (5.9)). The CAMP algorithm is agnostic to the distribution of the non-zero entries of $\mathfrak{h}$ and works for a wide range of distributions. An enhanced version of CAMP, called the tuned CAMP, which we will denote by τCAMP, is presented in [122]. At every iteration of τCAMP the optimal threshold value τ_l is selected, that minimizes the square error function $\mathbb{E}_u\|\eta(\mathfrak{h}+\sigma u;\tau)-\mathfrak{h}\|^2$ for a given sparse channel $\mathfrak{h}$, where $u\sim\mathcal{N}(0,1)$ and σ is the noise and interference level.

Based on the conducted experiments we found that τCAMP significantly outperforms the original CAMP for the problem of (5.3). However, when either CAMP or τCAMP is applied to a system with a large number of active users (overloaded system) high levels of misses are produced and that results in high PUPE of the overall URA system. As we will see later, the number of misses is the key parameter of the algorithm as long as URA application is concerned. Moderate levels of false alarms cause slight increase of interference within the MUD operating on the MU parts of the packets. Similarly, the quality of the channel estimates provided by the AMP algorithm for the active users does not have to be very high, since these estimates will be refined multiple times at the MUD stage. Therefore, in the next section we propose a new algorithm that meets the needs of the designed URA system.

Proposed Phase Estimation and Thresholding AMP (PET-AMP) Algorithm

The new algorithm is developed based on AMP framework [120]. We start with outlining the steps of the algorithm performed at every iteration l and then explain the purpose of

each step. The algorithm is given by

$$\boldsymbol{z}_{\mathrm{p}}^{l} = \boldsymbol{y}_{\mathrm{p}} - \mathbf{A}\widehat{\mathfrak{h}}^{l} + \frac{\boldsymbol{z}_{\mathrm{p}}^{l-1}}{\tau_{l-1}^{2}}\left(\frac{P_{\mathrm{h}} - ||\widehat{\mathfrak{h}}^{l}||^{2}}{N_{\mathrm{p}}}\right), \tag{5.10}$$

$$\mathfrak{r}^{l} = \widehat{\mathfrak{h}}^{l} + \mathbf{A}^{*}\boldsymbol{z}_{\mathrm{p}}^{l}, \tag{5.11}$$

$$|\tilde{\mathfrak{h}}_{j}| = \frac{p_1 \int_0^\infty a p(a)\rho(\mathfrak{r}_j^l|a,\tau_l)da}{p_0\rho(\mathfrak{r}_j^l|a=0,\tau_l) + p_1\int_0^\infty p(a)\rho(\mathfrak{r}_j^l|a,\tau_l)da} \quad j=1,\cdots,2^{B_{\mathrm{p}}} \tag{5.12}$$

$$\arg(\tilde{\mathfrak{h}}_{j}) = \arg(\mathfrak{r}_{j}^{l}) \quad j=1,2,\cdots,2^{B_{\mathrm{p}}} \tag{5.13}$$

$$\tau_{l}^{2} = \frac{||\boldsymbol{z}_{\mathrm{p}}^{l}||^{2}}{N_{\mathrm{p}}}, \tag{5.14}$$

$$\widehat{\mathfrak{h}}_{j}^{l+1} = \begin{cases} \tilde{\mathfrak{h}}_{j}, & |\tilde{\mathfrak{h}}_{j}| > c\tau_{l} \\ 0, & \text{otherwise} \end{cases}, \quad j=1,\cdots,2^{B_{\mathrm{p}}} \tag{5.15}$$

where $P_{\mathrm{h}} = \mathbb{E}||\mathfrak{h}||^2$ is the expected overall power estimated by

$$\widehat{P}_{\mathrm{h}} = ||\boldsymbol{y}_{\mathrm{p}}||^2 - N_{\mathrm{p}}N_0.$$

The probability of the user activity is given by $p_1 = \frac{K_{\mathrm{a}}}{2^{B_{\mathrm{p}}}}$, where $p_0 = 1 - p_1$, and the probability density functions of the fading amplitude and the interference are

$$p(a) \propto ae^{-\frac{a^2}{2}} \quad \text{and} \quad \rho(x|a;\tau) \propto e^{-\frac{(|x|-a)^2}{2\tau^2}}.$$

The algorithm starts with calculating the residual noise and interference $\boldsymbol{z}_{\mathrm{p}}^{l}$ shown in equation (5.10) and uses the total power constraint in the correction term as in [123]. The residual noise $\boldsymbol{z}_{\mathrm{p}}^{l}$ is matched-filtered with the sensing matrix $\mathbf{A}$ and accumulated with the previous estimate, to find the initial estimate $\mathfrak{r}^{l}$ of $\mathfrak{h}$ in (5.11). Since the system operates on the Rayleigh channel, we extend the AMP approach used for activity detection as in [116][111] to jointly estimate the channel coefficient and user activity. Under the assumption of Gauusian noise and interference the entries of $\mathfrak{r}^{l}$ are distributed as

$$\mathfrak{r}_{j}^{l} = |\mathfrak{h}_{j}|e^{i\ \arg(\mathfrak{h}_j)} + \tau_l\xi_j \quad j=1,2,\cdots,2^{B_{\mathrm{p}}} \tag{5.16}$$

where $\xi_j \sim \mathcal{CN}(0,1)$. Consequently, we estimate the amplitudes of the vector $\mathfrak{h}$ given the observations $\mathfrak{r}_j^l$ and assuming they are obtained in independent Gaussian channels with variance τ_l^2, where the probability of the user activity is p_1 and the Rayleigh amplitude

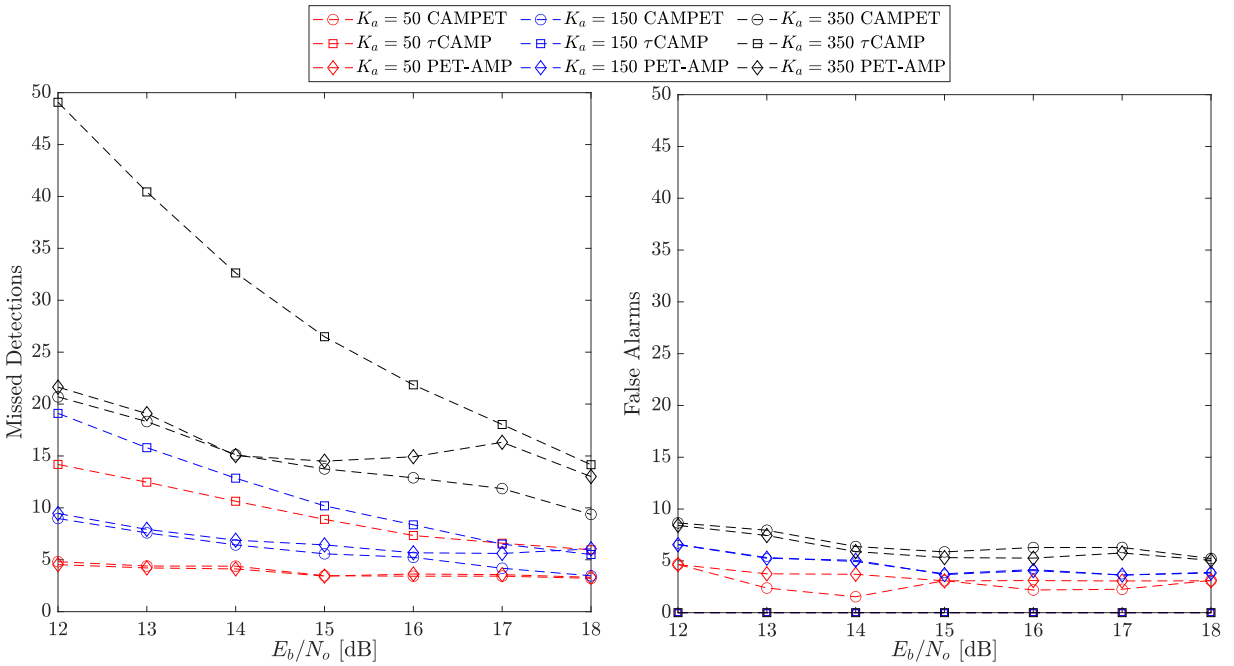

Figure 5.3: Numbers of misses and false alarms for τCAMP (squares), PET−AMP (diamonds), and CAMPET (circles) computed for a range of $E_{\rm b}/N_0$ and $K_{\rm a} = 50, 150, 350$ numbers active users and $N_{\rm p} = 350, 1250, 2125$ respectively.

distribution equals $p(a)$ (see (5.11)). The separate maximum likelihood estimate of the phase $\arg(\mathfrak{r}^l)$ is given in (5.13).

To actively suppress false alarms that appear in the iterative estimation process, we use a thresholding procedure (5.15) which is analogous to the thresholding that appears in many versions of AMP [120] to enforce sparsity in the estimated vector. We utilise $c = 2.8$, 2.9 or 3 for the range of active user numbers $K_{\rm a}$ and CS part lengths $N_{\rm p}$ of interest. The presented algorithm performs a number of iterations (typically set to 25) and the estimate $\widehat{\mathfrak{h}}^l$ that corresponds to the lowest τ_l is chosen for the output. The algorithm can produce an estimate with much smaller number of misses compared to τCAMP, and we will use τCAMP in the next section to improve it further.

τCAMP Assisted PET-AMP (CAMPET) Algorithm

The proposed PET-AMP algorithm introduces significantly less misses than τCAMP. On the other hand, τCAMP produces a very low level of false alarms, indicating that users estimated by τCAMP are reliable. Therefore, we combine both algorithms and reduce the miss-detection rate further. The following steps summarize the proposed combined CAMPET

algorithm:

1. Compute the estimate $\widehat{\mathbf{h}}_{\tau\text{CAMP}}$ using τCAMP. The set of active users $\mathcal{S}_{\tau\text{CAMP}}$ is defined as the set of indices of the nonzero entries of $\widehat{\mathbf{h}}_{\tau\text{CAMP}}$.

2. Compute $\widehat{\mathbf{h}}_{\text{PET}-\text{AMP}}$ using PET-AMP and obtain the set of active users $\mathcal{S}_{\text{PET}-\text{AMP}}$.

3. Calculate the difference $\mathcal{S}_{\Delta} = \mathcal{S}_{\tau\text{CAMP}} \setminus \mathcal{S}_{\text{PET}-\text{AMP}}$.

4. Assign $\widehat{\mathbf{h}}_{\text{CAMPET}} = \widehat{\mathbf{h}}_{\text{PET}-\text{AMP}}$ and then set $\widehat{\mathbf{h}}_{\text{CAMPET}}(\mathcal{S}_{\Delta}) = \widehat{\mathbf{h}}_{\tau\text{CAMP}}(\mathcal{S}_{\Delta})$.

Figure 5.3 compares the three algorithms in terms of the number of misses and false alarms for the cases of $K_{\text{a}} = 50$, $N_{\text{p}} = 350$ (red), $K_{\text{a}} = 150$, $N_{\text{p}} = 1250$ (blue), and $K_{\text{a}} = 350$, $N_{\text{p}} = 2150$ (black). The performance curves for τCAMP, PET$-$AMP, and CAMPET are shown by curves with squares, diamonds and circles respectively. The fact that CAMPET provides lowest number of misses, especially for the low range of E_{b}/N_0, is essential to lower the overall SNR requirement of the URA system. As E_{b}/N_0 increases, all algorithms have similar performance for $K_{\text{a}} = 50, 150$. For $K_{\text{a}} = 350$ users the advantage of combining τCAMP and PET$-$AMP is clearly visible. The number of false alarms stays relatively constant with respect to E_{b}/N_0. CAMPET has a slightly higher false alarm rate than the τCAMP. However, such increase in false alarm rate has a minor impact on the performance of the MUD algorithm applied to the MU parts of the packets.

5.3.3 Payload Receiver Based on Iterative Data Estimation and Interference Cancellation

The composite received signal for the MU parts of the packets is given by

$$\boldsymbol{y}_{\text{d}} = \sum_{k=1}^{K_{\text{a}}} h_k \boldsymbol{x}_{\text{d}}^{k} + \boldsymbol{z}_{\text{d}}. \tag{5.17}$$

Following the decoding of the CS parts of the packets discussed in Section 5.3.2, in this section we will describe the MUD algorithm applied to the received signal $\boldsymbol{y}_{\text{d}}$ in order to decode the MU parts. The decoder of the CS parts outputs the estimated data of the CS parts $\hat{\boldsymbol{v}}_{\text{p}}^{k}$ and the corresponding estimated indices $\hat{\nu}^{k}$, $k = 1, 2, \cdots, \hat{K}_a$ of the signature and permutation pairs utilized by the active users $k = 1, 2, \cdots, \hat{K}_a$ to encode the MU parts. By

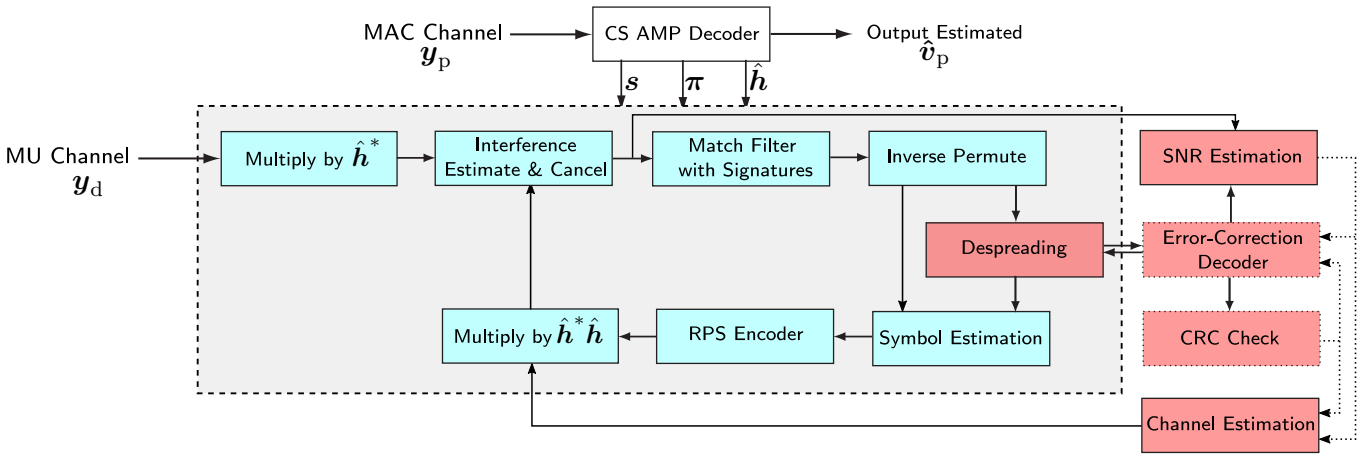

Figure 5.4: MUD receiver architecture.

$\hat{K}_{\mathrm{a}}$ we denote the number of packets detected by the CS part decoder that also outputs the estimated channel coefficients $\hat{h}_k$ of each detected active user.

Figure 5.4 depicts the block diagram of the MUD receiver. The main loop of the iterative decoder is highlighted by the gray color. The blocks that process the spread signal are shown by the blue color. The red blocks show processing of the despread symbols. To extract the data of the kth active user, $k = 1, 2, \cdots, \hat{K}_a$, the received signal $\boldsymbol{y}_{\mathrm{d}}$ (5.17) is multiplied by the conjugate of the estimated channel coefficient $\hat{h}_k$

$$\boldsymbol{r}_k = \hat{h}_k^* \boldsymbol{y}_{\mathrm{d}} = |h_k|^2 \boldsymbol{x}_{\mathrm{d}}^k + \sum_{\substack{k'=1 \\ k' \neq k}}^{K_{\mathrm{a}}} \hat{h}_k^* h_{k'} \boldsymbol{x}_{\mathrm{d}}^{k'} + \hat{h}_k^* \boldsymbol{z}_{\mathrm{d}} + e_k^* h_k \boldsymbol{x}_{\mathrm{d}}^k \ . \tag{5.18}$$

The second term on the right hand side of (5.18) comprises the interference from other users, the third term is the noise term, and the last term is the error due to the imperfect channel estimation where $e_k = \hat{h}_k - h_k$. The task of the MUD is to iteratively cancel the multi-user interference and ultimately decode the data $\boldsymbol{v}_{\mathrm{d}}^k$, $k = 1, 2, \cdots, \hat{K}_a$.

As shown in Figure 5.4, at each iteration the receiver performs estimation of the data bits, channel estimation, and interference cancellation. In addition, depending on the estimated SNR, the data may undergo error-correction decoding and a CRC check to test its correctness.

Data Estimation

At iteration i the log-likelihood ratios (LLR)s of the data bits of user k are calculated as

$$\hat{\boldsymbol{\lambda}}_k^{\,i} = \frac{2\tilde{\boldsymbol{r}}_k^{i-1}}{\sigma_{k,i-1}^2}, \tag{5.19}$$

where $\tilde{\boldsymbol{r}}_k^{i-1}$ is the estimate of $|h_k|^2\boldsymbol{x}_d^k$ at the ith iteration (given later by (5.24)) and the initial $\tilde{\boldsymbol{r}}_k^0 = \boldsymbol{r}_k$ at iteration $i = 0$. The noise and interference power experienced by the active user k at iteration $i-1$ is denoted by $\sigma_{k,i-1}^2$.

The LLR vector $\hat{\boldsymbol{\lambda}}_k^{\,i}$ (5.19) is multiplied by the signature sequence $\boldsymbol{s}^k$ and then de-interleaved using the inverse of the permutation $\boldsymbol{\pi}^k$. The real and imaginary parts of de-interleaved sequence are concatenated to produce a set of M LLRs $\tilde{\lambda}_{k,j,m}^i$, $m = 1, 2, \cdots, M$ for each data bit $j = 1, 2, \cdots, B_{\rm d}$ of user k, $k = 1, 2, \cdots, \hat{K}_{\rm a}$. These LLRs are then used to compute soft and hard estimates of the data bits for the purpose of error-correction decoding and interference cancellation as well as for refining the channel estimates. LLRs of the M different replicas of each data bit are added together and then the optimal (in MSE sense) conditional expectation estimate of a binary $\{-1, 1\}$ signal in a Gaussian noise and interference is computed

$$\vartheta_{k,j}^i = \sum_{m=1}^{M} \tilde{\lambda}_{k,j,m}^i \ , \tag{5.20}$$

$$\tilde{v}_{k,j}^i = \tanh\left(\vartheta_{k,j}^i\right) \ , \tag{5.21}$$

where $j = 1, 2, \cdots, B_{\rm d}$. The "soft symbols" of equation (5.21) can be used to produce hard decision QPSK symbols $\mathfrak{q}_{k,j}^i$, $j = 1, 2, \cdots, B_{\rm d}/2$ which will be used for refining of the estimated channel coefficients. In addition, in order to propagate the estimates of each bit replica and continue the iterative MUD process M different estimates (for the uncoded case) are computed

$$\tilde{v}_{k,j,m}^i = \tanh\left(\sum_{\substack{m'=1 \\ m' \neq m}}^{M} \tilde{\lambda}_{k,j,m'}^i\right), \quad m = 1, 2, \cdots, M, \quad j = 1, 2, \cdots, B_{\rm d} \ . \tag{5.22}$$

The estimates (5.22) are used to re-modulate the signals by applying permutation $\boldsymbol{\pi}^k$ and scrambling with $\boldsymbol{s}^k$. The resulting data signals $\tilde{\boldsymbol{x}}_{\rm d}^{i,k}$ will be used to perform interference cancellation.

Error-Correction Decoding, SNR Estimation, CRC Check

For that case when an error-correction code is used and the decoder is activated at the receiver, the LLRs $\vartheta_{k,j}^{i}$ are passed to the input of the decoder together with $\hat{\boldsymbol{v}}_{\mathrm{p}}^{k}$. The result of the decoding is utilized to form hard QPSK symbols, $\mathfrak{q}_{k,j}^{i}$ that are then repeated M times, permuted, and scrambled, to re-modulate the data of the respective packet prior to the interference cancellation.

In the CRC-aided successive cancellation list (CA-SCL) decoder, cyclic redundancy check (CRC) bits are appended to the coded bits to reduce the block error rate (BLER) [124]. CRC-aided polar codes are adopted in the 5G standard for both uplink and downlink channels. We exploit the CRC bits to decrease the complexity of the receiver and improve PUPE when the packets are encoded by a polar code. If the CRC bits of one packet are valid for two successive iterations of the MUD, the packet is considered as perfectly decoded and is not decoded in the subsequent iterations. We use two successive iterations to decrease the probability of a false positive of the CRC sequence.

SNR estimation plays a crucial role in the decoder to control the channel estimation and error correction blocks. For low SNRs, execution of error-correction decoding results in higher MSE compared to the case when the decoder is not applied as shown in Figure 5.5. Hence, implementing a threshold to switch between the two modes of operation when the error-correction decoder is on or off is critical, especially for the system encoded by a polar code. In addition, the MSE of the channel estimate depends on the SNR, and consequently on the bit error rate of a particular user (packet). If the SNR of the received signal is not high enough, the MSE of the channel estimate produced inside the MUD could be higher than the MSE of the channel estimate obtained from the CS part decoder. Therefore, switching between the error-correction decoding and no decoding regime is used for each packet, based on its SNR level.

Channel Estimation

As we already mentioned, the decoder of the CS parts provides the initial estimates of the channel coefficients, namely $\hat{h}_k$. The estimates are refined throughout the MUD iterations. As the iterations progress, naturally, the channel estimates get first improved for the high-power users and then for the low-power users. The channel coefficient of the kth user can

be estimated at each iteration via

$$\hat{h}_{i,k} = \frac{1}{B_{\rm d}/2} \sum_{j=1}^{B_{\rm d}/2} \frac{\vartheta_{k,j}^{i} \sigma_{k,i}^{2}}{2\hat{h}_{k,i-1}^{*} \mathfrak{q}_{k,j}^{i}} \ . \tag{5.23}$$

Interference Cancellation

The data signals $\tilde{\boldsymbol{x}}_{\rm d}^{i,k'}$ constructed from the M soft-bit replicas (5.22), or hard QPSK symbols in case the system is coded and the error-correction decoder is activated (see Figure 5.4), are used for the interference cancellation to compute

$$\tilde{\boldsymbol{r}}_{k}^{i} = \hat{h}_{i,k}^{*} \boldsymbol{y}_{\rm d} - \sum_{\substack{k'=1 \\ k' \neq k}}^{\hat{K}_{\rm a}} \hat{h}_{i,k}^{*} \hat{h}_{i,k'} \tilde{\boldsymbol{x}}_{\rm d}^{i,k'}, \quad \boldsymbol{\sigma}_{k,i}^{2} = \mathrm{var} \left(\hat{h}_{i,k}^{*} \boldsymbol{y}_{\rm d} - \sum_{k'=1}^{\hat{K}_{a}} \hat{h}_{i,k}^{*} \hat{h}_{i,k'} \tilde{\boldsymbol{x}}_{\rm d}^{i,k'} \right) \ . \tag{5.24}$$

The average NIP equals $\sigma_{k,i}^{2} = \bar{\boldsymbol{\sigma}}_{k,i}^{2}$. The cancelled signals $\tilde{\boldsymbol{r}}_{k}^{i}$ will be used to produce the LLRs (5.19) in the next $(i+1)$th iteration. The iterative MUD process continues until the normalized NIP $\sigma_{k,i}^{2}/|h_k|^2$ approaches the level of the noise power $\sigma^2 = N_0/2$ (per Re/Im dimension). This would correspond to the "single-user" performance. The conditions for convergence of the system to the single-user performance are investigated in Section 5.4.

Impact of Misses, False Alarms, and User Collisions on MUD Operation

Some active users' packets are not detected by the decoder of the CS parts. The packets of those missed users behave as interference for other users in the MUD receiver and would not be cancelled by (5.24). At the same time, some false users are introduced by the CS decoder algorithm to MUD by mistake due to false alarms. These will be referred to as false users. The false users can inject interference into the iterative decoder at the stage when the transmit signal is regenerated as $\hat{h}_{k'} \tilde{\boldsymbol{x}}_{\rm d}^{k'}$. It turns out that the vast majority of the false users are of low power and cannot increase the residual interference dramatically.

Another phenomenon that degrades the performance of the MUD algorithm is the collisions of pairs of active users. As we mentioned earlier a collision happens when two active users select the same signature and permutation pair $(\boldsymbol{s}^k, \boldsymbol{\pi}^k)$ to send their message. In such case the decoder of the CS parts detects the channel-faded signals of the two colliding users as a single user. The estimated channel coefficient approximates the sum of the channel coefficients of the two colliding users and the resulting "combined user" signal is passed to the MUD. The MUD algorithm, in turn, can often detect and decode the user with the

highest power out of the two users in a collision. This happens if the difference between the powers of the two colliding users is high enough. Apart from that, both colliding users are not detectable by the MUD algorithm. In contrast to the case of missed and false users, the power of colliding users could be high and could increase the interference dramatically if the number of collisions is significant.

5.4 Performance Analysis

In this section we present a performance analysis of the MUD operating on the MU parts of the packets. The analysis is based on the evolution of the NIP as well as the MSE of the data estimates that we track throughout the iterative interference cancellation process.

5.4.1 Analysis in Absence of User Collisions

We consider a system with K_{a} active users where the powers of their respective packets at the receiver are given by $P_k = |h_k|^2$, $k = 1, 2, \cdots, K_{\mathrm{a}}$. We start with considering the case when the user collisions are absent i.e. all the users happen to select distinct signature and permutation pairs. We also start with the assumption that all users' packets have been detected correctly by the algorithm processing the CS parts, the channel coefficients have been estimated perfectly, and no false alarms have been produced. First, we derive the analysis equations for the case when the packets are uncoded.

In case of perfect channel knowledge the interference cancellation equation (5.24) at iteration $i = 1, 2, \cdots$ can be written as

$$\boldsymbol{r}_k^i/|h_k| = |h_k|\boldsymbol{x}_{\mathrm{d}}^k + \sum_{\substack{k'=1 \\ k' \neq k}}^{K_{\mathrm{a}}} h_k^* h_{k'}/|h_k| \left(\boldsymbol{x}_{\mathrm{d}}^{k'} - \tilde{\boldsymbol{x}}_{\mathrm{d}}^{i,k'}\right) + h_k^*/|h_k|\boldsymbol{z}_{\mathrm{d}} \ , \tag{5.25}$$

$$\boldsymbol{r}_{k,j}^i/|h_k| = |h_k|v_{k,j} + \eta_{k,j}, \quad j = 1, 2, \cdots \tag{5.26}$$

where the power of the noise and interference term $\eta_{k,j}$ (per real or complex dimension) is given by

$$\begin{aligned}\chi_i = \sigma_{k,i}^2/|h_k|^2 = \mathbb{E}\eta_{k,j}^2 &= \sum_{k'=1}^{K_{\mathrm{a}}} |h_{k'}|^2 \mathbb{E}\left(v_{k',j} - \tilde{v}_{k',j}^i\right)^2 + \sigma^2 \\ &= \sum_{k'=1}^{K_{\mathrm{a}}} P_{k'} \mathbb{E}\left(v_{k',j} - \tilde{v}_{k',j}^i\right)^2 + \sigma^2 \ . \end{aligned} \tag{5.27}$$

Since we consider the optimal estimator (5.20) of the binary signal $v_{k,j} \in \{-1, 1\}$ in a Gaussian noise and interference, the MSE of the estimate is given by

$$\mathbb{E}\left(v_{k,j} - \tilde{v}_{k,j}^{i}\right)^2 = g\left(\frac{P_k}{\chi_{i-1}}\right),$$

where the function

$$g(s) = 1 - \frac{1}{\sqrt{2\pi}} \int_{-\infty}^{\infty} e^{-z^2/2} \tanh\left(s - z\sqrt{s}\right) dz \tag{5.28}$$

derived in [125] is the MSE of the maximum a posteriori probability (MAP) estimation of equiprobable binary $\{1, -1\}$ signals in AWGN $\mathcal{N}(0, s^{-1})$. Following the interference cancellation stage of iteration i the MSEs of all users $k = 1, 2, 3, \cdots$ will jointly contribute to the overall NIP after iteration i resulting in

$$\chi_i = \sum_{k=1}^{K_\mathrm{a}} P_k g\left(\frac{P_k}{\chi_{i-1}}\right) + \sigma^2 \ .$$

where we do not account for the fact that the kth user is not a part of the interference.

Since the channels of the users are Rayleigh we can write a continuous approximation based on the Rayleigh probability density function $p(\cdot)$ of the received signal amplitudes

$$\chi_i = \alpha_\mathrm{a} \int_0^{\infty} r^2 p(r) g\left(\frac{r^2}{\chi_{i-1}}\right) dr + \sigma^2 = \alpha_\mathrm{a} g_\mathrm{f}\left(\frac{1}{\chi_{i-1}}\right) + \sigma^2 \quad i = 1, 2, 3, \cdots \tag{5.29}$$

where $\alpha_\mathrm{a} = K_\mathrm{a}/M$ is the active user load computed as the ratio of the number of active users to the repetition factor M and

$$g_\mathrm{f}\left(\chi^{-1}\right) = \int_0^{\infty} r^2 p(r) g\left(\frac{r^2}{\chi}\right) dr$$

denotes the average MSE of the entire user population. The initial NIP, before the MUD iterations start, equals

$$\chi_0 = \alpha_\mathrm{a} g_\mathrm{f}(0) + \sigma^2 = \alpha_\mathrm{a} \int_0^{\infty} r^2 p(r) g(0)\, dr = \alpha_\mathrm{a} + \sigma^2 \ . \tag{5.30}$$

Equation 5.29 characterises the evolution of the NIP throughout the MUD iterations. The goal of the MUD process is to cancel (almost) all the multi-user interference, in which case the sequence χ_i will decrease with i and approach the noise power σ^2. Often, however, the interference cancellation process stops at a point where the NIP χ_i does not decrease

as a function of i and remains significantly larger than σ^2. To study the evolution of the interference cancellation process we define a characteristic equation

$$\chi = \alpha_{\mathrm{a}} g_{\mathrm{f}} \left(\frac{1}{\chi} \right) + \sigma^2. \tag{5.31}$$

The convergence of the interference cancellation process is characterized by the largest fixed point (FP) χ^* of (5.31). The final BLER (for the case of uncoded transmission) is one of the main contributors to the PUPE and is determined by

$$P_{\mathrm{bl}} = \int_0^\infty \left(1 - (1 - Q(\sqrt{r^2/\chi^*}))^{B_{\mathrm{d}}}\right) p(r) dr$$
$$\text{where} \qquad Q(s) = \frac{1}{\sqrt{2\pi}} \int_s^\infty \exp(-z^2/2) dz \ .$$

based on hard decisions taken after the last MUD iteration for each bit independently. For the case when the interference cancellation process converges to the level close to the noise power σ^2 we can substitute $\chi^* \approx \sigma^2$ in the above expression.

The Two-Stage Decoding Schedule

Consider now the case when the data is encoded with an (n, B) error-correction code $\mathcal{C}$. The simplest decoding schedule at the receiver is the two-stage decoding schedule when the receiver performs MUD first, without involving the error-correction decoder at the (the first stage). Once the MUD reaches a point where the average SNR of the packets equals a certain threshold γ, the ECC decoding is performed for each packet individually and the final result is produced (the second stage). The MUD cutoff threshold γ is selected based on the target BLER and the error-correction code properties.

To achieve the best performance of this schedule we can let the first MUD stage achieve the point of saturation described by the highest FP of the characteristic equation (5.31). The final post-MUD SNR for a packet received with power r^2, $r \in [0, \infty]$, is given by r^2/χ^* where r is the fading gain. Let us denote the BLER provided by the ECC $\mathcal{C}$ at SNR s by $P_{\mathcal{C}}(s)$. The final BLER can then be computed as

$$P_{\mathrm{bl}} = \int_0^\infty P_{\mathcal{C}} \left(r^2/\chi^* \right) p(r) dr \ . \tag{5.32}$$

Joint MUD/ECC Decoding

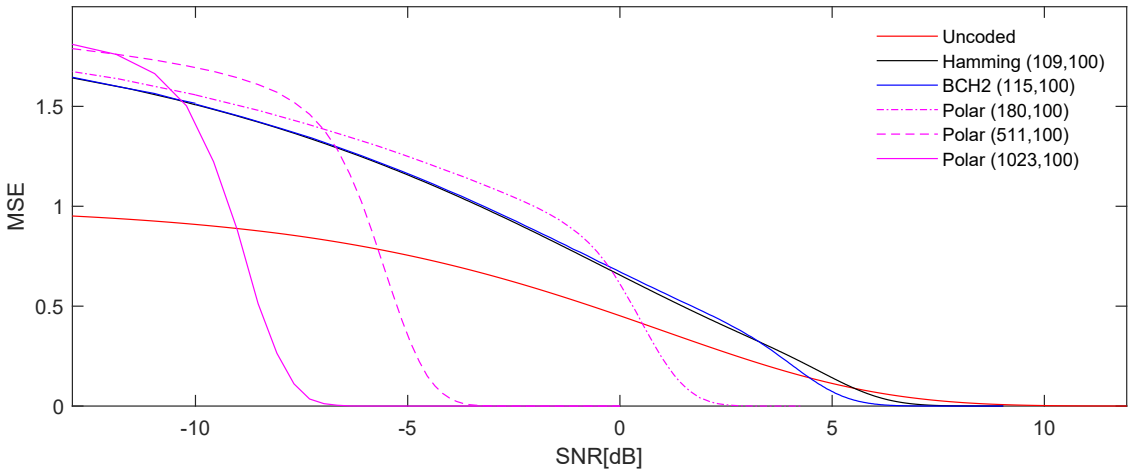

Figure 5.5: MSE of coded and uncoded estimated BPSK signals in AWGN.

The next schedule we consider is a joint decoding schedule when the MUD and the decoding of the ECC are executed jointly in an iterative fashion, see Section 5.3.3. At every iteration MUD bit estimation (from the repetition), error-correction decoding, and the MUD interference cancellation can be executed. As we will see it is beneficial not to perform the error-correction decoding at the initial iterations when the SNR of the system is too low, since the decoder introduces more errors than it corrects. It is more beneficial, as shown by the analysis, to engage the decoder once the SNR of a particular packet reaches the level when the decoder can contribute to the interference cancellation process.

For the data encoded with an (n, B) error-correction code $\mathcal{C}$ we can define and numerically compute the MSE of the post-decoding data $\hat{v}$ in an AWGN channel with SNR s as

$$g_{\mathrm{c}}(s) = 4\mathbb{E}(v - \hat{v}(s))^2 \ , \tag{5.33}$$

assuming that the coded bits were modulated with BPSK modulation. Figure 5.5 shows the MSE $g_{\mathrm{c}}(s)$ in AWGN for a number of ECCs used in this work, plotted as a function of the SNR $s = P/\sigma^2$ per coded bit. The red curve corresponds to the uncoded MSE $g(s)$ (5.28).

One of the error-correction codes we consider is the double-extended systematic Hamming $(128, 119)$ code used in 400ZR optical communication standard [126]. We shortened it to $(109, 100)$ so that it contains 100 information bits for the purpose of comparison with the related work discussed later in Section 5.5. We use a decoding algorithm that takes into account soft input information (LLRs) of the received sequence and outputs a codeword (hard decision). The algorithm is the direct error-pattern testing (DEPT) algorithm, presented in

[127] that uses 64 partial error-patterns. The respective Hamming code MSE is given by the black curve. In addition, we consider a double error-correcting systematic BCH [113, 114] code $(128, 113)$ shortened to $(115, 100)$ and decoded with DEPT algorithm using 575 patterns (blue curve). For both BCH and Hamming codes, for simplicity, we consider hard decision feedback from the decoder to the MUD as discussed in Section 5.3.3.

Finally, we consider several 5G polar codes including the $(1023, 100)$ code (solid magenta curve), $(511, 100)$ code (dashed magenta curve), and $(181, 100)$ code (dash-dotted magenta curve). All codes are rate-adjusted to contain 100 information bits. Each code is using 11 CRC bits and is decoded with a list size of 64.

We can see that for high SNRs stronger and more powerful codes outperform their counterparts in terms of MSE. However, for low SNRs the situation is opposite. Note also that for low SNRs the MSE of the uncoded transmission is much lower than that of the coded transmission due to high numbers of errors and the hard decoding output. By $s = \gamma_{\text{switch}}$ we will denote the SNR point where the uncoded MSE $g(s)$ and the coded MSE $g_{\text{c}}(s)$ intersect.

Thus, we can consider an MUD schedule at the receiver that tracks the signal-to-noise and interference ratio (SINR) r^2/χ_i of every user (packet). For any given user the estimation phase of every iteration is carried out without the decoding feedback until the SINR of the data bits reaches a level close to γ_{switch}. After that we engage hard decoding at every iteration for this user. The switching between the uncoded data estimation and error-correction decoding, based on the optimal SINR, changes the MSE function to $\bar{g}(s) = \min\{g(s), g_{\text{c}}(s)\}$ and the resulting characteristic equation to

$$\chi = \alpha_{\text{a}} \bar{g}_{\text{f}} \left(\frac{1}{\chi} \right) + \sigma^2 = \alpha_{\text{a}} \int_0^\infty r^2 p(r) \bar{g} \left(\frac{r^2}{\chi} \right) dr + \sigma^2 \ . \tag{5.34}$$

The largest FP χ^* of (5.34) predicts convergence of the system to SNR $1/\chi^*$ where the final BLER is given by (5.32).

The performance may be improved with use of a soft decoding feedback at the expense of increased decoding complexity. On the other hand, switching between the LLR-based data estimation and decoding optimizes the use of the error-correction code, and the availability of a soft feedback may not provide high additional gains.

Accounting for CS Part Decoding

We can now take into account some of the imperfections of the CS part decoding that influence the MUD of the MU parts. CS decoders use thresholding to suppress small entries

of the estimated user activity vector. All users (packets) corresponding to the entries that fall below that threshold after the final CS decoder iteration are missed.

Such missed users contribute to the noise and interference power throughout the MUD iterations and we assume, for simplicity, that the MSE of these users equals 1. This leads to the convergence equation that takes into account the thresholding in the CS part decoding algorithm

$$\chi = \alpha_{\mathrm{a}} g_{\mathrm{f,t}}\left(\frac{1}{\chi}, \theta\right) + \int_0^{\theta} r^2 p(r) dr + \sigma^2, \tag{5.35}$$

where

$$g_{\mathrm{f,t}}\left(\chi^{-1}, \theta\right) = \int_{\theta}^{\infty} r^2 p(r) g\left(\frac{r^2}{\chi}\right) dr \ .$$

The threshold parameter θ can be computed based on the overall probability of miss produced by the CS decoder, assuming, for simplicity, that all users below the threshold θ are missed and all the users above are decoded.

The impact of false users is usually more complicated to predict and take into account, since it is difficult to estimate their power distribution. Simulation results suggest that moderate numbers of false users do not impact the performance significantly.

5.4.2 The Impact of User Collisions

Consider now the general case when some of the active users may select the same signature and permutation pairs from the available pool. This selection happens in every time slot uniformly at random. Let's assume that in a given time slot k_{s} users select a signature and permutation pair which is not unique.

In a typical scenario such k_{s} colliding users appear in form of $k_{\mathrm{s}}/2$ user pairs where two users within a pair select the same signature and permutation. For large numbers of active users K_{a} a single triple of users that select the same signature and permutation may occur. The cases of more that one triple and more than three users involved in a collision have insignificant probability for our parameter setting. Probability distributions of the number of colliding users per time slot for $B_{\mathrm{p}} = 17$ and various K_{a} are given in Figure 5.6 for K_{a} equal to 10 (red circles), 200 (blue squares), 600 (black triangles), 1000 (magenta stars), and 1400 (green diamonds). The part of a probability distribution for which the users are involved solely in pair collisions is given by a solid curve. The part of a distribution that involves a single triple is given by a dashed curve.

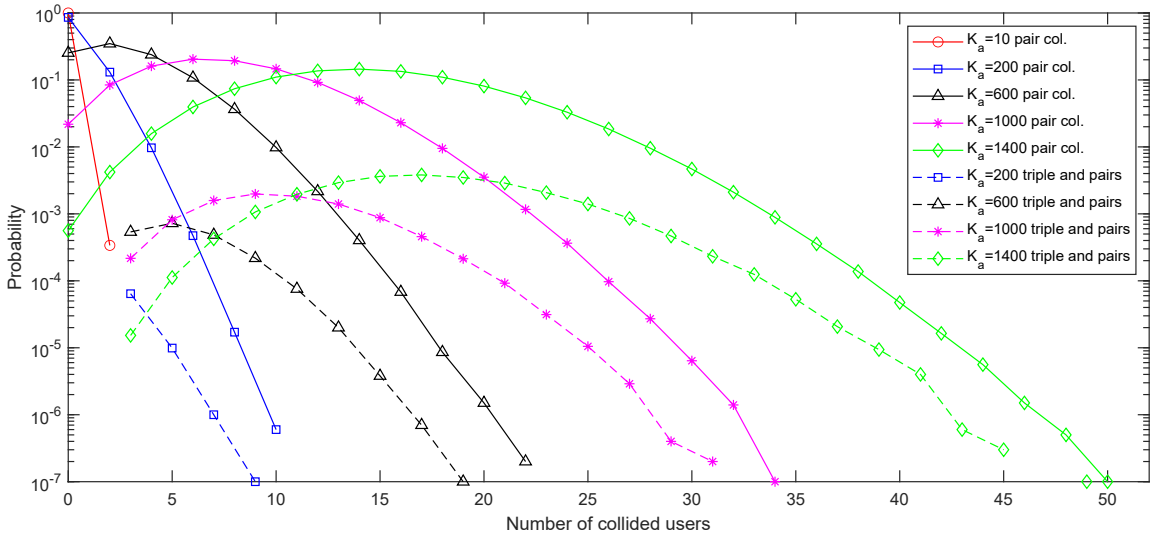

Figure 5.6: Probability distribution of the number of colliding users for $B_{\rm p} = 17$ and $K_{\rm a} = 10, 200, 600, 1000, 1400$. The solid curves show the probabilities of the numbers of users involved in pair collisions. The dashed curves are for the case of a single triple collision and several pair collisions.

Based on the observations related to collision resolution in the MUD process given in Section 5.3.3 the highest power user in a collision is often decoded. Hence we make an approximation and assume that we can always decode half of the users involved in collisions. The $k_{\rm s}/2$ weaker users become a part of the Gaussian noise and interference. The resulting characteristic equation for the case of $k_{\rm s}$ users involved in collisions and considering the thresholding θ related to the number of misses produced by the CS decoding algorithm is given by

$$\chi = \frac{K_{\rm a} - k_{\rm s}/2}{M} \bar{g}_{\rm f,t}\left(\frac{1}{\chi}, \theta\right) + \int_0^{\theta} r^2 p(r) dr + \frac{k_{\rm s}}{4M} + \sigma^2 \ . \tag{5.36}$$

Note that the average power of a small user in a collision is $1/2$ (and not 1) based on the order statistic and Rayleigh distribution of the channel fading. The highest FP $\chi^*(k_{\rm s})$ of (5.36) results in BLER $P_{\rm bl}(k_{\rm s})$ computed based on the error-correction code which is used. Finally the overall PUPE is computed as an expectation $\mathbb{E}P_{\rm bl}(k_{\rm s})$ taken over the distribution of the numbers of colliding users $k_{\rm s}$.

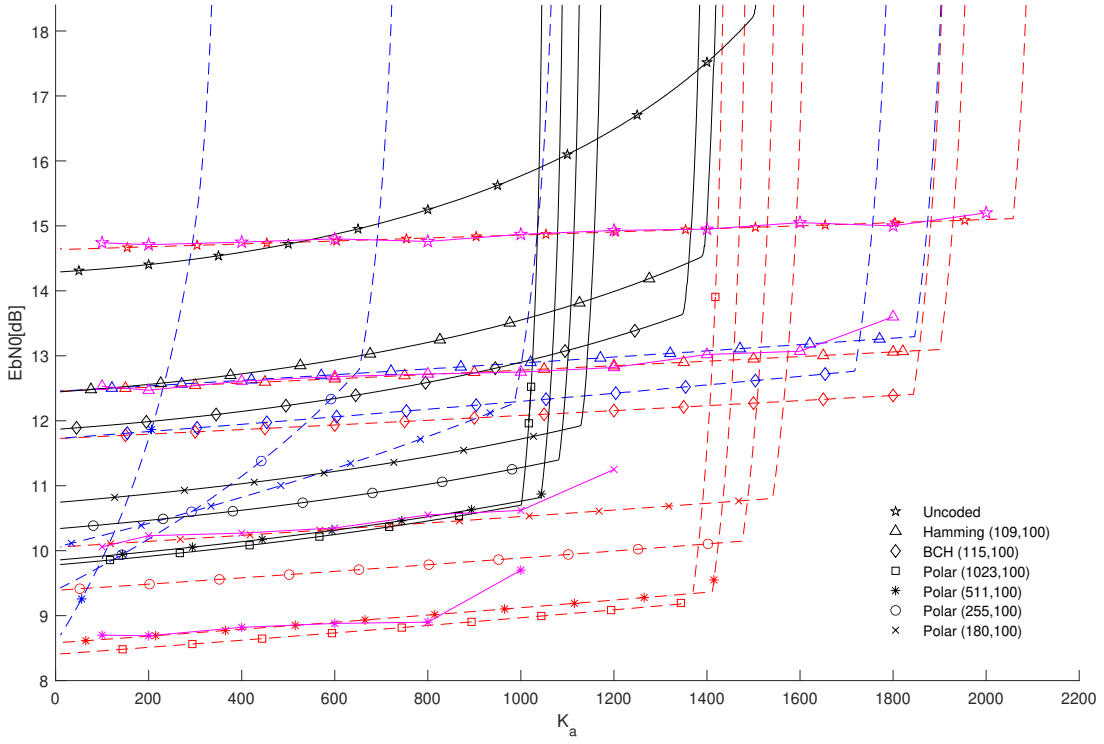

Figure 5.7: The minimum E_{b}/N_0 required to achieve PUPE of 0.1 for uncoded and coded systems without CS part and joint MUD/ECC decoding (red dashed curves), two-stage decoding (blue dashed curves), simulated (solid magenta curves). Systems with a CS part, user collisions, and joint MUD/ECC decoding are shown by the solid black curves.

5.4.3 Analysis Results

Finally we present the numerical results for the performance analysis derived in this section. We consider a commonly used setup of [12] where the length of the users' messages equals $N_t = 30000$ channel uses and each user transmits a packet that encodes $B = 100$ information bits. We set the required level of PUPE to 0.1 as in [20]. Figure 5.7 demonstrates the smallest E_{b}/N_0 required to achieve PUPE of 0.1 for a variety of systems. Each curve is plotted as a function of the number of active users K_{a}. In all cases we consider $B_{\mathrm{p}} = 17$ for the CS part. Rayleigh fading channel is considered and it is assumed that the channel coefficients are known by the MUD receiver, the impacts of misses and false alarms are not considered on this plot.

The dashed red curves correspond to the analysis computed for the case when the entire packet of length N_{t} is dedicated to the payload where $N_{\mathrm{d}} = N_{\mathrm{t}}$ ($N_{\mathrm{p}} = 0$) and the repetition

factor $M \approx 2N_{\mathrm{t}}/B_{\mathrm{d}}$. Joint MUD/ECC decoding schedule with SNR-based decoder activation is applied. The dashed blue curves correspond to the same parameter setting but with the two-stage decoding schedule. The markers on the curves indicate uncoded transmission $n = B$ (pentagrams), as well as encoding by Hamming code $(109, 100)$ (triangles), BCH $(115, 100)$ (diamonds), polar $(180, 100)$ (crosses), polar $(255, 100)$ (circles), polar $(511, 100)$ (stars), and polar $(1023, 100)$ (squares). The characteristic knee-shaped turns of the curves occur at the points where the highest FP of the respective characteristic equation deviates from the near-optimal $\chi^* \approx \sigma^2$ as the number of active users increases. The phase-transition change occurs, and the interference cancellation is no longer capable to provide near "single-user" performance. The simulations for the joint MUD/ECC schedule without preamble are given by the solid magenta curves. In all the above scenarios we do not consider the impact of the user collisions.

The solid black curves correspond to the case when the length of the CS equals $N_{\mathrm{p}} = 8000$ and it uses 12dB SNR. The repetition factor of the MU part is adjusted to $2(N_{\mathrm{t}} - N_{\mathrm{p}})/B_{\mathrm{d}}$ while we still consider the "perfect" decoding of the CS parts. The impact of the user collisions as per Section 5.4.3 is taken into account for this set of curves.

We note that the joint MUD/ECC schedule provides results that are superior to that of the two-stage schedule. The difference is especially pronounced for stronger polar codes of lower rates. For the case of polar codes, the main benefit of coding comes from the integration of the code into the decoding process where it helps to work at low SNRs. This capability comes at the price of increased active user load due to the low coding rate, since the overall packet length is fixed. Therefore, using such codes in a two-stage schedule is inefficient and the MUD has to combat high active user load at the first decoding stage without any help of the error-correction decoding. For high-rate codes the difference in performance between the two-stage and joint MUD schedules is small. For the uncoded case the performances of both schedules naturally coincide. We also note that the analysis provides a good match to the simulation results.

Finally, we note that presence of the CS part impacts the results in terms of the overall SNR that takes into account both CS and MU parts of the packet (black curves). Since the MU part is shorter, the repetition factor M is reduced and the active user load increases compared to the zero-length CS part case. Hence, the point of no convergence, when the system is no longer capable to support the active user load, occurs for a smaller number of

active users. The user collisions contribute to the increased noise and interference floor of the system (5.36) and result in a slight concavity of the curves upwards towards higher required SNRs. This can be seen for the black curves with pentagrams, diamonds, and triangles. This happens specifically for the $800 - 1500$ user range where the impact of collisions becomes significant. In the next section we will compare the results of the analysis and full numerical system simulations.

5.5 Numerical Results

To evaluate the system's performance numerically here we again consider $N_{\mathrm{t}} = 30000$, $B = 100$, and a PUPE level of 0.1. The CAMPET algorithm is used to decode the CS part and it passes the data to the MUD working on the MU parts of the packets. The minimum E_{b}/N_0 of the entire packet is computed as

$$\frac{E_{\mathrm{b}}}{N_0} = \frac{s_{\mathrm{d}} B_{\mathrm{d}} + s_{\mathrm{p}} B_{\mathrm{p}}}{nR} = \frac{s_{\mathrm{d}} B_{\mathrm{d}} + s_{\mathrm{p}} B_{\mathrm{p}}}{B}, \tag{5.37}$$

where $R = B/n$ is the ECC rate, s_{p} is the SNR per data bit of the CS part used to detect permutation and signatures sequences and perform an initial channel estimate. By s_{d} we denote the SNR per data bit of the MUD part, required to achieve PUPE of 0.1 that combines the probability of misses in the CS part and the block errors in the MUD part.

Figure 5.8 shows the minimum E_{b}/N_0 required to achieve the desired PUPE as a function of the number of the active users K_{a} in the system. We consider $B_{\mathrm{p}} = 17$ bits in the CS part of the messages for all the experiments. In order to optimize the performance we use different SNRs for the CS and MU parts. The SNR of the CS part equals 12dB for $K_{\mathrm{a}} \leq 400$, 13dB for $K_{\mathrm{a}} = 500$, 14dB for $K_{\mathrm{a}} = 600$, 15dB for $K_{\mathrm{a}} \in [800, 1000]$, and 18dB for $K_{\mathrm{a}} \geq 1200$. For the cases when polar codes are used as ECC, the N_{p} of the CS part is set to 8000 for $K_{\mathrm{a}} = 100, 200$ and $N_{\mathrm{p}} = 6500$ for $K_{\mathrm{a}} \geq 300$. For the case of uncoded transmission and transmission using $(109, 100)$ shortened Hamming code $N_{\mathrm{p}} = 8000$ is used for all K_{a}. For each case the repetition parameter M of the MU part is selected to ensure that the overall packet length $N_{\mathrm{t}} \approx 30000$.

The solid black curve corresponds to the system which is encoded by the $(109, 100)$ Hamming code. The uncoded system results are shown by the solid blue curve. Note that both systems can support very high numbers of active users. The dashed blue curve shows the result based on the analysis of the MUD performance presented in Section 5.4 for the

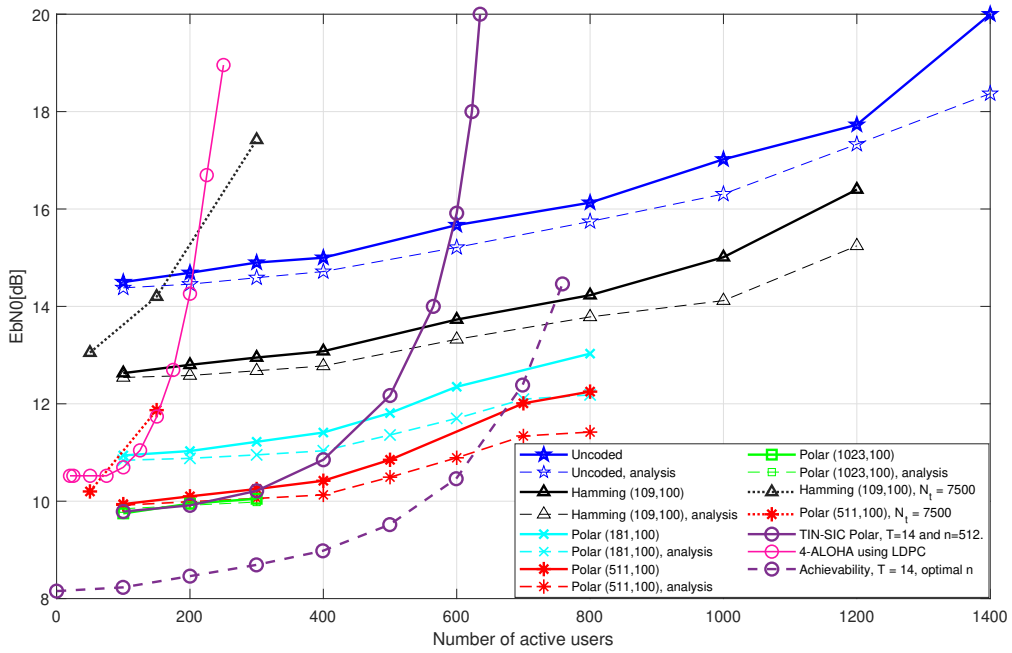

Figure 5.8: Minimum required E_{b}/N_0 as a function of K_{a} for PUPE ≤ 0.1, $N_{\mathrm{t}} = 30000$ and 7500, $B = 100$, block Rayleigh fading.

uncoded system. Similarly the dashed black curve shows the analysis result for the Hamming-coded system. The practical imperfections such as the rate of misses, distribution of user collisions, and the SNR required by the CS part decoder are considered in the calculation of the analytical curves. The analysis results are in good agreement with the simulated performance. Channel estimation error and presence of false users cause some deviation for higher numbers of users.

The minimum required SNRs of the systems encoded with the $(181, 100)$, $(511, 100)$, and $(1023, 100)$ polar codes, discussed in Section 5.4, are given by the solid cyan, red, and green curves, respectively. The anaysis results for the polar-coded systems are plotted by the dashed curves of the same color.

Note that longer polar codes with lower rates provide lower required SNRs that translate into the best performance. Since the overall packet length N_{t} is fixed, large code length n reduces the repetition factor M that can be used and increases the active user load $\alpha_{\mathrm{a}} = K_{\mathrm{a}}/M$. Therefore, such codes can only be used for smaller and medium K_{a}, not exceeding 800 in this case. Higher active user loads can be supported by Hamming-coded transmission and uncoded transmission and require somewhat higher SNRs. This observation, confirmed by

the analysis results shown in Figures 5.7 and 5.8, suggests that stronger codes are beneficial for small numbers of users when the noise presents a more significant impairment than the multi-user interference. High numbers of users necessitate high-rate codes or uncoded transmission, that is capable to operate with higher repetition factors and deliver stronger MUD performance.

For comparison, the performances of the two existing state-of-the-art URA systems are also shown in Figure 5.8. These are the 4-fold ALOHA system that uses LDPC codes [20] (pink solid curve with circles) and the treat interference-as-noise successive interference cancellation (TIN-SIC) scheme using polar codes [21] (solid purple curve with circles). Both systems consider block fading Rayleigh channel. However, the channel is allowed to change on the scale of the sub-slots used by the ALOHA system. In the TIN-SIC algorithm a 14-fold ALOHA is applied and the ALOHA sub-slot length is $n = 512$. The theoretic achievablity bound of the TIN-SIC decoder constructed using random coding arguments is plotted by the dashed purple curve.

The presented system outperforms the related work in terms of the achievable active user numbers by more than twice. In addition, for the case when the number of active users $K_{\mathrm{a}} \geq 300$ the system outperforms the state-of-the-art systems in terms of the minimum required SNR as well. The results for low user numbers are at par with the related works.

We have also considered a system with $N_{\mathrm{t}} = 7500$ and $N_{\mathrm{p}} = 2000$ to study the flexibility of the proposed design with respect to the packet length and adaptability to the coherence block length of the fading channel. The overall number of information bits equals $B = 100$ while $B_{\mathrm{p}} = 15$ is considered. The results of the Hamming coded and polar $(511, 100)$ coded systems are shown by the black and red dotted curves respectively. The $N_{\mathrm{t}} = 7500$ system needs approximately $0.2 - 1$ dB more power than the $N_{\mathrm{t}} = 30000$ length system to support the same active user density K_a/N_t. On the other hand, we demonstrate that for $K_{\mathrm{a}} \leq 300$ the system with a much smaller block length is sufficient to communicate $B = 100$ bits of information in a URA fashion.

5.6 Conclusions

The chapter considers a URA over fading channels and focuses on the approach where each transmitted packet is equipped with a CS preamble part for the purpose of URA and channel estimation, and an MU data payload part encoded via permutation and scrambling for

non-orthogonal multiple-access. We propose a decoding algorithm to decode the CS parts of the packets that can support high numbers of active users and perform their channel estimation. We also present an MUD algorithm for the MU parts that allows for iterative data detection, channel estimation, and flexible error-correction code activation, based on the current signal-to-noise and interference ratio as predicted by the presented performance analysis. We demonstrate that the proposed design outperforms state-of-art methods in terms of both supported multi-user load and the SNR required to guarantee a certain level of per-user error probability.

Chapter 6

Conclusion and Future Work

In this thesis, we presented two iterative cancellation receivers that operate in two drastically different communication environments. The underwater channel, characterized by its doubly-selective nature presents a serious challenge for the channel estimator, especially for the case of OFDM transmission over a channel with high Doppler spread. The presented Kalman filter-combiner is able to provide accurate channel estimates for significant levels of Doppler spreads, while utilizing a relatively simple model. It is shown to provide good performance in combination with interference-cancellation type iterative receiver. Further investigation on improving the estimation performance, especially in MIMO setting, is needed to support higher number of transmitted data streams that resemble higher-order constellations. The combined analysis of estimation and iterative receiver, through the state evolution would allow for better parameters optimization for different sea states and Doppler spreads.

The presented channel model for the case of MIMO underwater channels provides a step forward in terms of model construction based on physical understating of the environment. The current model is suitable for calm seas, when the curvature of the surface is small, and additional extensions are necessary to enhance the validity of the model.

The presented URA system attempts to combine the best of unsourced user activity detection via the compressed sensing preamble, and the strong multi-user detection for the payload. Extension to MIMO and massive MIMO settings are a very natural direction of the future work. Additionally, a state evolution study for the presented AMP algorithms would allow for optimization of preamble parameters, and optimal integration with the MUD part.

Bibliography

[1] D. Truhachev, C. Schlegel, M. Bashir, and J.-F. Bousquet, "Modeling of underwater acoustic channels for communication system testing," in *OCEANS 2018 MTS/IEEE Charleston*. IEEE, 2018, pp. 1–8.

[2] M. B. Porter, "The bellhop manual and user guide: Preliminary draft," *Heat, Light, and Sound Research, Inc., La Jolla, CA, USA, Tech. Rep*, 2011.

[3] J. C. Peterson and M. B. Porter, "Ray/beam Tracing For Modeling The Effects Of Ocean and Platform Dynamics," *IEEE Journal of Oceanic Engineering*, vol. 38, no. 4, pp. 655–665, 2013.

[4] P. Qarabaqi and M. Stojanovic, "Statistical characterization and computationally efficient modeling of a class of underwater acoustic communication channels," *IEEE Journal of Oceanic Engineering*, vol. 38, no. 4, pp. 701–717, Oct 2013.

[5] A. Abdi and H. Guo, "A new Compact Multichannel Receiver for Underwater Wireless Communication Networks," *IEEE Transactions on Wireless Communications*, vol. 8, no. 7, pp. 3326–3329, 2009.

[6] M. Naderi, A. G. Zajić, and M. Pätzold, "A nonisovelocity geometry-based underwater acoustic channel model," *IEEE Transactions on Vehicular Technology*, vol. 67, no. 4, pp. 2864–2879, 2017.

[7] P. Hoeher, "A statistical discrete-time model for the wssus multipath channel," *IEEE Transactions on vehicular technology*, vol. 41, no. 4, pp. 461–468, 1992.

[8] M. Suzuki, T. Sasaki, and T. Tsuchiya, "Digital acoustic image transmission system for deep-sea research submersible," in *OCEANS 92 Proceedings@ m_Mastering the Oceans Through Technology*, vol. 2. IEEE, 1992, pp. 567–570.

[9] Y. M. Aval and M. Stojanovic, "Differentially coherent multichannel detection of acoustic ofdm signals," *IEEE Journal of Oceanic Engineering*, vol. 40, no. 2, pp. 251–268, 2014.

[10] B. Li, S. Zhou, M. Stojanovic, L. Freitag, and P. Willett, "Multicarrier communication over underwater acoustic channels with nonuniform doppler shifts," *IEEE Journal of Oceanic Engineering*, vol. 33, no. 2, pp. 198–209, 2008.

[11] K. Tu, D. Fertonani, T. M. Duman, M. Stojanovic, J. G. Proakis, and P. Hursky, "Mitigation of intercarrier interference for ofdm over time-varying underwater acoustic channels," *IEEE Journal of Oceanic Engineering*, vol. 36, no. 2, pp. 156–171, 2011.

[12] Y. Polyanskiy, "A perspective on massive random-access," in *IEEE Int. Symp. on Inform. Theory*, Aachen, Germany, June 2017, pp. 2523–2527.

[13] O. Ordentlich and Y. Polyanskiy, "Low complexity schemes for the random access Gaussian channel," in *IEEE Int. Symposium on Information Theory*, June 2017, pp. 2528–2532.

[14] V. K. Amalladinne, J.-F. Chamberland, and K. R. Narayanan, "A coded compressed sensing scheme for unsourced multiple access," *IEEE Transactions on Information Theory*, vol. 66, no. 10, pp. 6509–6533, 2020.

[15] A. Fengler, P. Jung, and G. Caire, "SPARCs and AMP for unsourced random access," in *IEEE Int. Symp. on Information Theory, Paris, France*, July 2019, pp. 2843–2847.

[16] R. Calderbank and A. Thompson, "CHIRRUP: a practical algorithm for unsourced multiple access," *Information and Inference: A Journal of the IMA*, 12 2019.

[17] V. K. Amalladinne, A. K. Pradhan, C. Rush, J.-F. Chamberland, and K. R. Narayanan, "On approximate message passing for unsourced access with coded compressed sensing," *IEEE Int. Symp. on Inf. Theory*, Jun 2020.

[18] G. Liva, "Graph-based analysis and optimization of contention resolution diversity slotted ALOHA," *IEEE Trans. on Communications*, vol. 67, no. 12, pp. 477–487, February 2011.

[19] A. Glebov, N. Matveev, K. Andreev, A. Frolov, and A. Turlikov, "Achievability bounds for t-fold irregular repetition slotted ALOHA scheme in the Gaussian MAC," in *2019 IEEE Wireless Communications and Networking Conference (WCNC)*, 2019.

[20] S. S. Kowshik, K. Andreev, A. Frolov, and Y. Polyanskiy, "Energy efficient coded random access for the wireless uplink," *IEEE Transactions on Communications*, vol. 68, no. 8, pp. 4694–4708, 2020.

[21] K. Andreev, E. Marshakov, and A. Frolov, "A polar code based TIN-SIC scheme for the unsourced random access in the quasi-static fading MAC," in *IEEE Int. Symp. on Inf. Theory*, Jun. 2020, pp. 1–5.

[22] A. Vem, K. Narayanan, J.-F. Chamberland, and J. Cheng, "A user-independent successive interference cancellation based coding scheme for the unsourced random access Gaussian channel," *IEEE Trans. on Commun.*, vol. 67, no. 12, pp. 8258–8272, December 2019.

[23] A. Pradhan, V. Amalladinne, A. Vem, K. R. Narayanan, and J.-F. Chamberland, "A joint graph based coding scheme for the unsourced random access Gaussian channel," *GLOBECOM*, Dec. 2019.

[24] E. Marshakov, G. Balitskiy, K. Andreev, and A. Frolov, "A polar code based unsourced random access for the gaussian MAC," in *IEEE Vehicular Technology Conference*, Sep. 2019, pp. 1–5.

[25] B. D. Van Veen and K. M. Buckley, "Beamforming: A versatile approach to spatial filtering," *IEEE assp magazine*, vol. 5, no. 2, pp. 4–24, 1988.

[26] J. C. Peterson and M. B. Porter, "Ray/beam tracing for modeling the effects of ocean and platform dynamics," *IEEE Journal of Oceanic Engineering*, vol. 38, no. 4, pp. 655–665, 2013.

[27] G. H. Brooke, D. J. Thomson, and G. R. Ebbeson, "Pecan: A canadian parabolic equation model for underwater sound propagation," *Journal of Computational Acoustics*, vol. 9, no. 01, pp. 69–100, 2001.

[28] P. Qarabaqi and M. Stojanovic, "Statistical characterization and computationally efficient modeling of a class of underwater acoustic communication channels," *IEEE Journal of Oceanic Engineering*, vol. 38, no. 4, pp. 701–717, 2013.

[29] P.-J. Bouvet and A. Loussert, "Capacity analysis of underwater acoustic mimo communications," in *OCEANS'10 IEEE SYDNEY*. IEEE, 2010, pp. 1–8.

[30] A. Radosevic, D. Fertonani, T. M. Duman, J. G. Proakis, and M. Stojanovic, "Capacity of mimo systems in shallow water acoustic channels," in *2010 Conference Record of the Forty Fourth Asilomar Conference on Signals, Systems and Computers*. IEEE, 2010, pp. 2164–2168.

[31] M. Bashir, D. Truhachev, and C. Schlegel, "Kalman forward-backward channel tracking and combining for ofdm in underwater acoustic channels," in *2018 OCEANS-MTS/IEEE Kobe Techno-Oceans (OTO)*. IEEE, 2018, pp. 1–10.

[32] "Random access signaling in underwater acoustic channels: Challenges and approaches," *ADHOCNETS 2017,Niagara Falls, Canada, September 2017*.

[33] P. Van Walree, T. Jenserud, and R. Otnes, "Stretched-exponential doppler spectra in underwater acoustic communication channels," *The Journal of the Acoustical Society of America*, vol. 128, no. 5, pp. EL329–EL334, 2010.

[34] P. Hoeher, "A statistical discrete-time model for the wssus multipath channel," *IEEE Transactions on vehicular technology*, vol. 41, no. 4, pp. 461–468, 1992.

[35] P. A. Van Walree, T. Jenserud, and M. Smedsrud, "A discrete-time channel simulator driven by measured scattering functions," *IEEE journal on selected areas in communications*, vol. 26, no. 9, pp. 1628–1637, 2008.

[36] F.-X. Socheleau, C. Laot, and J.-M. Passerieux, "Stochastic replay of non-wssus underwater acoustic communication channels recorded at sea," *IEEE Transactions on Signal Processing*, vol. 59, no. 10, pp. 4838–4849, 2011.

[37] D. Tse and P. Viswanath, *Fundamentals of wireless communication*. Cambridge university press, 2005.

[38] C. Schlegel and M. Jar, "Embedded pilot and multi-size ofdm processing for jointly time and frequency selective channels," in *2016 International Symposium on Information Theory and Its Applications (ISITA)*. IEEE, 2016, pp. 748–752.

[39] A. G. Zajic, "Statistical Modeling of MIMO Mobile-to-Mobile Underwater Channels," *IEEE Transactions on Vehicular Technology*, vol. 60, no. 4, pp. 1337–1351, 2011.

[40] P. A. Van Walree, T. Jenserud, and M. Smedsrud, "A Discrete-Time Channel Simulator Driven by Measured Scattering Functions," *IEEE journal on selected areas in communications*, vol. 26, no. 9, pp. 1628–1637, 2008.

[41] P. Van Walree, T. Jenserud, and R. Otnes, "Stretched-exponential doppler spectra in underwater acoustic communication channels," *The Journal of the Acoustical Society of America*, vol. 128, no. 5, pp. EL329–EL334, 2010.

[42] F.-X. Socheleau, C. Laot, and J.-M. Passerieux, "Stochastic Replay of Non-WSSUS Underwater Acoustic Communication Channels Recorded at Sea," *IEEE Transactions on Signal Processing*, vol. 59, no. 10, pp. 4838–4849, 2011.

[43] M. Siderius and M. B. Porter, "Modeling Broadband Ocean Acoustic Transmissions with Time-Varying Sea Surfaces," *The Journal of the Acoustical Society of America*, vol. 124, no. 1, pp. 137–150, 2008.

[44] G. H. Brooke, D. J. Thomson, and G. R. Ebbeson, "PECan: A Canadian Parabolic Equation Model For Underwater Sound Propagation," *Journal of Computational Acoustics*, vol. 9, no. 01, pp. 69–100, 2001.

[45] J. Kim, I.-S. Koh, and Y. Lee, "Spatially Correlated Underwater Acoustic Multiple-Input and Multiple-Output Channel Model and its Application to Estimation of Channel Capacity," *Japanese Journal of Applied Physics*, vol. 54, no. 7S1, p. 07HG01, 2015.

[46] F. B. Jensen, W. A. Kuperman, M. B. Porter, and H. Schmidt, *Computational Ocean Acoustics*. Springer Science & Business Media, 2011.

[47] T. J. Hayward and T. Yang, "Single-and Multi-channel Underwater Acoustic Communication Channel Capacity: A Computational Study," *The Journal of the Acoustical Society of America*, vol. 119, no. 5, pp. 3428–3428, 2006.

[48] P. H. Dahl, "On the spatial coherence and angular spreading of sound forward scattered from the sea surface: Measurements and interpretive model," *The Journal of the Acoustical Society of America*, vol. 100, no. 2, pp. 748–758, 1996.

[49] D. Tse and P. Viswanath, *Fundamentals of Wireless Communication*. Cambridge university press, 2005.

[50] T. K. Stanton, "Broadband Acoustic Sensing of the Ocean," vol. 36, no. 2, pp. 95–107, 2009.

[51] L. D. Landau and E. M. Lifshitz, *Fluid Mechanics*. Butterworth, 1987.

[52] D. Carter, "Prediction of Wave Height and Period for a Constant Wind Velocity using the JONSWAP Results," *Ocean Engineering*, vol. 9, no. 1, pp. 17–33, 1982.

[53] L. Mandel and E. Wolf, *Optical Coherence and Quantum Optics*. Cambridge university press, 1995.

[54] W. M. Organization, "Manual on Codes: International Codes Volume I. 1 Annex II to the WMO Technical Regulations Part A—Alphanumeric Codes," 2016.

[55] E. Biglieri and G. Taricco, *Transmission and reception with multiple antennas: Theoretical foundations*. Now Publishers Inc, 2004.

[56] M. Salehi and J. Proakis, "Digital Communications," *McGraw-Hill Education*, vol. 31, p. 32, 2007.

[57] K. Hasselmann, T. Barnett, E. Bouws, H. Carlson, D. Cartwright, K. Enke, J. Ewing, H. Gienapp, D. Hasselmann, P. Kruseman, *et al.*, "Measurements of Wind-Wave Growth and Swell Decay During the Joint North Sea Wave Project (JONSWAP)," *Ergänzungsheft 8-12*, 1973.

[58] R. Headrick and L. Freitag, "Growth of underwater communication technology in the us navy," *IEEE Communications Magazine*, vol. 47, no. 1, pp. 80–82, 2009.

[59] H. Haas, L. Yin, Y. Wang, and C. Chen, "What is lifi?" *Journal of lightwave technology*, vol. 34, no. 6, pp. 1533–1544, 2015.

[60] E. M. Sozer, M. Stojanovic, and J. G. Proakis, "Underwater acoustic networks," *IEEE journal of oceanic engineering*, vol. 25, no. 1, pp. 72–83, 2000.

[61] M. Stojanovic and L. Freitag, "Multichannel detection for wideband underwater acoustic cdma communications," *IEEE Journal of Oceanic Engineering*, vol. 31, no. 3, pp. 685–695, 2006.

[62] C. C. Tsimenidis, O. R. Hinton, A. E. Adams, and B. S. Sharif, "Underwater acoustic receiver employing direct-sequence spread spectrum and spatial diversity combining for shallow-water multiaccess networking," *IEEE Journal of Oceanic Engineering*, vol. 26, no. 4, pp. 594–603, 2001.

[63] L. Freitag, M. Stojanovic, S. Singh, and M. Johnson, "Analysis of channel effects on direct-sequence and frequency-hopped spread-spectrum acoustic communication," *IEEE journal of oceanic engineering*, vol. 26, no. 4, pp. 586–593, 2001.

[64] M. Stojanovic, *Low complexity OFDM detector for underwater acoustic channels*. IEEE, 2006.

[65] X. Cai and G. B. Giannakis, "Bounding performance and suppressing intercarrier interference in wireless mobile ofdm," *IEEE Transactions on communications*, vol. 51, no. 12, pp. 2047–2056, 2003.

[66] C. Shin, J. G. Andrews, and E. J. Powers, "An efficient design of doubly selective channel estimation for ofdm systems," *IEEE Transactions on Wireless Communications*, vol. 6, no. 10, pp. 3790–3802, 2007.

[67] Y. M. Aval and M. Stojanovic, "Partial fft demodulation for coherent detection of ofdm signals over underwater acoustic channels," in *2013 MTS/IEEE OCEANS-Bergen*. IEEE, 2013, pp. 1–4.

[68] Y. M. Aval and M. Stojanovic, "Fractional fft demodulation for differentially coherent detection of acoustic ofdm signals," in *2012 Conference Record of the Forty Sixth Asilomar Conference on Signals, Systems and Computers (ASILOMAR)*. IEEE, 2012, pp. 1525–1529.

[69] J. Wu and Y. R. Zheng, "Oversampled orthogonal frequency division multiplexing in doubly selective fading channels," *IEEE Transactions on Communications*, vol. 59, no. 3, pp. 815–822, 2010.

[70] B. Peng, P. S. Rossi, H. Dong, and K. Kansanen, "Time-domain oversampled ofdm communication in doubly-selective underwater acoustic channels," *IEEE Communications Letters*, vol. 19, no. 6, pp. 1081–1084, 2015.

[71] S.-J. Hwang and P. Schniter, "Efficient multicarrier communication for highly spread underwater acoustic channels," *IEEE Journal on Selected Areas in Communications*, vol. 26, no. 9, pp. 1674–1683, 2008.

[72] S. Mason, C. Berger, S. Zhou, K. Ball, L. Freitag, and P. Willett, "An ofdm design for underwater acoustic channels with doppler spread," in *2009 IEEE 13th Digital Signal Processing Workshop and 5th IEEE Signal Processing Education Workshop*. IEEE, 2009, pp. 138–143.

[73] S. F. Mason, C. R. Berger, S. Zhou, K. R. Ball, L. Freitag, and P. Willett, *Receiver comparisons on an OFDM design for Doppler spread channels*. IEEE, 2009.

[74] J. Huang, J. Huang, C. R. Berger, S. Zhou, and P. Willett, "Iterative sparse channel estimation and decoding for underwater mimo-ofdm," *EURASIP Journal on Advances in Signal Processing*, vol. 2010, p. 1, 2010.

[75] T. Kang and R. A. Iltis, "Iterative carrier frequency offset and channel estimation for underwater acoustic ofdm systems," *IEEE Journal on Selected Areas in Communications*, vol. 26, no. 9, pp. 1650–1661, 2008.

[76] K. Fang, L. Rugini, and G. Leus, "Iterative channel estimation and turbo equalization for time-varying ofdm systems," in *2008 IEEE International Conference on Acoustics, Speech and Signal Processing*. IEEE, 2008, pp. 2909–2912.

[77] E. Calvo and M. Stojanovic, "Efficient channel-estimation-based multiuser detection for underwater cdma systems," *IEEE Journal of Oceanic Engineering*, vol. 33, no. 4, pp. 502–512, 2008.

[78] J. Huang, S. Zhou, J. Huang, C. R. Berger, and P. Willett, "Progressive inter-carrier interference equalization for ofdm transmission over time-varying underwater acoustic channels," *IEEE Journal of Selected Topics in Signal Processing*, vol. 5, no. 8, pp. 1524–1536, 2011.

[79] H. Nguyen-Le, T. Le-Ngoc, and N. H. Tran, "Iterative receiver design with joint doubly selective channel and cfo estimation for coded mimo-ofdm transmissions," *IEEE Transactions on Vehicular Technology*, vol. 60, no. 8, pp. 4052–4057, 2011.

[80] L. Cannelli, G. Leus, H. Dol, and P. van Walree, *Adaptive turbo equalization for underwater acoustic communication.* IEEE, 2013.

[81] Z. Yang and Y. R. Zheng, "Iterative channel estimation and turbo equalization for multiple-input multiple-output underwater acoustic communications," *IEEE Journal of Oceanic Engineering*, vol. 41, no. 1, pp. 232–242, 2015.

[82] Z. Chen, J. Wang, and Y. R. Zheng, "Frequency-domain turbo equalization with iterative channel estimation for mimo underwater acoustic communications," *IEEE Journal of Oceanic Engineering*, vol. 42, no. 3, pp. 711–721, 2016.

[83] D. Truhachev and C. Schlegel, "Coupling data transmission for multiple-access communications," *IEEE Transactions on Information Theory*, 2019.

[84] J. G. Proakis and M. Salehi, *Digital communications.* McGraw-hill New York, 2001, vol. 4.

[85] R. H. Clarke, "A statistical theory of mobile-radio reception," *The Bell System Technical Journal*, vol. 47, no. 6, pp. 957–1000, July 1968.

[86] M. Stojanovic, "Adaptive channel estimation for underwater acoustic mimo ofdm systems," in *Digital Signal Processing Workshop and 5th IEEE SPEW, 2009. DSP/SPE 2009. IEEE 13th.* IEEE, 2009, pp. 132–137.

[87] N. Lin, H. Sun, E. Cheng, J. Qi, X. Kuai, and J. Yan, "Prediction based sparse channel estimation for underwater acoustic ofdm," *Applied Acoustics*, vol. 96, pp. 94–100, 2015.

[88] A. H. Sayed, *Adaptive filters.* John Wiley & Sons, 2011.

[89] C. R. Berger, S. Zhou, J. C. Preisig, and P. Willett, "Sparse channel estimation for multicarrier underwater acoustic communication: From subspace methods to compressed sensing," *IEEE Transactions on Signal Processing*, vol. 58, no. 3, pp. 1708–1721, March 2010.

[90] U. Gunturkun, C. Schlegel, and D. Truhachev, "Compression-aided kalman filter for recursive bayesian estimation of sparse wideband channels in ofdm systems," in *OCEANS 2016 MTS/IEEE Monterey*, Sept 2016, pp. 1–8.

[91] T. Kang and R. A. Iltis, "Matching pursuits channel estimation for an underwater acoustic ofdm modem," in *2008 IEEE International Conference on Acoustics, Speech and Signal Processing*. IEEE, 2008, pp. 5296–5299.

[92] C. R. Berger, S. Zhou, J. C. Preisig, and P. Willett, "Sparse channel estimation for multicarrier underwater acoustic communication: From subspace methods to compressed sensing," in *OCEANS 2009-EUROPE*. IEEE, 2009, pp. 1–8.

[93] W. Li and J. C. Preisig, "Estimation of rapidly time-varying sparse channels," *IEEE Journal of Oceanic Engineering*, vol. 32, no. 4, pp. 927–939, 2007.

[94] A. Tadayon and M. Stojanovic, "Iterative sparse channel estimation and spatial correlation learning for multichannel acoustic ofdm systems," *IEEE Journal of Oceanic Engineering*, vol. 44, no. 4, pp. 820–836, 2019.

[95] M. Stojanovic and S. Tadayon, "Estimation and tracking of time-varying channels in ofdm systems," in *2014 52nd Annual Allerton Conference on Communication, Control, and Computing (Allerton)*. IEEE, 2014, pp. 116–122.

[96] J. Huang, C. R. Berger, S. Zhou, and J. Huang, "Comparison of basis pursuit algorithms for sparse channel estimation in underwater acoustic ofdm," in *OCEANS'10 IEEE SYDNEY*. IEEE, 2010, pp. 1–6.

[97] S. Beygi and U. Mitra, "Multi-scale multi-lag channel estimation using low rank approximation for ofdm," *IEEE transactions on signal processing*, vol. 63, no. 18, pp. 4744–4755, 2015.

[98] J. K. Tugnait, S. He, and H. Kim, "Doubly selective channel estimation using exponential basis models and subblock tracking," *IEEE Transactions on Signal Processing*, vol. 58, no. 3, pp. 1275–1289, 2009.

[99] K. Muralidhar and K. H. Li, "A low-complexity kalman approach for channel estimation in doubly-selective ofdm systems," *IEEE Signal Processing Letters*, vol. 16, no. 7, pp. 632–635, 2009.

[100] F. Qu and L. Yang, "Basis expansion model for underwater acoustic channels?" in *OCEANS 2008*. IEEE, 2008, pp. 1–7.

[101] M. Bashir, D. Truhachev, and C. Schlegel, "Kalman forward-backward channel tracking and combining for ofdm in underwater acoustic channels," in *2018 OCEANS-MTS/IEEE Kobe Techno-Oceans (OTO)*. IEEE, 2018, pp. 1–10.

[102] T. Kailath, A. H. Sayed, and B. Hassibi, *Linear estimation*. Prentice Hall Upper Saddle River, NJ, 2000, vol. 1.

[103] S. Song, A. C. Singer, and K.-M. Sung, "Soft input channel estimation for turbo equalization," *IEEE Transactions on Signal Processing*, vol. 52, no. 10, pp. 2885–2894, Oct 2004.

[104] C. Schlegel and D. Truhachev, "Random access signaling in underwater acoustic channels: Challenges and approaches," *ADHOCNETS 2017, 9th IAE International Conference on Ad Hoc Networks 2017, Niagara Falls, Canada, September 2017*.

[105] N. Abramson, "The ALOHA system - another alternative for computer communications," in *Proc. 1970 Fall Joint Computer Conference. AFIPS Press.*, 1970.

[106] A. K. Pradhan, V. K. Amalladinne, K. R. Narayanan, and J.-F. Chamberland, "Polar coding and random spreading for unsourced multiple access." [Online]. Available: http://arxiv.org/abs/1911.01009

[107] A. Fengler, S. Haghighatshoar, P. Jung, and G. Caire, "Non-bayesian activity detection, large-scale fading coefficient estimation, and unsourced random access with a massive mimo receiver," *IEEE Transactions on Information Theory*, vol. 67, no. 5, pp. 2925–2951, 2021.

[108] A. Decurninge, I. Land, and M. Guillaud, "Tensor-based modulation for unsourced massive random access," *IEEE Wireless Communications Letters*, vol. 10, no. 3, pp. 552–556, 2020.

[109] A. Fengler, P. Jung, and G. Caire, "Pilot-based unsourced random access with a massive MIMO receiver, MRC and polar codes," *arXiv preprint arXiv:2012.03277*, 2020.

[110] V. Shyianov, F. Bellili, A. Mezghani, and E. Hossain, "Massive unsourced random access based on uncoupled compressive sensing: Another blessing of massive mimo," *IEEE J. on Selected Areas in Commun.*, vol. 39, no. 3, pp. 820–834, 2021.

[111] D. Truhachev, M. Bashir, A. Karami, and E. Nassaji, "Low-complexity coding and spreading for unsourced random access," *IEEE Communication Letters*, vol. 25, no. 3, pp. 774–778, March 2021.

[112] A. Maleki, L. Anitori, Z. Yang, and R. G. Baraniuk, "Asymptotic analysis of complex LASSO via complex approximate message passing CAMP," *IEEE Transactions on Information Theory*, vol. 59, no. 7, pp. 4290–4308, 2013.

[113] A. Hocquenghem, "Codes correcteurs d'erreurs," *Chiffres (in French)*, vol. 2, pp. 147–156, 1959.

[114] R. C. Bose and D. K. Ray-Chaudhuri, "On a class of error correcting binary group codes," *Inform. and Control*, vol. 3, pp. 68–79, Mar. 1960.

[115] A. Greig and R. Venkataramanan, "Techniques for improving the finite length performance of sparse superposition codes," *IEEE Transactions on Communications*, vol. 66, no. 3, pp. 905–917, 2017.

[116] A. Fengler, P. Jung, and G. Caire, "SPARCs and AMP for unsourced random access," in *2019 IEEE International Symposium on Information Theory (ISIT)*. IEEE, 2019, pp. 2843–2847.

[117] J. A. Tropp and A. C. Gilbert, "Signal recovery from random measurements via orthogonal matching pursuit," *IEEE Transactions on Information theory*, vol. 53, no. 12, pp. 4655–4666, 2007.

[118] R. Tibshirani, "Regression shrinkage and selection via the lasso," *Journal of the Royal Statistical Society: Series B (Methodological)*, vol. 58, no. 1, pp. 267–288, 1996.

[119] C. L. Lawson and R. J. Hanson, *Solving least squares problems*. vol. 15. Philadelphia, PA, USA: SIAM, 1995.

[120] D. L. Donoho, A. Maleki, and A. Montanari, "Message-passing algorithms for compressed sensing," *Proceedings of the National Academy of Sciences*, vol. 106, no. 45, pp. 18 914–18 919, 2009.

[121] D. L. Donoho, A. Javanmard, and A. Montanari, "Information theoretically optimal compressed sensing via spatial coupling and approximate message passing," *IEEE Transactions on Information theory*, vol. 59, no. 11, pp. 7434–7464, 2013.

[122] A. Mousavi, A. Maleki, and R. G. Baraniuk, "Parameterless optimal approximate message passing," *arXiv preprint arXiv:1311.0035*, 2013.

[123] C. Rush, A. Greig, and R. Venkataramanan, "Capacity-achieving sparse superposition codes via approximate message passing decoding," *IEEE Transactions on Information Theory*, vol. 63, no. 3, pp. 1476–1500, 2017.

[124] K. Niu and K. Chen, "CRC-aided decoding of polar codes," *IEEE Comm. Letters*, vol. 16, no. 10, pp. 1668–1671, 2012.

[125] M. Burnashev, C. Schlegel, W. Krzymien, and Z. Shi, "Characteristics analysis of successive interference cancellation methods," *Problems of Information Transmission*, vol. 40, no. 4, pp. 297–317, December 2004.

[126] "Implementation agreement 400ZR," *OFI Internetworking Forum*, March 2020.

[127] D. Truhachev, K. El-Sankary, A. Karami, A. Zokaei, and S. Li, "Efficient implementation of 400 Gbps optical communication FEC," *IEEE Transactions on Circuits and Systems I: Regular Papers*, vol. 68, no. 1, pp. 496–509, 2020.

Appendix A

IEEE Copyright and Consent Forms

IEEE COPYRIGHT AND CONSENT FORM

To ensure uniformity of treatment among all contributors, other forms may not be substituted for this form, nor may any wording of the form be changed. This form is intended for original material submitted to the IEEE and must accompany any such material in order to be published by the IEEE. Please read the form carefully and keep a copy for your files.

Kalman Forward-Backward Channel Tracking and Combining for OFDM in Underwater Acoustic Channels
Murwan Bashir, Dmitri Truhachev, Christian Schlegel
2018 OCEANS - MTS/IEEE Kobe Techno-Ocean (OTO)

COPYRIGHT TRANSFER

The undersigned hereby assigns to The Institute of Electrical and Electronics Engineers, Incorporated (the "IEEE") all rights under copyright that may exist in and to: (a) the Work, including any revised or expanded derivative works submitted to the IEEE by the undersigned based on the Work; and (b) any associated written or multimedia components or other enhancements accompanying the Work.

GENERAL TERMS

1. The undersigned represents that he/she has the power and authority to make and execute this form.
2. The undersigned agrees to indemnify and hold harmless the IEEE from any damage or expense that may arise in the event of a breach of any of the warranties set forth above.
3. The undersigned agrees that publication with IEEE is subject to the policies and procedures of the IEEE PSPB Operations Manual.
4. In the event the above work is not accepted and published by the IEEE or is withdrawn by the author(s) before acceptance by the IEEE, the foregoing copyright transfer shall be null and void. In this case, IEEE will retain a copy of the manuscript for internal administrative/record-keeping purposes.
5. For jointly authored Works, all joint authors should sign, or one of the authors should sign as authorized agent for the others.
6. The author hereby warrants that the Work and Presentation (collectively, the "Materials") are original and that he/she is the author of the Materials. To the extent the Materials incorporate text passages, figures, data or other material from the works of others, the author has obtained any necessary permissions. Where necessary, the author has obtained all third party permissions and consents to grant the license above and has provided copies of such permissions and consents to IEEE

You have indicated that you DO wish to have video/audio recordings made of your conference presentation under terms and conditions set forth in "Consent and Release."

CONSENT AND RELEASE

1. In the event the author makes a presentation based upon the Work at a conference hosted or sponsored in whole or in part by the IEEE, the author, in consideration for his/her participation in the conference, hereby grants the IEEE the unlimited, worldwide, irrevocable permission to use, distribute, publish, license, exhibit, record, digitize, broadcast, reproduce and archive, in any format or medium, whether now known or hereafter developed: (a) his/her presentation and comments at the conference; (b) any written materials or multimedia files used in connection with his/her presentation; and (c) any recorded interviews of him/her (collectively, the "Presentation"). The permission granted includes the transcription and reproduction of the Presentation for inclusion in products sold or distributed by IEEE and live or recorded broadcast of the Presentation during or after the conference.
2. In connection with the permission granted in Section 1, the author hereby grants IEEE the unlimited, worldwide, irrevocable right to use his/her name, picture, likeness, voice and biographical information as part of the advertisement, distribution and sale of products incorporating the Work or Presentation, and releases IEEE from any claim based on right of privacy or publicity.

BY TYPING IN YOUR FULL NAME BELOW AND CLICKING THE SUBMIT BUTTON, YOU CERTIFY THAT SUCH ACTION CONSTITUTES YOUR ELECTRONIC SIGNATURE TO THIS FORM IN ACCORDANCE WITH UNITED STATES LAW, WHICH AUTHORIZES ELECTRONIC SIGNATURE BY AUTHENTICATED REQUEST FROM A USER OVER THE INTERNET AS A VALID SUBSTITUTE FOR A WRITTEN SIGNATURE.

MURWAN BASHIR	23-03-2018
Signature	**Date (dd-mm-yyyy)**

Information for Authors

AUTHOR RESPONSIBILITIES

The IEEE distributes its technical publications throughout the world and wants to ensure that the material submitted to its publications is properly available to the readership of those publications. Authors must ensure that their Work meets the requirements as stated in section 8.2.1 of the IEEE PSPB Operations Manual, including provisions covering originality, authorship, author responsibilities and author misconduct. More information on IEEE's publishing policies may be found at http://www.ieee.org/publications_standards/publications/rights/authorrightsresponsibilities.html Authors are advised especially of IEEE PSPB Operations Manual section 8.2.1.B12: "It is the responsibility of the authors, not the IEEE, to determine whether disclosure of their material requires the prior consent of other parties and, if so, to obtain it." Authors are also advised of IEEE PSPB Operations Manual section 8.1.1B: "Statements and opinions given in work published by the IEEE are the expression of the authors."

RETAINED RIGHTS/TERMS AND CONDITIONS

- Authors/employers retain all proprietary rights in any process, procedure, or article of manufacture described in the Work.
- Authors/employers may reproduce or authorize others to reproduce the Work, material extracted verbatim from the Work, or derivative works for the author's personal use or for company use, provided that the source and the IEEE copyright notice are indicated, the copies are not used in any way that implies IEEE endorsement of a product or service of any employer, and the copies themselves are not offered for sale.
- Although authors are permitted to re-use all or portions of the Work in other works, this does not include granting third-party requests for reprinting, republishing, or other types of re-use.The IEEE Intellectual Property Rights office must handle all such third-party requests.
- Authors whose work was performed under a grant from a government funding agency are free to fulfill any deposit mandates from that funding agency.

AUTHOR ONLINE USE

- **Personal Servers**. Authors and/or their employers shall have the right to post the accepted version of IEEE-copyrighted articles on their own personal servers or the servers of their institutions or employers without permission from IEEE, provided that the posted version includes a prominently displayed IEEE copyright notice and, when published, a full citation to the original IEEE publication, including a link to the article abstract in IEEE Xplore. Authors shall not post the final, published versions of their papers.
- **Classroom or Internal Training Use.** An author is expressly permitted to post any portion of the accepted version of his/her own IEEE-copyrighted articles on the author's personal web site or the servers of the author's institution or company in connection with the author's teaching, training, or work responsibilities, provided that the appropriate copyright, credit, and reuse notices appear prominently with the posted material. Examples of permitted uses are lecture materials, course packs, e-reserves, conference presentations, or in-house training courses.
- **Electronic Preprints.** Before submitting an article to an IEEE publication, authors frequently post their manuscripts to their own web site, their employer's site, or to another server that invites constructive comment from colleagues. Upon submission of an article to IEEE, an author is required to transfer copyright in the article to IEEE, and the author must update any previously posted version of the article with a prominently displayed IEEE copyright notice. Upon publication of an article by the IEEE, the author must replace any previously posted electronic versions of the article with either (1) the full citation to the

IEEE work with a Digital Object Identifier (DOI) or link to the article abstract in IEEE Xplore, or (2) the accepted version only (not the IEEE-published version), including the IEEE copyright notice and full citation, with a link to the final, published article in IEEE Xplore.

Questions about the submission of the form or manuscript must be sent to the publication's editor.
Please direct all questions about IEEE copyright policy to:
IEEE Intellectual Property Rights Office, copyrights@ieee.org, +1-732-562-3966

IEEE COPYRIGHT AND CONSENT FORM

To ensure uniformity of treatment among all contributors, other forms may not be substituted for this form, nor may any wording of the form be changed. This form is intended for original material submitted to the IEEE and must accompany any such material in order to be published by the IEEE. Please read the form carefully and keep a copy for your files.

Modeling of Underwater Acoustic Channels for Communication System Testing
Dmitri Truhachev, Christian Schlegel, Murwan Bashir, Jean-Francois Bousquet
OCEANS 2018 MTS/IEEE Charleston

COPYRIGHT TRANSFER

The undersigned hereby assigns to The Institute of Electrical and Electronics Engineers, Incorporated (the "IEEE") all rights under copyright that may exist in and to: (a) the Work, including any revised or expanded derivative works submitted to the IEEE by the undersigned based on the Work; and (b) any associated written or multimedia components or other enhancements accompanying the Work.

GENERAL TERMS

1. The undersigned represents that he/she has the power and authority to make and execute this form.
2. The undersigned agrees to indemnify and hold harmless the IEEE from any damage or expense that may arise in the event of a breach of any of the warranties set forth above.
3. The undersigned agrees that publication with IEEE is subject to the policies and procedures of the IEEE PSPB Operations Manual.
4. In the event the above work is not accepted and published by the IEEE or is withdrawn by the author(s) before acceptance by the IEEE, the foregoing copyright transfer shall be null and void. In this case, IEEE will retain a copy of the manuscript for internal administrative/record-keeping purposes.
5. For jointly authored Works, all joint authors should sign, or one of the authors should sign as authorized agent for the others.
6. The author hereby warrants that the Work and Presentation (collectively, the "Materials") are original and that he/she is the author of the Materials. To the extent the Materials incorporate text passages, figures, data or other material from the works of others, the author has obtained any necessary permissions. Where necessary, the author has obtained all third party permissions and consents to grant the license above and has provided copies of such permissions and consents to IEEE

You have indicated that you DO wish to have video/audio recordings made of your conference presentation under terms and conditions set forth in "Consent and Release."

CONSENT AND RELEASE

1. In the event the author makes a presentation based upon the Work at a conference hosted or sponsored in whole or in part by the IEEE, the author, in consideration for his/her participation in the conference, hereby grants the IEEE the unlimited, worldwide, irrevocable permission to use, distribute, publish, license, exhibit, record, digitize, broadcast, reproduce and archive, in any format or medium, whether now known or hereafter developed: (a) his/her presentation and comments at the conference; (b) any written materials or multimedia files used in connection with his/her presentation; and (c) any recorded interviews of him/her (collectively, the "Presentation"). The permission granted includes the transcription and reproduction of the Presentation for inclusion in products sold or distributed by IEEE and live or recorded broadcast of the Presentation during or after the conference.
2. In connection with the permission granted in Section 1, the author hereby grants IEEE the unlimited, worldwide, irrevocable right to use his/her name, picture, likeness, voice and biographical information as part of the advertisement, distribution and sale of products incorporating the Work or Presentation, and releases IEEE from any claim based on right of privacy or publicity.

BY TYPING IN YOUR FULL NAME BELOW AND CLICKING THE SUBMIT BUTTON, YOU CERTIFY THAT SUCH ACTION CONSTITUTES YOUR ELECTRONIC SIGNATURE TO THIS FORM IN ACCORDANCE WITH UNITED STATES LAW, WHICH AUTHORIZES ELECTRONIC SIGNATURE BY AUTHENTICATED REQUEST FROM A USER OVER THE INTERNET AS A VALID SUBSTITUTE FOR A WRITTEN SIGNATURE.

Dmitry Trukhachev	15-08-2018
Signature	**Date (dd-mm-yyyy)**

Information for Authors

AUTHOR RESPONSIBILITIES

The IEEE distributes its technical publications throughout the world and wants to ensure that the material submitted to its publications is properly available to the readership of those publications. Authors must ensure that their Work meets the requirements as stated in section 8.2.1 of the IEEE PSPB Operations Manual, including provisions covering originality, authorship, author responsibilities and author misconduct. More information on IEEE's publishing policies may be found at http://www.ieee.org/publications_standards/publications/rights/authorrightsresponsibilities.html Authors are advised especially of IEEE PSPB Operations Manual section 8.2.1.B12: "It is the responsibility of the authors, not the IEEE, to determine whether disclosure of their material requires the prior consent of other parties and, if so, to obtain it." Authors are also advised of IEEE PSPB Operations Manual section 8.1.1B: "Statements and opinions given in work published by the IEEE are the expression of the authors."

RETAINED RIGHTS/TERMS AND CONDITIONS

- Authors/employers retain all proprietary rights in any process, procedure, or article of manufacture described in the Work.
- Authors/employers may reproduce or authorize others to reproduce the Work, material extracted verbatim from the Work, or derivative works for the author's personal use or for company use, provided that the source and the IEEE copyright notice are indicated, the copies are not used in any way that implies IEEE endorsement of a product or service of any employer, and the copies themselves are not offered for sale.
- Although authors are permitted to re-use all or portions of the Work in other works, this does not include granting third-party requests for reprinting, republishing, or other types of re-use.The IEEE Intellectual Property Rights office must handle all such third-party requests.
- Authors whose work was performed under a grant from a government funding agency are free to fulfill any deposit mandates from that funding agency.

AUTHOR ONLINE USE

- **Personal Servers**. Authors and/or their employers shall have the right to post the accepted version of IEEE-copyrighted articles on their own personal servers or the servers of their institutions or employers without permission from IEEE, provided that the posted version includes a prominently displayed IEEE copyright notice and, when published, a full citation to the original IEEE publication, including a link to the article abstract in IEEE Xplore. Authors shall not post the final, published versions of their papers.
- **Classroom or Internal Training Use.** An author is expressly permitted to post any portion of the accepted version of his/her own IEEE-copyrighted articles on the author's personal web site or the servers of the author's institution or company in connection with the author's teaching, training, or work responsibilities, provided that the appropriate copyright, credit, and reuse notices appear prominently with the posted material. Examples of permitted uses are lecture materials, course packs, e-reserves, conference presentations, or in-house training courses.
- **Electronic Preprints.** Before submitting an article to an IEEE publication, authors frequently post their manuscripts to their own web site, their employer's site, or to another server that invites constructive comment from colleagues. Upon submission of an article to IEEE, an author is required to transfer copyright in the article to IEEE, and the author must update any previously posted version of the article with a prominently displayed IEEE copyright notice. Upon publication of an article by the IEEE, the author must replace any previously posted electronic versions of the article with either (1) the full citation to the

IEEE work with a Digital Object Identifier (DOI) or link to the article abstract in IEEE Xplore, or (2) the accepted version only (not the IEEE-published version), including the IEEE copyright notice and full citation, with a link to the final, published article in IEEE Xplore.

Questions about the submission of the form or manuscript must be sent to the publication's editor.
Please direct all questions about IEEE copyright policy to:
IEEE Intellectual Property Rights Office, copyrights@ieee.org, +1-732-562-3966